NTNU – Trondheim
Norwegian University of
Science and Technology

Self-Assembly of Magnetic Nanoparticles into Superstructures for Magnonics

Verner Håkonsen

Nanotechnology
Submission date: June 2015
Supervisor: Erik Wahlstrøm, IFY
Co-supervisor: Gurvinder Singh, IMT

Norwegian University of Science and Technology
Department of Physics

ABSTRACT

Magnonics is a young and evolving field with the potential to replace conventional electronics. This field relies on the use of spin waves, or magnons, rather than electrons as the information carrier in logic devices, which brings along advantageous features when it comes to device performance. However, to accurately control and manipulate magnons, periodically patterned magnetic materials are needed, conventionally obtained by top-down methods such as the deposition of a magnetic thin film followed by critical patterning steps, which are both time consuming and expensive.

The bottom-up method of liquid-air interface self-assembly in a magnetic field was employed as a simplified method to successfully fabricate ordered one-dimensional magnonic structures, consisting of 12 nm magnetite nanocubes. This method offers great flexibility in terms of the direction and strength of an applied magnetic field, as well as the size, morphology and concentration of the nanoparticles involved. In addition, Markov Chain Monte Carlo simulations utilizing the Metropolis-Hastings algorithm, was performed to simulate and gain insight to the self-assembly mechanism.

Two types of one-dimensional structures were considered, namely horizontal lines and vertically aligned rods. Volumetric solvent amount studies at fixed uniform magnetic fields, a uniform field study at fixed volume and an oleic acid surfactant concentration study was performed in the context of line-formation. Optimal magnetic field strength and total dispersion volume were established for narrow separated monolayered lines. Lines also seem to adapt a nanocube configuration corresponding to the [100]-direction parallel to the applied magnetic field for values below 750 G, and a [110]-configuration for values above 750 G, in excellent agreement with simulation results. Vertical gradient magnetic fields were investigated, resulting in superstructured rods. Experimentally, studies performed with varying magnetic field strengths and gradients, as well as concentration of nanocubes and dispersion volume, revealed that the level of one-dimensionality in terms of aspect ratio tend to increase with increasing magnetic fields, but did not seem to show any clear correlation to the value of the gradient. In addition, increasing both concentration and volume resulted in an increase of aspect ratio.

A proposed magnetic field-induced self-assembly mechanism was established, in which a combination of translational and rotational Brownian motion, magnetic dipole-dipole interactions, magnetocrystalline anisotropy, as well as increasingly stronger van der Waals attractions with increasing oleic acid concentration upon evaporation, served to explain obtained ordered superstructures. Experiments supported by simulations demonstrate that the final stage of the process in pure oleic acid, is imperative for long range ordering, in which the final obtained

structure is a compromise between van der Waals interactions and magnetic dipole-dipole interactions.

Ferromagnetic resonance (FMR) was utilized to magnetically characterize obtained magnonic structures. Second peaks presumably corresponding to low k magnonic modes were observed for all samples considered, most probably with the applied field in the lengthwise direction in case of the one-dimensional structures. Shape anisotropy was well expressed in case of the one-dimensional structures.

SAMMENDRAG

Magnonikk er et ungt og utviklende felt som har potensial til å erstatte konvensjonell elektronikk. Dette feltet avhenger av bruk av spinnbølger, eller magnoner, i stedet for elektroner som informasjonsbærer i logiske komponenter, som gir opphav til fordelaktige egenskaper når det gjelder enhetens ytelse. For å nøyaktig kontrollere og manipulere magnoner, trengs periodiske mønstrede magnetiske materialer, konvensjonelt fremstilt ved ovenfra-og-ned-metoder slik som deponering av magnetiske tynnfilmer etterfulgt av kritiske mønstringstrinn, som er både tidkrevende og kostbart.

Nedenfra-og-opp-metoden væske-luftgrensesnittet-selvorganisering ble anvendt som e forenklet metode for å fabrikkere ordnede endimensjonale magnoniske superstrukturer, bestående av 12 nm nanokuber av magnetitt. Denne metoden gir stor fleksibilitet med hensyn til retningen og styrken til et påtrykt magnetisk felt, så vel som størrelse, morfologi og konsentrasjon av de involverte nanopartiklene. I tillegg ble Markov Chain Monte Carlo simuleringer ved å benytte Metropolis-Hastings-algoritmen, utført for å simulere og få innsikt i selvorganiseringsmekanismen.

To typer endimensjonale strukturer ble tatt i betraktning, både horisontale linjer og vertikalt innrettede staver. Studier av løsningsmiddelvolum ved konstante uniforme magnetfelt, en uniform feltstudie ved faste volumer og en studie av oljesyre surfaktantkonsentrasjon ble utført med fokus på lineformasjon. Optimal magnetfeltstyrke og total dispersjonsvolum ble etablert for smale separerte linjer som var et monolag tykt. Linjer ser også ut til å uttrykke en nanokubekonfigurasjon som svarer til [100]-retningen parallelt med det påtrykte magnetiske feltet for verdier under 750 G, og [110]-konfigurasjon for verdier over 750 G, i utmerket overensstemmelse med simuleringsresultater. Vertikale magnetiske gradientfelt ble undersøkt, noe som resulterte i superstrukturerte staver. Eksperimentelt, avslørte studier utført med varierende magnetiske feltstyrker og gradienter, samt konsentrasjon av nanokuber og dispersjonsvolum, at nivået av endimensjonalitet i form av høyde-tverrsnitt-størrelse-forhold har en tendens til å øke med økende magnetfelt, men ser ikke ut til å vise noen klar korrelasjon til verdien av gradienten. I tillegg resulterte en økning av både konsentrasjon og volum i en økning av høyde-tverrsnitt-størrelse-forhold.

En foreslått magnetfeltindusert selvorganiseringsmekanisme ble etablert, hvor en kombinasjon av translasjonelle og rotasjonelle Brownske bevegelser, magnetiske dipol-dipol interaksjoner, magnetokrystallinsk anisotropi, samt stadig sterkere van der Waals attraksjoner med økende konsentrasjon av oljesyre ved fordampning, forklarte de resulterende superstrukturene. Eksperimenter støttet av simuleringer viser at det siste trinnet av prosessen i ren oljesyre, er avgjørende for ordnede

strukturer med lang rekkevidde, hvor den endelige oppnådde strukturen er et kompromiss mellom van der Waals interaksjoner og magnetiske dipol-dipol-interaksjoner.

Ferromagnetisk resonans (FMR) ble benyttet for å magnetisk karakterisere de oppnådde magnoniske strukturene. Sekundære topper, antagelig svarende til lav-k-magnoniske moder ble observert i alle målte prøver, mest sannsynlig med det påtrykte feltet i lengderetningen til de endimensjonale strukturene. Formanisotropi var godt uttrykt i tilfellene av en-dimensjonale strukturer.

PREFACE

This Master's thesis is the result from the Nanotechnology research project TFY4905, comprising a workload of 30 ECTS credits, at the Department of Physics, NTNU. The Master's thesis is based on the previous work and experimental results obtained from the project thesis of the specialization project TFY4520.

In the recent time I found my interest in materials physics, and thus writing a Master's thesis in condensed matter physics, more specifically magnonics, seemed appropriate. Magnonics offers some great potentials in future computer science applications, and is still a rather young and unexplored field. I chose this field specifically because it brings along an excitement and motivation in doing things people have never done before, or at least not published.

I have really enjoyed this period, in spite of the hard work, and learned a lot from it, both on an academic and a personal level. Moreover, as a Nanomaterials student, this project could not have been more suitable to me in terms of my interdisciplinary background in physics, chemistry and material science, where I really got to use all of these scientific areas to solve emerging and challenging problems.

At the end I would like to present a grateful thanks to my supervisors Associate Professor Erik Wahlström and Dr. Gurvinder Singh for excellent guidance and support throughout the entire project. I would also like to thank PhD student Vegard Flovik for help with the characterization technique FMR, PhD student Aleksandar Yordanov Mehandzhiyski for providing an extra computer for simulations, and the technical staff at NTNU Nanolab for great support. The Research Council of Norway is acknowledged for the support to NTNU NanoLab through the Norwegian Micro- and Nano-Fabrication Facility, NorFab (197411/V30).

Trondheim *Verner Håkonsen*
June 2015

ABBREVIATIONS

FIB	Focused Ion Beam
FMR	Ferromagnetic Resonance
EPR	Electron Paramagnetic Resonance
FFT	Fast Fourier Transform
SEM	Scanning Electron Microscopy
TEM	Transmission Electron Microscopy
S(T)EM	Scanning (Transmission) Electron Microscopy
SE	Secondary Electron
MCMC	Markov Chain Monte Carlo
DEG	Diethylene Glycol
NP	Nanoparticle
NC	Nanocube
MFM	Magnetic Force Microscopy
SQUID	Superconducting Quantum Interference Device

CONTENTS

Chapter 1

INTRODUCTION

Ever since the phenomenon of magnetism was described for the first time by Thales of Miletus (about 634-546 BC) as attraction of iron by "lodestone"[1], it has, after being studied and explored over the last 2500 years, made an enormous impact on science as we know it today [1, ch.1]. Important for the widespread interest has been the linking to electricity and as an important constituent of electromagnetic waves, together with a perpendicularly oscillating electric field. Moreover this linkage is due to the theory if relativity, which depends on the motion of charges relative to an observer. There is nevertheless no doubt that many daily used technologies are based on condensed matter magnetism, and that this field is still of great interest today.

Magnetism in condensed matter is a prerequisite for several novel phenomena, such as different types of spontaneous ordering of microscopic **magnetic moments** in a macroscopic solid [2]. Different types of ordered magnetic materials such as **ferro-** and **antiferromagnets**, are certainly imperative in many applications, among them magnetic memory hard drives.

One can ask what it takes for the microscopic magnetic moments in a solid to be ordered. The answer is twofold. First of all, the moments in the material in question has to somehow couple to each other in such a way that they either align in a parallel (ferromagnetic coupling) or an antiparallel (antiferromagnetic coupling) manner. And this alignment, all factors taken into account, has to be energetically favourable. Secondly, the coupling and hence the alignment, has to be left undisturbed to a certain degree. An important competing factor of the magnetic ordering is the temperature of the material, and hence the generation of thermal magnetic lattice excitations, namely **spin waves**. Spin waves causes a disruption of the magnetic order with the result of decreased magnetization, in the case of a ferromagnet. This results in a critical temperature below which the material exhibits ordered magnetic moments (to a certain degree), and above which the material exhibits randomly oriented moments and loses its spontaneous magnetization, that is, in the case of a ferromagnet.

Thermally excited spin waves in an ordered magnetic material are quantized, giving rise to quasiparticle behaviour. These quasiparticles are known as **magnons**, and are bosonic in nature. An apparent question arises; can these disturbances in magnetic order, these magnons, be used to something meaningful in technological terms? The concept of spin waves serving as dynamic eigenmodes of a magnetically

[1] Lodestone is the old English name for the naturally occurring magnetic ore, the spinel **magnetite**, Fe_3O_4.

ordered system was first introduced by Felix Bloch in 1930 [3]. Later it has been studied both classically and quantum mechanically. However, the idea to use spin waves to carry and process information resulted in the emergence of the field of **magnonics** [4], and has over the past decade received considerable attention in the literature. It turns out that magnons can be controlled and manipulated by combining **magnonic structures**, which can result in magnonic devices with behaviour equivalent to conventional semiconductor devices. Thus logic magnonic devices, such as transistors, can be made as a replacement for conventional electronics, with the advantage to transfer and process a signal without actually moving mass. Minimal heat dissipation can thus be expected, leading to higher performance devices. The field of magnonics is young and evolving, but the realization of interesting ideas brings along some great technological potentials in, most importantly, computer science.

As an important prerequisite for spin waves, the discovery of magnetic resonance has had a profound influence of many areas in science and technology [5, ch.13]. One of the oldest and probably most time-honoured technique used in the field of magnetic condensed matter is **ferromagnetic resonance** (FMR) [6], in which the first direct observation of spin waves was made[2]. FMR spectroscopy is a microwave-based technique which can excite and detect magnonic modes in magnonic structures.

Energy an propagation of magnons can be controlled and manipulated by introducing periodically structured magnetic materials at the nanoscale[3]. Conventionally, these **metamaterials** have been made by top-down approaches which includes thin film deposition followed by patterning by means of either focused ion beam (FIB) or lithography methods. An example of a reported magnonic system in the literature is the two-dimensional antidot lattice in which holes are etched in the magnetic thin film by means of FIB [8]. By applying an in-plane angle dependent magnetic field, localized or delocalized spin wave eigenmodes may be observed in the lattice upon application of electromagnetic radiation. Other reported two-dimensional magnonic systems are periodic nanopillars or nanodiscs, both obtained by patterning magnetic thin films.

The idea to use **self-assembled** nanoparticles, constituting the magnonic building blocks, has at the time of writing not resulted in any known reports in the literature. As a bottom-up approach, it truly serves as an interesting and, not to mention, simplified and cheaper method to produce magnonic structures at the nanoscale, in which critical time consuming patterning steps are avoided.

As for this project, it will be fully focused on self-assembled nanoparticle systems for magnonics. Self-assembly is conceptually easy and can be used to make high quality nanoparticle **superlattices** [9]. The self-assembly method of choice is **liquid–air interface self-assembly**, in which the particles are self-assembled at

[2]The first direct observations of spin waves was made by J. H. E. Griffiths [7].

[3]The length scales may range from nano- to millimeters, but nanoscale structures are truly more interesting in terms of future computer science.

the interface of a non-volatile liquid and air. Moreover, the method also offers great freedom in terms of the application of a magnetic field, which can result in novel self-assembled patterns [10]. The nanomaterial of choice will be magnetite exhibiting the cubic morphology, which due to this cubic symmetry will make it a more interesting anisotropic system than spherical morphology. Moreover, nanoparticles exhibiting the cubic morphology are rarely reported in the literature making it an interesting subject for further investigation.

The most important aim for this project is to obtain self-assembled one-dimensional magnetic nanoparticle superlattices, that is, one-dimensional magnonic crystals, which eases the investigation of magnonic eigenmodes in these structures. This could be achieved by applying an appropriate uniform magnetic field during the self-assembly process. In reality, the ideal case would be one-dimensional superstructures separated by a sufficiently large distance such that no magnetic coupling between the structures is observed. In addition, **Monte Carlo** simulations will be performed to support experimental results as far as self-assembly goes, and to gain insight to the physics behind the process. As far as magnetic characterization is concerned, FMR spectroscopy will be used in this project as a tool to characterize obtained magnonic structures.

Chapter 2

THEORY

This is an explanatory theory chapter set out to explain concepts important for the reader in the following sections. A convenient way to start is by discussing the origin of magnetism in condensed matter, and how this is related to the properties of magnetic materials and magnonics.

2.1 Origin of magnetism in condensed matter

It has been known for many years that charges in motion give rise to a magnetic field, which thus can act on other charges in motion [2, ch.1],[1, ch.3]. This phenomenon can either be due to the translation of a charge, or rotation around its own axis which is known as spin angular momentum or just **spin**. In condensed matter magnetism the latter is by far more important than the former. In a solid, spin angular momentum can either be associated with the electrons surrounding the nucleus, or the nucleus itself, consisting of both protons or neutrons giving rise to a magnetic field. The rotating charged particles[1] have what is known as a magnetic moment associated with them, the fundamental object in condensed matter magnetism. If a charge is orbiting there will also be a magnetic moment associated with the **orbital angular momentum** of the charge.

2.1.1 Magnetic moments

In classical electromagnetism, the magnetic moment, $\mathrm{d}\boldsymbol{\mu}$, can be associated with a loop of area $|\mathrm{d}\mathbf{A}|$, around which a current I is circulating, given by

$$\mathrm{d}\boldsymbol{\mu} = I\mathrm{d}\mathbf{A}. \tag{2.1}$$

This current can be narrowed down to a single charged particle. The magnetic moment $\boldsymbol{\mu}_\mathbf{L}$, equivalent to a **magnetic dipole**, is related to a charged particle's orbital angular momentum $\mathbf{L}$ through

$$\boldsymbol{\mu}_\mathbf{L} = \gamma\mathbf{L}, \tag{2.2}$$

[1] Neutrons have a net zero charge, but consist of quarks, i.e. charged elementary particles, giving rise to a net observed magnetic moment.

where γ is the gyromagnetic ratio, given by $-e/2m_\mathrm{e}$ in the case of the electron. Thus the magnetic moment of an electron is antiparallel to its spin angular momentum. Now, the smallest orbital angular momentum an electron can have, according to quantum mechanics, is $\hbar$. The absolute value of the smallest orbital magnetic moment[2] associated with an electron with charge $|-e|$ and mass m_e, known as the **Bohr magneton**, μ_B, is thus defined by

$$\mu_\mathrm{B} = \frac{e\hbar}{2m_e}, \tag{2.3}$$

and takes on the value $9.274 \cdot 10^{-24}$ Am^2. Due to the negative charge of the electron, the associated magnetic moment will thus be negative, hence $-\mu_\mathrm{B}$. Now, as the mass of the electron is substituted with the mass of a proton, which is approximately three orders of magnitude larger, the **nuclear magneton** μ_N, becomes three orders of magnitude smaller than the Bohr magneton. Hence the magnetic moment of the electrons is by far the most important, in terms of condensed matter magnetism, than that of the nucleus, and will be responsible for most of the novel phenomena encountered in magnetodynamics.

Consider an electron rotating around its own axis, with spin angular momentum $\mathbf{S}$. The magnetic moment, $\boldsymbol{\mu}_\mathbf{S}$, resulting from the spin is then given by

$$\boldsymbol{\mu}_\mathbf{S} = \frac{-g\mu_\mathrm{B}}{\hbar}\mathbf{S}, \tag{2.4}$$

where g is known as the **g-factor**, a proportionality factor relating the spin and the Bohr magneton to the observed angular momentum, and $\hbar$ is the reduced Planck constant, $h/2\pi$, equal to $1.05 \cdot 10^{-34}$ J $\cdot$ s. The total observed electron magnetic moment, $\boldsymbol{\mu}$, would just be the sum of $\boldsymbol{\mu}_\mathbf{L}$ and $\boldsymbol{\mu}_\mathbf{S}$, as illustrated in Figure 2.1.

The spin angular momentum can couple to the orbital angular momentum giving rise to the **spin-orbit** interaction. The orbital angular momentum tend to force the spin to align in its direction, which thus involves an energy cost associated with non-parallel spin and angular momentum.

If a magnetic moment $\boldsymbol{\mu}$ is placed in a magnetic field $\mathbf{H}$, the energy E of the magnetic moment is given by

$$E = -\boldsymbol{\mu} \cdot \mathbf{H}. \tag{2.5}$$

A variation of the magnetic field with respect to position, a gradient field, causes a net magnetic force, F_M, acting on the magnetic moment, given by

[2] According to quantum mechanics, the smallest angular momentum an electron can have is really $\sqrt{l(l+1)}\hbar$ with the quantum number $l = 1$ yielding $\sqrt{2}\hbar$, but the Bohr magneton is defined by assuming that the smallest angular momentum is $\hbar$ which holds true if only the z-direction is considered.

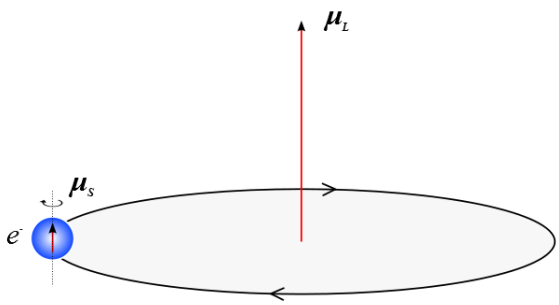

Figure 2.1: An orbiting electron (nucleus not shown) giving rise an orbital magnetic moment $\boldsymbol{\mu}_\mathbf{L}$. The electron also rotates around its own axis giving rise to a spin magnetic moment $\boldsymbol{\mu}_\mathbf{S}$. The magnitudes of the respective magnetic moments are exaggerated to simplify the illustration.

$$\mathbf{F}_\mathrm{M} = \boldsymbol{\mu} \nabla \mathbf{H}, \tag{2.6}$$

asssuming a point magnetic dipole.

2.1.2 The exchange interaction

The **exchange interaction**, or exchange coupling, is an energy term which can be derived from the quantum mechanical consideration of two indistinguishable particles subjected to exchange symmetry, that is, being exchanged [2, ch.4],[1, ch.6]. For **fermions**, exhibiting half integer spin, this involves a positive value and thus a repulsion which is in fact the Pauli repulsion. For **bosons**, exhibiting integer spin, this involves a negative value and an attraction making particles come together, as in Bose-Einstein condensation. In condensed matter magnetism, there exists several types of exchange interactions, short ranged and long ranged, between two spins. The short range interaction is the **direct exchange** and takes place between to neighbouring atoms. The **indirect exchange** is an interaction between two atoms, separated by a third one, and is thus longer ranged. In oxides the oxygen plays the role of the atom in-between two interacting atoms, governing the exchange. Two important indirect exchange interactions are the **superexchange** and the **double exchange**, responsible for antiferromagnetic and ferromagnetic alignment, respectively [2, ch.4]. For two electrons with spins $\mathbf{S_1}$ and $\mathbf{S_2}$, the energy E associated with the coupling between the spins is given by

$$E = -2\frac{\mathrm{J}}{\hbar^2}\mathbf{S_1} \cdot \mathbf{S_2}, \tag{2.7}$$

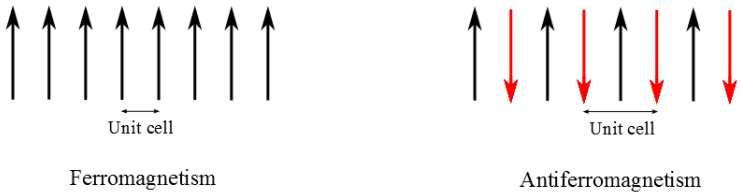

Figure 2.2: Ferromagnetic and antiferromagnetic ordering in one-dimensional magnetic crystals. The magnetic unitcells are indicated with horizontal arrows.

where J is the exchange energy.

2.1.3 Magnetic ordering

As a prerequisite for magnetism, each atom in the solid needs to have an unpaired electron, otherwise the magnetic moments of the paired electrons will cancel each other out, resulting in a net zero magnetic moment. In a three-dimensional solid, electron spins can align spontaneously through the exchange interaction, resulting in magnetically ordered materials. This behaviour is observed in two important systems, namely ferromagnets and antiferromagnets [2, ch.4-5],[5, ch.12].

In a ferromagnet, exhibiting parallel aligned spins, the aligned state is due to positive exchange coupling (see Equation 2.7) between the spins on the respective atoms in the solid, and this state is energetically favourable. Ferromagnetic order can only exist below the **Curie temperature**, T_{C}. Above this transition temperature, the electron spins will be randomly oriented, due to the thermal energy dominating the exchange interaction, causing the solid to lose its magnetization.

Conversely in an antiferromagnet, the energetically favourable state of the solid is antialignment of the unpaired spins on each atom, as a result of a mutual negative exchange coupling (see Equation 2.7) between the electrons, which can be situated on two sublattices with equal and opposite aligned spins. Hence, macroscopic antiferromagnets will seemingly be non-magnetic due to cancelling of spins and thus the magnetic moments in the two sublattices. The corresponding temperature at which magnetic order to disorder occurs for an antiferromagnet is the **Néel temperature**, T_{N}. One-dimensional ferro- and atiferromagnets are displayed in Figure 2.2 with their corresponding magnetic unitcells. In the case of an antiferromagnet, the magnetic unitcell is twice the size as if the spins were parallel aligned. The two antiferromagnetic sublattices are indicated with red and black arrows.

Upon application of an external magnetic field, some materials, initially exhibiting randomly oriented spins, tend to align the spins parallel to the field, and

others tend to align antiparallel to the field. These materials are known as **para-** and **diamagnets**, respectively. Ferro- and antiferromagnets are typically paramagnets above the transition temperature. All materials show some degree of diamagnetism, although this is rarely the dominant behaviour.

2.2 Properties of magnetic materials

Magnetic materials exhibit many interesting properties in terms of how they respond to an applied magnetic field. Some of these properties evolve from magnetic domain walls, magnetic anisotropy and size effects, and have great scientific significance.

2.2.1 Magnetization processes

A macroscopic ferromagnetic material can often show no net magnetic moment in a zero applied magnetic field. This is due to **magnetic domains**, which are small regions in the ferromagnet where the magnetic moments are aligned, and thus shows a saturated magnetization [2, ch.6]. The net moments of the domains are, however, not aligned but randomly oriented, causing a net zero magnetization. Magnetic domains are separated by **domain walls**, which cost energy. The reason for domain formation in the first place, is the **demagnetization energy** associated with the demagnetization field resulting from the divergence of the field at the edges of a sample. This field costs energy, but this energy can be reduced by forming an appropriate number of domains diminishing this field, such that the sum of the energy of both the domain walls and the demagnetization field is smaller than that of the field itself.

As an external magnetic field is applied to a non-saturated sample, domain wall motion is observed in a ferromagnet. This is basically favourable alignment of the magnetic domains with respect to the magnetic field, which ultimately gets to the point where all domains are aligned, and the domain walls are non-existing. If M is the magnetization, defined as the magnetic moment per unit volume of the material, as a result of an external applied field H, this point will be the saturation magnetization M_{s} of the ferromagnet. The magnetization M as a function of the applied magnetic field H behaves as a **hysteresis loop**, shown in Figure 2.3. If the magnetization is saturated and the field is set to zero, the ferromagnet will still exhibit a certain magnetization, known as the **remanent magnetization** M_{r}. The magnetization of the antiferromagnet can be brought back to zero by applying a field with opposite polarity, known as the **coercive field** H_{c}.

Ferromagnetic materials can be categorized into two classes, namely **soft** and **hard magnetic materials**. Whether the material is soft or hard, depends on the magnitude of the coercive field H_{c} of the material. Soft materials have small

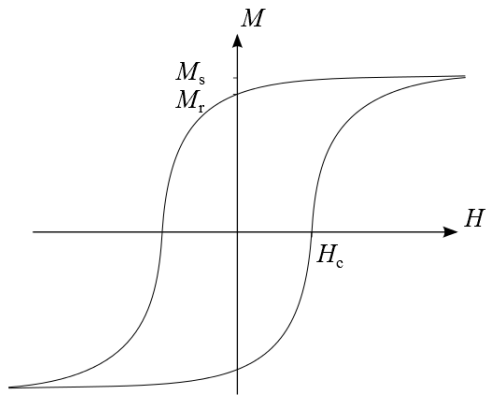

Figure 2.3: The magnetization M of a macroscopic ferromagnet resulting from an applied magnetic field H, behaves as a hysteresis loop. M_s, M_r and H_c is the saturation magnetization, remanent magnetization and coercive field, respectively.

coercive fields, that is, it takes a small field to magnetize the magnet, which also makes the magnetization less stable. Moreover, the remanent magnetization M_r is also small. An example of a soft material is permalloy, a Ni/Fe alloy, with a coercive field of $\sim 2 \cdot 10^{-7}$ T. In contrast, hard materials have both high coercive fields and remanent magnetizations, which makes them suitable for permanent magnets. An example of a hard material is $Nd_2Fe_{14}B$, with a coercive field of 1.2 T.

2.2.2 Magnetic anisotropy

In a ferromagnetic crystal, the spins associated with each atom prefer to align themselves along certain crystallographic directions, along which it would be easier to magnetize the crystal. This direction is known as the magnetic **easy axis** of the material, which in certain materials could be a family of equivalent axes. This suggest that there would also exist magnetic **hard axes**[3], along which it would be hard to magnetize the material, which is indeed the case. The phenomenon is known as **magnetocrystalline anisotropy**, and indicates a certain energy cost associated with the angle of a magnetic moment deviating from the easy axis of the material. This energy cost $E(\theta)$, with the angle θ of the magnetic moment with respect to the easy axis, is to a first approximation given by

$$E(\theta) = KV \sin^2 \theta, \tag{2.8}$$

[3]Some materials have magnetic **intermediate axes** as well.

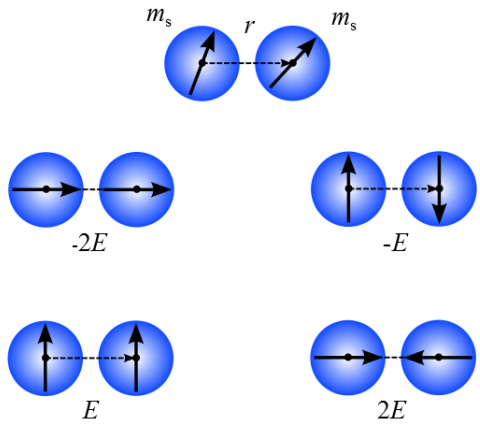

Figure 2.4: The physical origin of shape anisotropy is illustrated by considering four cases involving two particles with a magnetic moment of equal magnitude, μ, separated by a distance r. Different alignments give rise to different energies, both favourable and unfavourable. Here $E = m_s^2/2\pi\mu_0 r^3$.

where K is the anisotropy constant with units J/m^3, and V is the volume of the material in question [2, p.129]. K reflects the anisotropy energy per unit volume and takes on values in the range $10^2 - 10^7$ J/m^3, where lower degree of symmetry of the unitcell acquires higher values. Two examples of materials exhibiting low and high anisotropy energies, are magnetite which has a K equal to $1.1 \cdot 10^4$ J/m^3, and $SmCo_5$ with a K equal to $1.7 \cdot 10^7$ J/m^3, respectively.

Magnetocrystalline anisotropy arises from the spin-orbit interaction, which is larger along certain crystallographic directions and tend to force the spins to align along these particular directions. The larger the difference between the spin-orbit interaction associated with the easy and hard axis, the larger is the energy difference between spin alignment along these axes. This behaviour is of course only observed in ordered systems, and the system becomes effectively isotropic above the Curie temperature.

Magnetocrystalline anisotropy does not alone determine along which direction the net magnetic moment of a sample is directed. The shape of the sample would also contribute to the resulting direction, giving rise to **shape anisotropy**[4]. A spin will align in such a way that the demagnetization field, and hence the energy cost associated with it, is reduced to a minimum. The physical origin of this effect is illustrated in Figure 2.4 where the dipole-dipole interaction energy between two particles with magnetic moments of equal magnitude m_s, separated by a distance r, is considered in four important cases [1, p.508]. In the figure, the relative energies

[4]Other contributions to magnetic anisotropy not discussed in this text are **magnetoelastic anisotropy** [2, p.132] and **exchange anisotropy** [2, p.187].

are shown where E is given by

$$E = \frac{m_{\mathrm{s}}^2}{2\pi\mu_0 r^3},$$

where μ_0 is the magnetic permeability in vacuum, equal to $4\pi \cdot 10^{-7}$ N/A^2. The geometry of a macroscopic magnetic object tends to direct the total magnetic moment of the object in a specific direction such that a maximum number of the constituent building blocks exhibit the configuration with energy $-2E$, that is, lowering the total energy of the system. A specific example would be a rod which tends to direct the total magnetic moment in the lengthwise direction, even though the magnetocrystalline anisotropy prefers the alignment in the crosswise direction. The resulting direction of the net magnetic moment is a balance between those to anisotropies.

2.2.3 Magnetism in nanoparticles - superparamagnetism

Ferromagnetic nanoparticles are too small to exhibit multiple magnetic domains, and will thus comprise only one single domain, or a **macrospin**. The orientation of this macrospin will be dictated by the crystal structure and shape of the particle, as well as the direction of an applied external magnetic field if this is of interest. In fact, if the ferromagnetic particles are small enough, and the temperature is high enough, they will be in the **superparamagnetic** regime in which the magnetic moment can spontaneously flip between equivalent easy axes, if the energy barrier associated with the flip is overcomed by the thermal energy [11]. Assuming a uniaxial anisotropy energy similar to the one in Equation 2.8, the easy directions corresponding to $\theta = 0$ and $\theta = \pi$ are equally favourable, but there is an energy barrier of KV that needs to be overcomed in order to allow flipping. If the magnetization of the particle is measured at a timescale longer than that of the flip, known as the **Néel relaxation time** τ_{N}, the particle will appear to have a zero net magnetization. τ_{N} is directly proportional to a material specific attempt time τ_0[5], and can be approximated by an exponential increase with the energy barrier, given the thermal energy $k_{\mathrm{B}}T$, according to

$$\tau_{\mathrm{N}} = \tau_0 e^{\frac{KV}{k_{\mathrm{B}}T}}, \tag{2.9}$$

where T is the temperature and k_{B} is the Boltzmann constant, equal to $1.38 \cdot 10^{-23}$ J/K. In an external magnetic field, the magnetic moment of an isolated superparamagnetic nanoparticle is locked in the direction of the field, that is, if the field is strong enough. This value depends on several factors, such as the

[5]Attempt times typically lies in the range 10^{-10} to 10^{-9} s.

magnetocrystalline anisotropy and size of the particle, as well as the strength and direction of the applied magnetic field.

The saturation magnetization M_s associated with a nanoparticle is typically smaller than one would expect in terms of its volume, due to surface effects, that is, the spins at the surface do not couple that strongly to the spins of the interior of the nanoparticle and thus become more disordered. The thickness of the disordered surface layer is typically ~ 1 nm [11].

2.3 Magnons

A magnetically ordered system will be perfectly ordered at 0 K, which for a ferromagnet will involve a saturated magnetization, M_s[6]. As for ferromagnetic and antiferromagnetic materials approaching the Curie and Néel temperature, respectively, the systems becomes more and more disordered before eventually undergoing a phase transition, and thus become magnetically isotropic, at their respective critical temperatures. The reason for the apparent drop in magnetic order is thermal collective excitations of electron spin, also known as **spin waves**. Spin waves are quantized due to a finite material size, and have a quasiparticle nature, which is why they very often are referred to as **magnons**. In the following, the notions of spin waves and magnons will be used interchangeably. Before the discussion of magnons is proceeded, an important phenomenon that needs to be addressed is **spin precession**.

2.3.1 Precession

Since it is easier to visualize and sufficient for understanding the behaviour, spin precession will only be treated classically. Precession of magnetic moments [1, ch.3.6] arises as a consequence of a torque $\mathbf{T}$ acting on the magnetic moment $\boldsymbol{\mu}$, situated at an angle θ with respect to the magnetic field direction $\mathbf{H}$, illustrated in Figure 2.5. The resulting torque causes the magnetic moment to rotate, or precess, around the axis of the applied field, and is given by

$$\mathbf{T} = \boldsymbol{\mu} \times \mu_0 \mathbf{H}. \tag{2.10}$$

Now, since the torque is nothing more than the time derivative with respect to angular momentum, $\mathrm{d}\mathbf{L}/\mathrm{d}t$, combining Equation 2.2 and 2.11 yields

$$\frac{\mathrm{d}\boldsymbol{\mu}}{\mathrm{d}t} = \gamma\, \boldsymbol{\mu} \times \mu_0 \mathbf{H}, \tag{2.11}$$

[6] That is, if magnetic domains are disregarded.

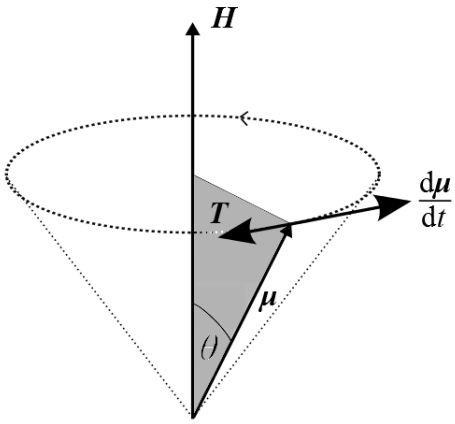

Figure 2.5: Precession of a magnetic moment, $\boldsymbol{\mu}$, associated with an electron occurs in a magnetic field **H**, at an angle θ, as a resulting torque **T** acts on the moment, perpendicular to both the moment and the field. The change in magnetic moment is according to Equation 2.11 directed in the opposite direction of **T** due to a negative gyromagnetic ration γ.

revealing that precession is the change in magnetic moment with respect to time, which is again equal to a vector perpendicular to both the magnetic moment and the magnetic field. This change in magnetic moment, in the case of an electron, is directed in the opposite direction of **T** due to a negative gyromagnetic ratio γ. The frequency ω_{L} at which the moment precesses, known as the **Larmor frequency**, is given by

$$\omega_{\mathrm{L}} = \gamma \mu_0 H, \tag{2.12}$$

and is counter-intuitively independent of the angle θ.

2.3.2 Spin waves and magnons

A magnon is excited by flipping a single spin in a ferromagnetically or an antiferromagnetically ordered material, giving rise to an entity carrying a magnetic moment equal to two Bohr magnetons. This spin-flip is, however, not local but a superposition of spin-flips distributed over the entire magnetic lattice, in which the spin wave oscillates[7]. Classically this will correspond to spins in a magnetic lattice precessing, but each with a phase shift in the Larmor frequency with respect to its neighbours, as illustrated in Figure 2.6 [2, ch.6],[1, ch.11.1],[5, ch.12]. Here

[7] A single local spin flip will not be an eigenstate of the appropriate Hamiltonian, thus a superposition with probabilities adding up to one, is required.

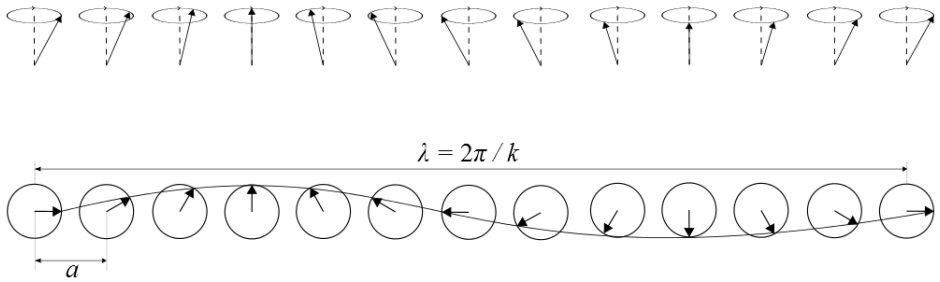

Figure 2.6: Illustration of spin waves in a one-dimensional magnetic lattice with lattice constant a. The top figure displays how the spins precesses around the equilibrium axis, and the bottom displays how the actual wave, with wavelength λ, will look like from above with only the in-plain spin component shown.

the precession of spins on a line with distance a between neighbouring spins, is seen both from perspective in the top figure, and from above in the bottom figure. From above, phase shifts in the spin precession defines a wave, which is the actual spin wave, as shown in the figure for one wavelength λ.

Magnons have integer spin and have therefore the statistical properties of a boson, meaning that several magnons can be in the same quantum state at the same time. This will in turn indicate that, at a temperature above 0 K, it would take a vanishingly small amount of energy to excite long wavelength spin waves, which will cause the ordered magnetic moments to precess, explaining the decrease in magnetization of a ferromagnetic materials at finite temperatures. Thermal excitation of the magnetic lattice will in thermal equilibrium at temperature T, generate an average number of magnons, n_k, in a certain mode with wave vector $\mathbf{k}$ and energy $\hbar\omega_k$, given by the Planck distribution

$$\langle n_{\mathbf{k}} \rangle = \frac{1}{e^{\hbar\omega_{\mathbf{k}}/k_{\mathrm{B}}T} - 1}. \tag{2.13}$$

Magnons can either be excited as **static** or **dynamic** spin waves. The static magnons are modes of standing waves, whereas dynamic magnons will propagate through the magnetic lattice a certain distance, determined by the **Gilbert damping**, that is, relaxation of the spin precession towards the equilibrium axis.

Magnons carries a momentum expressed through the reciprocal wave vector $\mathbf{k}$, and thus have a dispersion relation associated with them. For an isotropic one-dimensional ferromagnet with a distance a between the spins, the energy $\hbar\omega$[8] as a function of the wave number k, is given by the dispersion relation [12]

[8]Magnonic modes can have energies from the meV range to eV range.

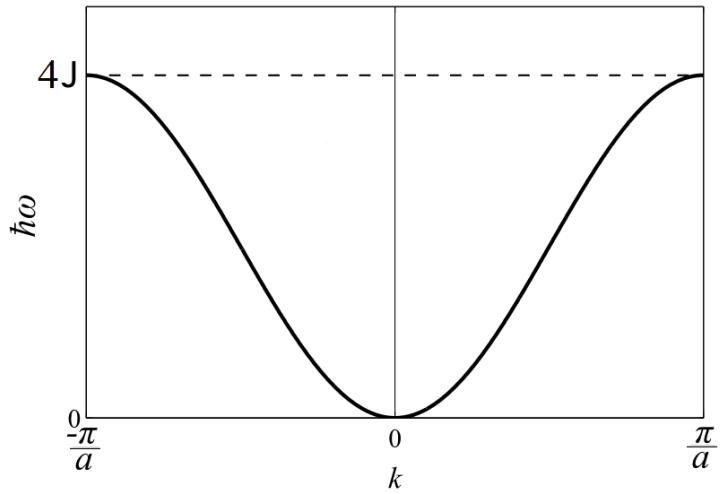

Figure 2.7: The first Brillouin zone is shown in a reduced zone scheme, with the dispersion relation from Equation 2.14 of an isotropic one-dimensional ferromagnet with a distance a between spins. The magnitude of the electron spin is here assumed to be equal to $\hbar/2$.

$$\hbar\omega = \frac{4\mathsf{J}S}{\hbar}[1 - \cos(ka)], \tag{2.14}$$

where ω is the angular frequency of the spin wave, S is the electron spin which can be assumed to take on the value $\hbar/2$, and J is the exchange energy, which as mentioned earlier, is positive in the case of a ferromagnet. This dispersion relation in the first Brillouin zone is shown in Figure 2.7 in a reduced zone scheme. The points $\pm\pi/a$ represent the zone boundaries. As observed, there is no higher energy bands and thus no magnonic band gap associated with this particular magnetic lattice, which will also holds true for tree-dimensional magnetic lattices.

2.4 Ferromagnetic resonance

The principles of ferromagnetic resonance (FMR) spectroscopy has been used extensively in the research of magnetic condensed matter since the beginning of the twentieth century [3]. Although the name suggests that this technique is restricted to ferromagnets, the same technique can be used to investigate several other classes of magnetic materials, although under a different name[9]. FMR employs electromagnetic microwaves to excite electron spin in ordered magnetic samples

[9]Such as nuclear magnetic resonance (NMR), electron paramagnetic resonance (EPR) and antiferromagnetic resonance (AFMR) [5, ch.13].

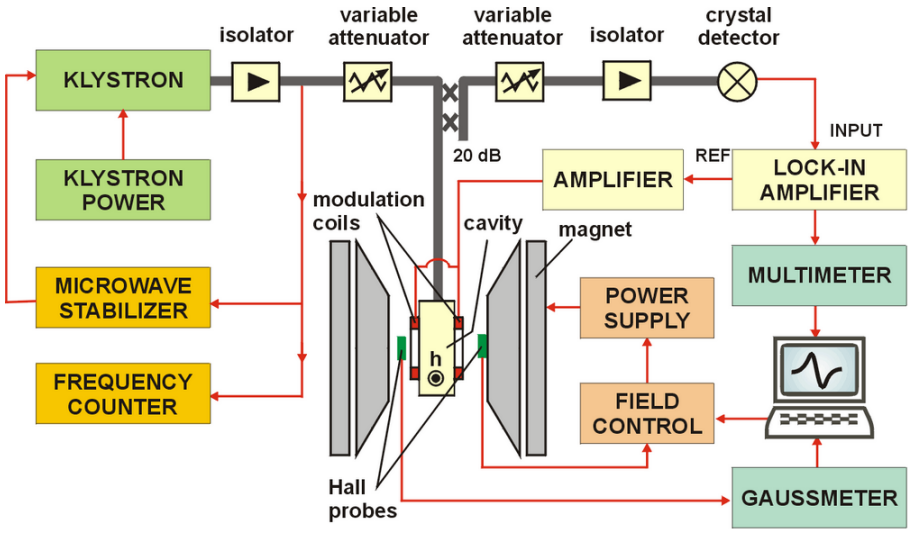

Figure 2.8: A detailed schematic of a typical FMR set-up. The sample is placed in the cavity between two electromagnets, and irradiated with microwaves to excite spin. The reflected microwave signal is detected, analysed and displayed. Taken from [13].

situated in a static magnetic field. Depending on what is the most convenient, resonant excitation can either be obtain at a fixed magnetic field and by changing the microwave frequency to resonant condition is obtained, or keep the microwave frequency fixed and change the magnetic field to resonant condition. In this section the focus will be directed towards the latter scheme.

2.4.1 Set-up

The magnetic sample is placed in a resonant cavity between the poles of two electromagnets and irradiated with microwaves in the super high frequency band, that is, in the range between 3 GHz and 30 GHz [14]. The signal is reflected back and detected, analysed and displayed on a screen. A detailed schematic of a typical set-up can be seen in Figure 2.8. The cavity usually has a rectangular or cylindrical shape, and the microwave frequency is chosen in such a way that standing wave modes in the cavity is obtained. It is important that the actual sample is situated where the magnetic field of the standing wave is uniform in the cavity. In addition the electric field associated with the standing wave, oscillating perpendicular to the magnetic field, can be shifted in such a way that it has a node at the location of the sample in the cavity, by tuning the shape and dimensions of the cavity. This is particularly important in the case of lossy samples to prevent heating, that is, samples such as polar liquids and certain types of semiconductors that can interact

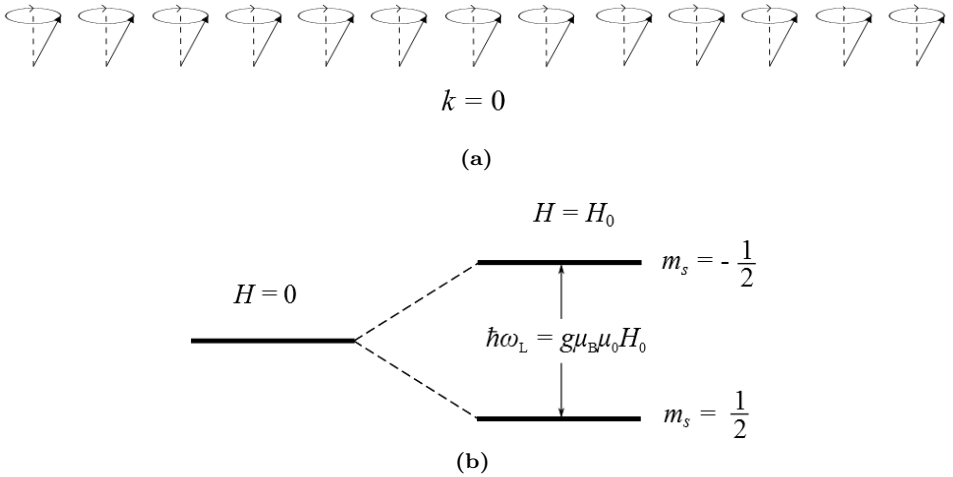

Figure 2.9: Figure (a) shows the uniform precession of a one-dimensional ferromagnetic lattice in perspective. This particular mode corresponds to a wave number k equal to zero. (b) shows the Zeeman splitting of the electron spin states with spin quantum number m_s equal to $1/2$ and $-1/2$.

with the electric field.

2.4.2 Resonance condition

A static magnetic field is applied and swept over a predefined range, in which the resonance should occur, and as a result the magnetic moments of the sample start to precess. The resonant condition is achieved at a certain value of the applied static magnetic field when the precession frequency matches the frequency of the microwave, that is, the Larmor frequency given by Equation 2.12. When this condition is met, the sample will absorb energy from the radiation which will correspond to a peak in the spectrum. The main peak of the ferromagnetic resonance will correspond to the uniform precession of the spins in the sample, that is, the precession of the macrospin associated with the sample. The uniform precession of a ferromagnetic one-dimensional lattice is shown in Figure 2.9a, which corresponds to a spin wave with k equal to zero.

Quantum mechanically, resonance can be described as the excitation of spin, from a state with spin up to spin down, upon absorption of photons from the microwave field [5, ch.13]. The applied magnetic field H_0 causes energy level splitting, commonly referred to as **Zeeman splitting**, between spin up and spin down. For an electron with spin quantum number m_s (not to be confused with the magnetic moment m_s of a particle) equal to $1/2$ and $-1/2$, this splitting energy is

equal to $g\mu_B\mu_0 H$. As the energy difference of the two levels after splitting comes close to the energy of the microwave photons, transition to the higher energy level, and hence resonance, is likely to occur. This is illustrated in Figure 2.9b. In FMR, the spin flip associated with the resonance condition is distributed over the full sample, giving rise to the observed signal peak.

Consider a magnetic geometry consisting of a single crystal with uniform saturation magnetization M_s, and a material g-factor g. Given an external applied magnetic field H_0, the microwave resonance frequency can be calculated according to the **Kittel formula** [6]

$$\omega_0 = \frac{g|\gamma|}{2\pi}\sqrt{[\mu_0 H_0 + (N_y - N_z)\mu_0 M_s]\cdot[\mu_0 H_0 + (N_x - N_z)\mu_0 M_s]}, \tag{2.15}$$

where γ is the gyromagnetic ratio as outlined in Section 2.1.1, and N_x, N_y and N_z are the **demagnetization factors** accounting for magnetization anisotropies. Restricted by the relation $N_x + N_y + N_z = 1$, the demagnetization factors describes how the magnetization is distributed through the sample geometry, which is generally assumed to be an ellipsoid. For instance for a thin film with in-plane magnetization, $N_x = N_z = 0$ and $N_y = 1$. This way for a given material and geometry, the resonance frequency can be predicted at certain applied fields and vice versa.

Resonance is maintained as long as the microwave field is switched on, and of course the static magnetic field. The microwave field is important for compensating the precessional damping in the solid in question [1, ch.3.6]. There are basically two intrinsic damping mechanisms associated with FMR, the first being spin-flip transition responsible for relaxing the component of the spin magnetic moment parallel to the static magnetic field, characterized by the so-called longitudinal relaxation time T_1. The other, being spin de-phasing diminishing the magnetic moment in-plane of the precession, is due to interactions with the neighbouring magnetic moments, and is described by the characteristic transverse relaxation time, T_2. Extrinsic damping is a consequence of lattice imperfections. Damping occurs through orbital angular momentum transfer to another reservoir, which typically involves excitation of spin waves. Ultimately the energy and angular momentum associated with the precession is transferred to the lattice, a mechanism know as **spin lattice relaxation**. This will in turn cause heating of the sample.

In addition to the excitation of the uniform precession, higher energy spin wave modes can also be excited at higher static fields than the uniform precession. These modes could be angle dependent in terms of the direction of the applied field and the geometry of the sample. It is important to note that the reciprocal space, or k-space, comes into play as another degree of freedom in the analysis. Hence at a fixed angle, the system will exhibit a three-dimensional representation, in terms of the applied field, the wave vector and the signal. Initial magnonic modes excited at low magnetic fields in FMR typically show low k-values associated with

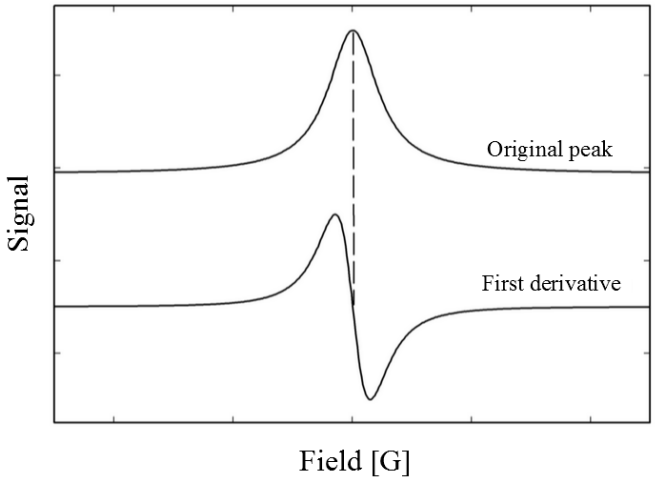

Figure 2.10: A real FMR peak is shown as the top curve, and its associated reported derivative is shown at the bottom. The curves are vertically shifted with respect to each other for easier visualization. Adapted from [15].

them, due to the low k-value the microwaves represent. However, as the static field becomes higher it can couple to the system at k-values given by the periodicity of the magnetic lattice [8].

2.4.3 FMR spectrum

As far as the FMR spectrum is concerned, the width of the resonance peak, that is, the **linewidth**, is associated with damping of the precessional motion and the spin lattice relaxation. The **peak position**, in terms of static magnetic field and its angle with respect to the intrinsic direction of the magnetization, is associated with the gyromagnetic ratio, γ, and magnetic anisotropy. The peak itself can be fitted to a Lorentzian function given by

$$f(H) = I\left[\frac{(\Delta H_w/2)^2}{(H-H_0)^2+(\Delta H_w/2)^2}\right], \tag{2.16}$$

where I is the peak signal, H_0 is the peak position and ΔH_w is the full width at half maximum [1, p.774]. Most commonly, the reported FMR spectrum is the first derivative of the actual peak, due to easier analysis [15]. This is shown in Figure 2.10 in which the two curves are vertically shifted with respect to each other for easier visualization. The horizontal distance between the extrema in the

bottom curve corresponds to the linewidth of the peak, and the root corresponds to the peak position.

2.4.4 Heating

The temperature of the sample should be as low as possible when performing the measurement. Upon heating, either resonant heating from the sample itself or the environment, the ground state is less likely to be occupied than the excited state. Hence, a decreasing sensitivity if the spectrometer will be observed. The resolution will also be diminished, and peaks will not appear as sharp as they would be at lower temperatures. Moreover, it will also be more difficult to observe excitations of higher energy spin wave modes.

2.5 Periodic structures

Novel properties of the magnonic band structure arise upon invoking periodic magnetic superstructures, commonly referred to as magnonic crystals [8, 16]. Magnonic crystals serves as a class of metamaterials, that is, artificially structured materials, which exhibit properties not found elsewhere in nature. By introducing periodicity in a magnetic material through patterning, interesting things happens to the magnonic band structure, namely the splitting of degenerate states causing band gaps in which no magnonic modes are allowed. By changing the size of the periodic components, as well as the periodicity of the superlattice, the band gap could in theory be controlled and tuned as desired, thus creating the possibility to filter out certain magnonic modes. As opposed to photonics and phononics, the size and the direction of the external static magnetic field with respect to the unit axes of the superlattice also serves as an additional degree of freedom, and will have a great influence on the resulting magnonic band structure. Hence, given a magnonic crystal, the magnetic field in itself can be used to manipulate the magnonic band structure.

2.5.1 Magnonic band gap

The magnonic band gap arises through dipole coupling between adjacent magnetic building blocks of the superlattice, like for instance ferromagnetic nanoparticles, giving rise to magnonic modes under the application of a static external magnetic field and microwave irradiation [17, 18, 19]. As for an electron in a periodic potential, it will exist two solutions of the Shcrödinger equation with the same wave vector at the first Brillouin zone boundaries, one eigenfunction localized at the potential minima and the other at the potential maxima, giving rise to an energy difference corresponding to the band gap [5, ch.7]. In analogy of the electron in a

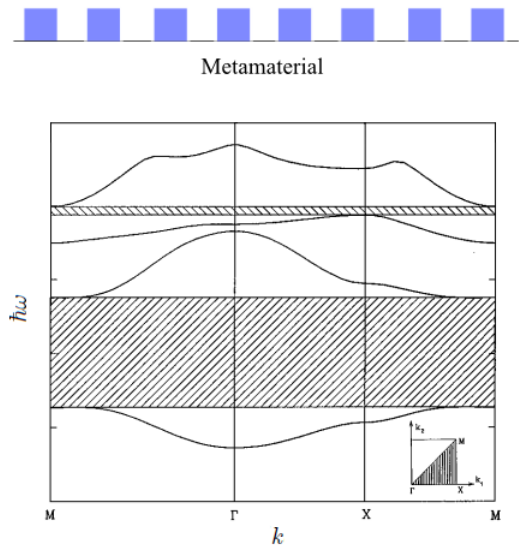

Figure 2.11: A magnetic matamaterial, which in this case corresponds to periodic Fe cylinders in a EuO matrix, gives rise to band gaps (shaded areas) in the magnonic dispersion relation. Four bands are shown in the high-symmetry directions of the two-dimensional Brillouin zone, shown in the inset. Adapted from [20].

periodic potential, there will exist two static magnetic modes at the Brillouin zone boundaries of a magnetic superlattice with periodic magnetization, being standing waves, each with the same wave vector localized at the magnetic components and in between, respectively. The magnon localized between magnetic elements have a higher energy than the magnon localized at the magnetic elements, thus having the same wave vector will give rise to a band gap between the states. An example is given in Figure 2.11 in which the magnonic band structure is calculated for periodic Fe cylinders in a EuO matrix [20]. Four bands are shown in the high-symmetry directions of the two-dimensional Brillouin zone, shown in the inset, and the shaded area corresponds to the band gaps.

The key parameter governing dipole coupling between adjacent magnetic components of the superlattice, is the length scale of the separations. If the distance between the building blocks is too large, the dipole coupling will be weaker, and hence more narrower bands arise with associated larger band gaps. Localized magnonic modes will be expected in this case in analogy to localized electrons in a strong periodic potential. The size of the magnetic elements of the superlattice will also have an influence since these posses the component spin of the superlattice, which scales with size. Thus the bigger the size, the stronger is the dipole coupling.

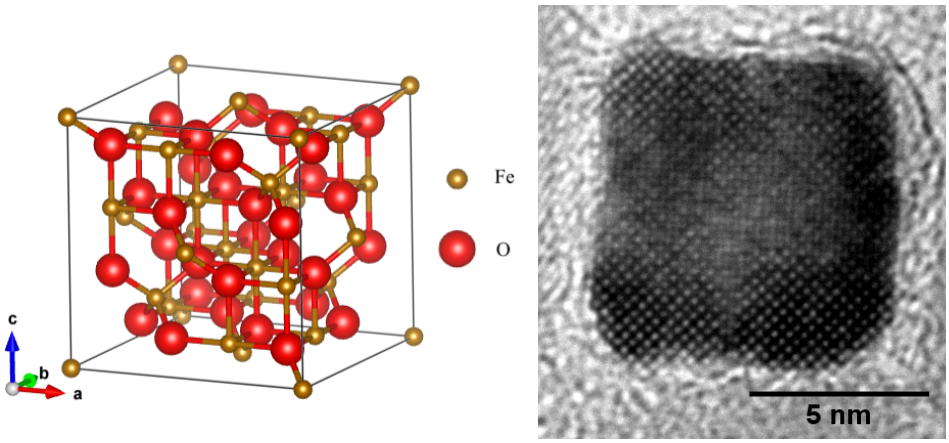

(a) **(b)**

Figure 2.12: The crystal structure of magnetite. Figure (a) shows a schematic of the fcc unitcell displaying bonds between Fe and O. Gold-colored and red spheres correspond to Fe and O, respectively. (b) shows a transmission electron micrograph of a 12 nm cubic nanoparticle in which the lattice is visible. (Courtesy of Gurvinder Singh.)

Due to the high exchange energy, higher frequency magnetic modes occurring within the actual building blocks, and not as an interaction between them, can be disregarded, thus only considering the superlattice as a whole and the macrospins associated with its components is necessary.

2.6 Magnetic properties of magnetite

The magnetic oxide magnetite is the oldest magnetic material known, and has been a material of interest through hundreds of years [1, p.283-284]. With chemical formula Fe_3O_4 it belongs to the spinel group, that is the inverse spinel crystal structure to be precise, and comprises 4 O-anions and three inequivalent Fe-cations, in which two of the Fe-cations are of valence 3+ and the third of valence 2+. The crystal structure, shown in Figure 2.12a, shows how O^{2+}-ions forms an fcc-lattice with the Fe-ions located at interstitial sites, something that is also reflected in the transmission electron micrograph of a 12 nm nanocube in Figure 2.12b. Half of the Fe^{3+} together with all of the Fe^{2+} occupies octahedral sites, whereas the other half of the Fe^{3+} occupies tetrahedral sites, as seen in Figure 2.12a. It is also worth noting that all three Fe-ions bonds to one single O^{2-}-ion, thus both superexchange and double exchange coupling between Fe-ions can occur, giving rise to **ferrimagnetism**.

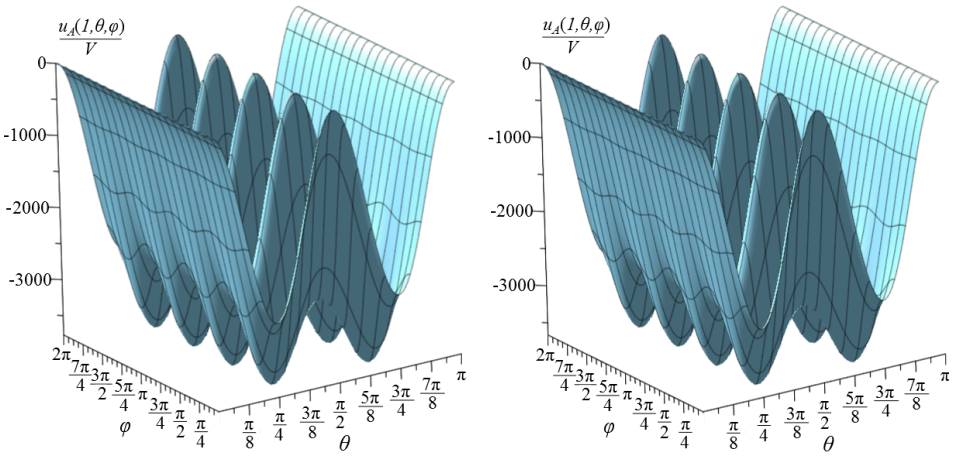

(a) Exact **(b)** Approximation

Figure 2.13: Magnetite magnetocrystalline anisotropy energy reduced with respect to volume, $u_{\mathrm{A}}(r,\theta,\varphi)/V$, with r set to 1, is plotted in a Cartesian coordinate system. a) displays the exact energy landscape with both quartic and sixth-order terms from Equation 2.17, while b) displays only the quartic term.

A ferrimagnet is basically an antiferromagnet in which the two magnetic sublattices posses opposite but unequal spin, magnitudewise. Macroscopically it will look like a ferromagnet and basically have the same magnetic properties as a ferromagnet. The Fe^{2+} and Fe^{3+}-ions at the octahedral sites couples ferromagnetically with each other, but antiferromagnetically to the Fe^{3+}-ion at the tetrahedral site. This results in a net dipole moment[10] per magnetite unit cell. Magnetite has the highest known Curie temperature of 858 K, above which it becomes a paramagnet [21]. Bulk saturation magnetization for the material is $4.80 \cdot 10^5$ A/m [22] with a g-factor equal to 2.12 [23]. As for magnetite nanoparticles, the isolated nanoparticle will be in its superparamagnetic state for sizes under 26 nm at a temperature ~ 300 K, assuming spherical shape [11].

In terms of magnetocrystallinity, magnetite exhibits easy, intermediate and hard axes along the crystallographic directions [111], [110] and [100] of the unit cell, respectively. Magnetite is also considered a soft magnetic material, with a rather small coercive field of ~ 0.2 mT [24]. This is a direct consequence of the magnetocrystalline anisotropy energy, u_{A}, which for bulk magnetite with a volume V is given by

[10] A dipole moment of $4\mu_B$ to be precise.

$$u_{\mathrm{A}}(\mathbf{M}') = K_{\mathrm{A1}}V\left[(M'_xM'_y)^2 + (M'_xM'_z)^2 + (M'_yM'_z)^2\right] + K_{\mathrm{A2}}V(M'_xM'_yM'_z)^2, \tag{2.17}$$

where $\mathbf{M}'$ is the unit vector of the magnetic moment with reference to the unit cell, and the quartic and a sixth-order anisotropy constant, $\mathrm{K_{A1}}$ and $\mathrm{K_{A2}}$, are both negative and equal to $-1.1 \cdot 10^4$ J/m^3 and $-2.8 \cdot 10^3$ J/m^3, respectively [25, ch.2],[22, 26]. Since the magnetocrystalline anisotropy scales with volume, it would be harder to magnetize the material along the hard axes as larger and larger volumes are considered. What can be observed is that the quartic term is about four times larger than the sixth-order term, and it would therefore be reasonable to think that this term could be neglected from Equation 2.17. Since $\mathbf{M}'$ is a unitvector, it is possible to express it in spherical coordinates as $\mathbf{M}'(r, \theta, \varphi) = (r\sin\theta\cos\varphi, r\sin\theta\cos\varphi, r\cos\theta)$, where r is the radial distance, θ is the polar angle and φ is the azimuthal angle. By setting r equal to 1 and plotting the volume reduced Equation 2.17 in a Cartesian coordinate system with argument range $\theta \in [0, \pi]$ and $\varphi \in [0, 2\pi]$, both with and without the sixth-order term, it can be seen in Figure 2.13 that the difference is low. Thus, the sixth-order anisotropy term can to a good approximation be neglected. Furthermore, from Figure 2.13 it can be seen that there exist eight global minima with equal depth, with angular coordinates corresponding to each corner of the cubic unit cell, and maxima with angular coordinates corresponding to the edges of the cube.

2.7 Self-assembly of magnetic nanoparticles

Self-assembly is a process in which a disordered system consisting of pre-existing components forms an ordered system as time progresses. The driving force for self-assembly is a lowering of the total free energy of the system, and the assembly happens in thermodynamic equilibrium [27, 28]. For the convenience of this work, the emphasis will be put on a system with magnetic nanoparticles, which does not exhibit any electric dipole moment, undergoing self-assembly at the liquid-air interface. Due to the small size, as well as steric repulsion of surfactants coating the nanoparticle surface, gravity and Pauli repulsion are not considered in this section.

2.7.1 Liquid-air interface self-assembly

In liquid-air interface self-assembly [9], in the context of nanoparticles as the components of the system, a resulting pattern of higher order than the isolated system ends up deposited at the interface between a liquid and the air.

The method of liquid-air self-assembly utilized a liquid, in which the particles are not dispersible, as a subphase onto which the self-assembled pattern will be

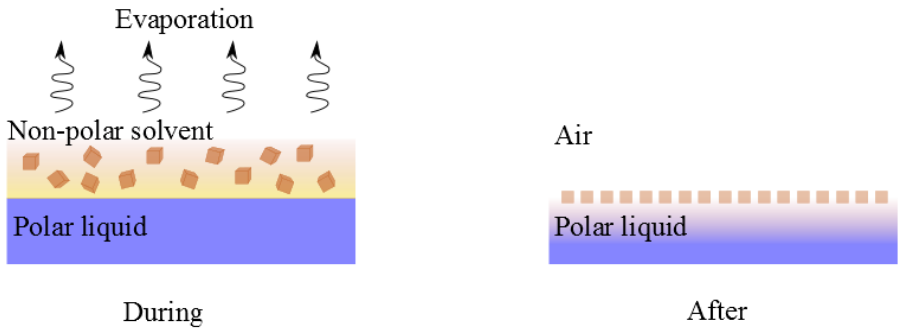

Figure 2.14: During and after liquid-air interface self assembly of nanoparticles with a polar liquid subphase and a non-polar solvent.

deposited at the end of the process. The liquid in question should preferably have both high boiling point and enthalpy of evaporation. The actual nanoparticles, as the disordered system, is preferentially dispersed in a liquid with a lower boiling point and opposite polarity with respect to the subphase. This is achieved by choosing a suitable surfactant with the purpose of both dispersing the particles in the this liquid, and prevent particle agglomeration. As a certain volume of the dispersion is added on top of the subphase, it will spread out forming a thin film which will slowly evaporate. As the volume becomes smaller, the distance between particles decreases until they eventually self-assemble into a more ordered system at the interface between the liquid subphase and air, when all of the solvent has evaporated. The process is illustrated in Figure 2.14 in which nanoparticles are self-assembled from a non-polar phase, in which they are dispersed, and eventually ends up as an ordered system at the interface of the polar liquid and air.

2.7.2 Interactions involved in magnetic field induced self-assembly

At the end of the day, the self-assembly process is just the balance between several driving forces acting internally in the system, and externally on the system in the case of an applied external magnetic field [11]. The interactions acting at the nanoscale are imperative in the self-assembly of nanoparticles. Determination of the magnitude, and thus the significance, of the interaction lies in the length scale at which the particles are situated relative to one another, as well as the size and shape of the particles. The attractive potentials need to balance the repulsive ones and at the same time overcome the thermal energy associated with **Brownian motion** as well as the entropic free energy cost. If this is the case, ordered structures could be obtained.

Brownian motion

Particles suspended in a solvent experiences a very high number of collisions per second from the solvent molecules, due to thermal energy. This causes the a net translational motion, or diffusion, of the suspended particles, something which is commonly referred to as Brownian motion. The displacements could be fitted to a random walk model, which can be used to draw out important statistical information about the overall motion. It turns out that the step size, x, a particle makes in one dimension during a small step time, τ, is normal distributed according to the following expression

$$p(x) = \frac{1}{\sqrt{2\pi D\tau}} e^{-\frac{x^2}{2D\tau}}, \tag{2.18}$$

where D is the diffusion coefficient [29, ch.4]. The mean step size is zero, but the mean square displacement, given by

$$\langle x^2 \rangle = 2D\tau, \tag{2.19}$$

is not, which implies a net displacement proportional to $\sqrt{\tau}$. Given a constant step time τ, the mean square displacement relies on the diffusion coefficient, given by the **Einstein relation**

$$D = \frac{k_{\mathrm{B}}T}{f}, \tag{2.20}$$

where f is the friction coefficient and $k_{\mathrm{B}}T$ is the thermal energy. The friction coefficient is again dependent on the dynamic viscosity η of the surrounding medium, and the size of the moving object. For a sphere of radius R, f is given by **Stokes formula**

$$f = 6\pi\eta R. \tag{2.21}$$

Movement in three dimensions occurs through the sum of independent displacements along the x- y- and z-axis. In addition rotational Brownian motion happens about all three axes, with a normal distributed angular step changing the orientation of the particle [30]. Hence the angular mean square step size, $\langle \theta^2 \rangle$, follows the same rule as Equation 2.19 with D replaced by a rotational diffusion coefficient, D_{r}. D_{r} is in analogy to translation given by the exact same expression as Equation 2.20, but with a rotational friction coefficient f_{r} that scales with the volume of the sphere, R^3, according to

$$f_{\mathrm{r}} = 8\pi\eta R^3. \tag{2.22}$$

Induced dipole-induced dipole interactions

Fluctuation in the electron density of atoms, molecules and particles causes the entity to become an induced electric dipole which can interact with other induced electric dipoles. Named the **London dispersion interaction**, it amounts to one of three possible van **der Waals interactions**, the other two being the induced dipole-dipole interaction (Keesom interaction) and the dipole-dipole interaction (Debye interaction). Only the London dispersion interaction will be considered in this work, and from now on just referred to as the van der Waals interaction.

The **Lennard–Jones potential**, u_{LJ}, reflects the energy associated with both attractive van der Waals interactions and Pauli repulsion, which for two atoms with characteristic atomic diameter σ, separated by a distance r, is given by

$$u_{\mathrm{LJ}}(r) = 4\epsilon \left[\left(\frac{\sigma}{r}\right)^{12} - \left(\frac{\sigma}{r}\right)^{6} \right], \tag{2.23}$$

where ϵ is the depth of the potential well, describing the strength of the interaction. Let the focus be directed towards the attractive fart of the Lennard-Jones potential. When dealing with macroscopic or mesoscopic particles, finding the net attraction requires a sum of all pairwise interactions between atoms, or molecules, in two interacting bodies that are sufficiently close to each other. In the case of cubic bodies with size a, the net van der Waals interaction energy, u_{vdW}, between the two cubes exhibiting a "face-to-face" configuration and center-to-center distance r, is given by

$$u_{\mathrm{vdW}}(r) = -\frac{Aa^2}{12\pi} \left[\frac{1}{(r-a)^2} + \frac{1}{(r+a)^2} - \frac{2}{r^2} \right], \tag{2.24}$$

where A is the **Hamaker constant** [31, ch.10],[32]. The Hamaker constant has the unit of J and reflects the strength of the interaction between two bodies. It also takes the medium between the bodies into consideration, and therefore represents the corrected van der Waals interaction energy in that particular medium. The range of interest is usually $10^{-21} - 10^{-19}$ J. If the Hamaker constants of both the body material and the medium are known, the corrected Hamaker constant A_{212} can be calculated through

$$A_{212} = (\sqrt{A_{11}} - \sqrt{A_{22}})^2, \tag{2.25}$$

where A_{11} is the Hamaker constant corresponding to the interaction between two bodies of solvent in vacuum, and A_{22} is corresponds to the interaction between two bodies of solid material in vacuum. Equation 2.25 states that the effective Hamaker constant can be tuned by choosing the medium in which the objects are allowed to interact. If, for instance, A_{11} and A_{22} have a comparable value, the

effective Hamaker constant A_{212} would be close to zero and the van der Waals interactions effectively screened.

Hamaker constants can be measured experimentally, but since challenges with small length scales and uncertainties in variables make this extremely difficult, theoretical calculations are usually performed. Liquids are typically more difficult in terms of finding the Hamaker constant due to a more disordered state and stronger temperature dependence than a solid. One method is based on the thermodynamics of liquids, and is given by

$$A = \frac{3}{4} k_{\mathrm{B}} T \left[1 - \frac{3 + 6\alpha T}{3 + 7\alpha T} \right]^{-1}, \tag{2.26}$$

where α is the thermal expansion coefficient. This method does, however, assume that dispersion forces dominate the attraction, and thus can not be used for polar liquids.

Steric repulsion

In addition to solvent mediated screening of van der Waals interactions, one other well known way to control the attractive interaction is to choose a suitable surfactant for the system. Surfactants, or stabilizers, are important constituents to tune both interparticle interactions and particle-solvent interactions. The surfactant will adsorb onto the surface of the nanoparticles, and will in so-called "good" solvents have a higher affinity to the solvent molecules than the surfactants on the surrounding nanoparticles, thus giving rise to steric repulsion [33]. Given a surfactant with length L, there exist three distinguishable ranges of interaction in which steric repulsion is significant for stabilized particles with size $a + 2L$. When two cubic particles with a face-to-face configuration are separated with a distance $r > a + 2L$, there exists no interaction. When the particles are further approaching each other, in the range $a + L < r < a + 2L$, free energy of mixing, $u_{\mathrm{mix},1}$, of surfactant chains results in an energy cost given by

$$u_{\mathrm{mix},1}(r) = k_{\mathrm{B}} T \frac{\pi a}{2 V_{\mathrm{s}}} \phi_{\mathrm{av}}^2 \left(\frac{1}{2} - \chi \right) \left[r - (a + 2L) \right]^2, \tag{2.27}$$

where V_{s} is the volume of the solvent molecule, ϕ_{av} is the average volume fraction of the surfactant segment in the volume shell in which the surfactants are located. The Flory parameter, χ, is a dimensionless quantity which describes the strength of the interaction between the surfactants and the solvent, and is further given by

$$\chi = \frac{V_{\mathrm{s}}}{k_{\mathrm{B}} T} (\delta_{\mathrm{solvent}} - \delta_{\mathrm{surfactant}})^2 + \beta, \tag{2.28}$$

where δ_{solvent} and $\delta_{\text{surfactant}}$ with units of $Pa^{\frac{1}{2}}$, are the Hildebrand solubility parameters of the solvent and surfactant, respectively. β is an empirical parameter usually set to the value 0.34 [34]. The third range of interaction is expressed when particles are separated with a distance $a < r < a+L$. In this range the free energy of mixing, $u_{\text{mix},2}$, is given by

$$u_{\text{mix},2}(r) = k_{\text{B}}T\frac{\pi a}{V_{\text{s}}}\phi_{\text{av}}^2\left(\frac{1}{2}-\chi\right)\left[3\ln\left(\frac{L}{r-a}\right)+2\ln\left(\frac{r-a}{L}\right)-\frac{3}{2}\right]. \quad (2.29)$$

In addition, there exist elastic compression of the surfactant tails causing an additional energy cost, u_{elastic}, given by

$$u_{\text{elastic}}(r) = k_{\text{B}}T\pi\nu a\left[(r-a)\left(\ln\left(\frac{L}{r-a}\right)-1\right)+L\right], \quad (2.30)$$

where ν is the number of surfactants per unit area of the particle surface. Hence, the size and structure of the surfactant involved, expressed through L and ϕ_{av}, can be tuned to control the distance at which particles interact.

Magnetic interactions

Magnetic nanoparticles are basically small magnets and can interact with each other through the magnetic dipole–dipole interaction, u_{ij}^{dd}, which for two equal sized particles with magnetic moment unit vectors $\mathbf{M}_i$ and $\mathbf{M}_j$, separated by the distance $|\mathbf{r}_{ij}|$, is given by

$$u_{ij}^{\text{dd}}(\mathbf{r}) = \frac{\mu_0 m_s^2}{4\pi}\left[\frac{\mathbf{M}_i\cdot\mathbf{M}_j}{|\mathbf{r}_{ij}|^3}-\frac{3(\mathbf{M}_i\cdot\mathbf{r}_{ij})(\mathbf{M}_j\cdot\mathbf{r}_{ij})}{|\mathbf{r}_{ij}|^5}\right], \quad (2.31)$$

where m_s is the intrinsic magnetic moment of the nanoparticles [11]. This interaction is weaker when nanoparticles are in the superparamagnetic state than in the ferromagnetic state, due to spontaneous flipping. Of course this interaction is only significant when the nanoparticles are sufficiently close to each other, since it scales with r^{-3}. Each individual particle i, with magnetic moment $m_s\mathbf{M}_i$, will generate a magnetic field $\mathbf{H}(\mathbf{r})$ at a distance $\mathbf{r}$, given by

$$\mathbf{H}(\mathbf{r}) = \frac{m_s}{4\pi}\left[\frac{3(\mathbf{M}_i\cdot\mathbf{r})\mathbf{r}}{|\mathbf{r}|^5}-\frac{\mathbf{M}_i}{|\mathbf{r}|^3}\right]. \quad (2.32)$$

In terms of externally applied magnetic fields [10], ferromagnetic nanoparticles will experience a force trying to line up the magnetic moments in the direction of the field, due to Zeeman coupling. This energy was given in Equation 2.5. If this field

is strong enough, lined up moments will accommodate the magnetic interaction between nanoparticles in such a way that the particles line up in a manner resulting in the lowest possible energy configuration, that is, in a "head-to-tail" manner as shown in Figure 2.4. This way, magnetic field induced self-assembly can potentially be utilized to obtain a high level of ordering in a post-assembled system.

2.7.3 Capillary forces

When most of the solvent has evaporated and the concentration of nanoparticles increases considerably, there will exist capillary forces between the particles, forcing them together. This could either be an advantage or a disadvantage depending on the desired outcome of the process, and could to some degree be controlled by adding excess surfactant to the solution, resulting in a self-assembled nanoparticle pattern embedded in a surfactant matrix.

2.8 Fast Fourier transformation of images

Fast Fourier transformation (FFT) of two-dimensional images is a method often used in image analysis to map out patterns [35]. It relies on an algorithm in which a Fourier transform [36] of intensities in real images are obtained as individual frequencies. Hence, frequencies of the image in real spatial space, is reflected as points in a new image of the frequency space, that is, in reciprocal space.

Common for every FFT is the center point (if the real image is not completely black), named the DC term[11], and its intensity represents the average brightness across the real image. The intensity of the frequency points, compared to center point, reflect to what extent the frequency is expressed in the real image. Higher frequencies in the real image will appear farther from the DC term and lower frequencies will appear closer to the DC term in the FFT. Due to the properties of the Fourier transform, points in the FFT image will always be symmetrical about the center, that is, the upper left quadrant is identical to the lower right quadrant and the upper right quadrant is identical to the lower left quadrant. FFT is illustrated in Figure 2.15 in which a sine wave of constant frequency has been Fourier transformed and given rise to two points in reciprocal space, symmetric about the DC term. Both the real image and the FFT carries all the information needed to obtain either image if only one is at hand. Hence when an image is Fourier transformed, no information is lost, and the process is completely reversible.

[11] DC is an abbreviation for **direct current** and the terminology comes from AC/DC electricity. In case of a DC-current the frequency is zero, hence the center point.

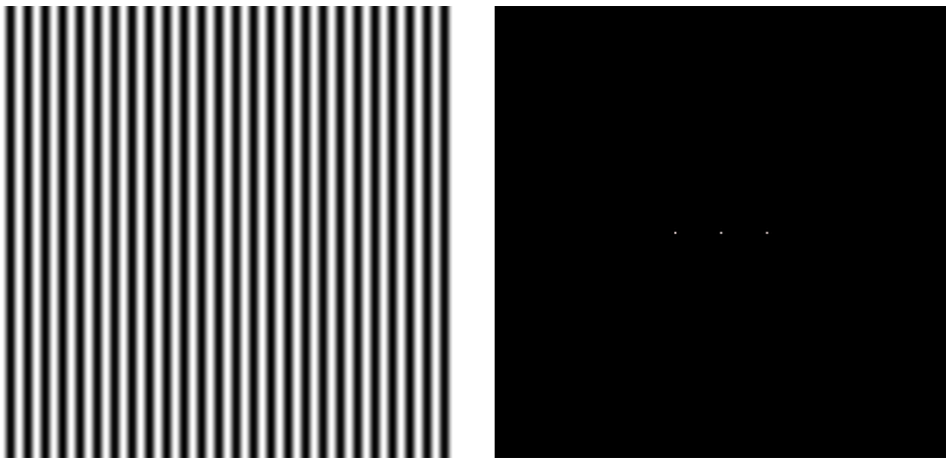

Figure 2.15: The concept of FFT is illustrated by Fourier transforming a sine wave in the left hand image. The FFT image on the right hand side show two points symmetric about the DC term, corresponding to the frequency of the sine wave. Taken from [35].

Chapter 3

MATERIALS AND METHODS

In order to make magnonic crystals, the material of choice was magnetite, a ferrimagnetic oxide. The emphasis was put on a system of monodispersed cubic nanoparticles with a mean size close to 12 nm, exhibiting a standard deviation of only ±2 %. Hence, according to Section 2.6, the size of the particles indicates that they are in the superparamagnetic regime. Details about nanocube synthesis can be found in [22].

Liquid-air interface self-assembly in conjunction with an applied magnetic field was used to obtain ordered structures. The method and all the chemicals used are based on the work of Dr. Gurvinder Sing et al. which have successfully obtained ordered self-assembled structures in a magnetic field [10]. Furthermore, the magnetic field was generated by means electromagnets with the possibility to adjust the field to the desired value, by accurately controlling the current through it with a power supply. The power supply at hand made it possible to generate magnetic fields up to 2500 G[1][2].

A Hitachi S-5500 Scanning Transmission Electron Microscope (S(T)EM), an in-lens cold field emission electron microscope with highest achievable resolution down to 0.4 Å [37], was used to visually characterized the self-assembled structures. This instrument allows for both transmission mode, and high resolution SEM mode in which a detailed images of the sample topography can be achieved. All images were captured in secondary electron (SE) mode, at maximum acceleration voltage and emission current of 30 kV and 20 nA, respectively. If relevant, obtained images were analysed using FFT.

As for magnetic characterization, the method of FMR spectroscopy was applied by using a Bruker Elexsys E 500 EPR-machine[3]. As explained in the beginning of Section 2.4, the same magnetic resonance technique could be used to characterize several types of magnetic materials, although under different names, thus an EPR-machine could be used to obtain ferromagnetic resonance since the material in question behaves as a ferromagnet.

In order to obtain physical insight to the complexity the self-assembly system represents, a theoretical method was applied to simulate the assembly of magnetic nanoparticles, namely Markov Chain Monte Carlo (MCMC) simulations.

[1] $1\,\mathrm{G} = 1 \cdot 10^{-4}\,\mathrm{T}$.

[2] In this thesis, magnetic flux densities are referred to as magnetic fields.

[3] An EPR-machine was used due to newer and more extensive accurate equipment.

3.1 Liquid-air interface self-assembly in a magnetic field

As an initial step, the magnetite nanoparticles were dispersed in non-polar normal hexane (n-hexane), with oleic acid as the surfactant and stabilizer. Shaking and immersion in an ultrasonic bath enabled the dispersion. Excess oleic acid was added to the hexane dispersion to prevent aggregation of nanoparticles during self-assembly, and to embed and stabilize the post-assembled particles in an oleic acid matrix.

A teflon[4] cup with diameter 2 cm and height 2 cm, was filled half full with 2.5 mL diethylene glycol (DEG), serving as the liquid subphase onto which the nanoparticles eventually self-assemble. DEG is a polar liquid and has a boiling point of about 245 °C, thus making it a suitable base liquid onto which the hexane dispersion is added. Immediately after, the magnetic field was switched on, directed at a preferred angle with respect to the liquid level. As n-hexane exhibit a boiling point of about 69 °C, and due to the difference in polarity of hexane and DEG, hexane, being a less dense liquid and more volatile, will float on top of the DEG and evaporate fast. Thus, a lid was put on top of the teflon cup to suppress the evaporation. As the hexane slowly evaporates, the nanoparticles self-assemble into more or less ordered superstructures in the magnetic field, embedded in an oleic acid matrix. The system is left for 10 min per 20 μL of added dispersion, during which the self-assembly process takes place. This would correspond to an evaporation rate close to 30 nm/s, given in decreasing dispersion height per second. Molecular structures of the all the chemicals involved in this self-assembly process can be seen in Figure 3.1 as ball-and-stick models, with the colors white, black, red and blue corresponding to hydrogen, carbon, oxygen and nitrogen, respectively.

The self-assembled film of nanoparticles is more or less useless being situated on top of a liquid, thus a solid substrate is desired, allowing the film to be subjected to subsequent characterisation techniques. Furthermore, this substrate should be a magnetically inert material with as flat surface as possible, to focus the characterization fully on the magnonic structure on the surface. For this purpose, silicon was chosen as the substrate material, onto which the self-assembled film was transferred by means if a lift-off process.

In order to do the lift-off, the nanoparticle film on top of the DEG needs to be accessible, that is, should be close to the rim of the cup, heightwise, such that the substrate easily can be submerged down in the liquid and guided underneath the film prior to the actual lift-off. Moreover, DEG is a rather viscous liquid making this task difficult. This problem is overcomed by simply using a syringe with a polar liquid, being acetonitrile in this case, and gently inject the liquid with the syringe close to the edge of the cup, until the meniscus of the DEG supporting the nanoparticle film is elevated to the rim of the cup. Subsequently, the actual

[4]Teflon was used due to the anti-sticking properties associated with this material.

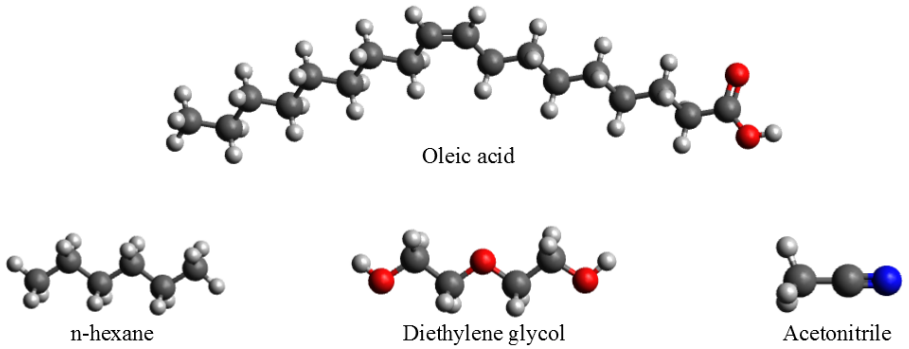

Figure 3.1: The chemicals involved in the self-assembly process. Oleic acid, hexane, diethylene glycol and acetonitrile are shown in the ball-and-stick model, with the colors white, black, red and blue corresponding to hydrogen, carbon, oxygen and nitrogen, respectively.

lift-off can take place by means of a pair of tweezers. During lift-off, the angle of the substrate with respect to the liquid level should not be too high, to prevent crack formation in the film, nor to low, to prevent too much liquid from getting trapped in-between the film and the substrate. An angle of 30 ° with respect to the liquid level is, after trial and error, considered optimal. The lift-off is consistently performed in-field and in the mid region of the film. After lift-off, a wipe was used to absorb excess liquid to allow the sample to dry faster and to accommodate film adhesion onto the substrate. Subsequent drying of the sample in room temperature for a day, or in vacuum for 20 min, ensured that all liquid still left on the sample is removed. The whole process is illustrated in Figure 3.2 as six critical steps.

As a summary, the important parameters in this self-assembly process, which also were to be investigated, are the nanoparticle batch concentration, the oleic acid concentration, the amount taken from the batch, the amount added hexane to the dispersion for dilution prior to the process and thus the total amount of dispersion added in the experiment, and finally the strength and angle of the applied magnetic field. All other parameters were kept constant during the experiments, unless stated otherwise.

When performing electron microscopy, organic features on the surface are easily prone to charging, making the resulting image blurry and unreadable. For this purpose the oleic acid, being an organic surfactant, needed to be removed to such an extent that clear micrographs could be obtained. In order to remove excess oleic acid, a squirt bottle with ethanol was used to thoroughly rinse the sample. Nitrogen gas was used to dry the sample, making it ready for subsequent electron microscopy characterization.

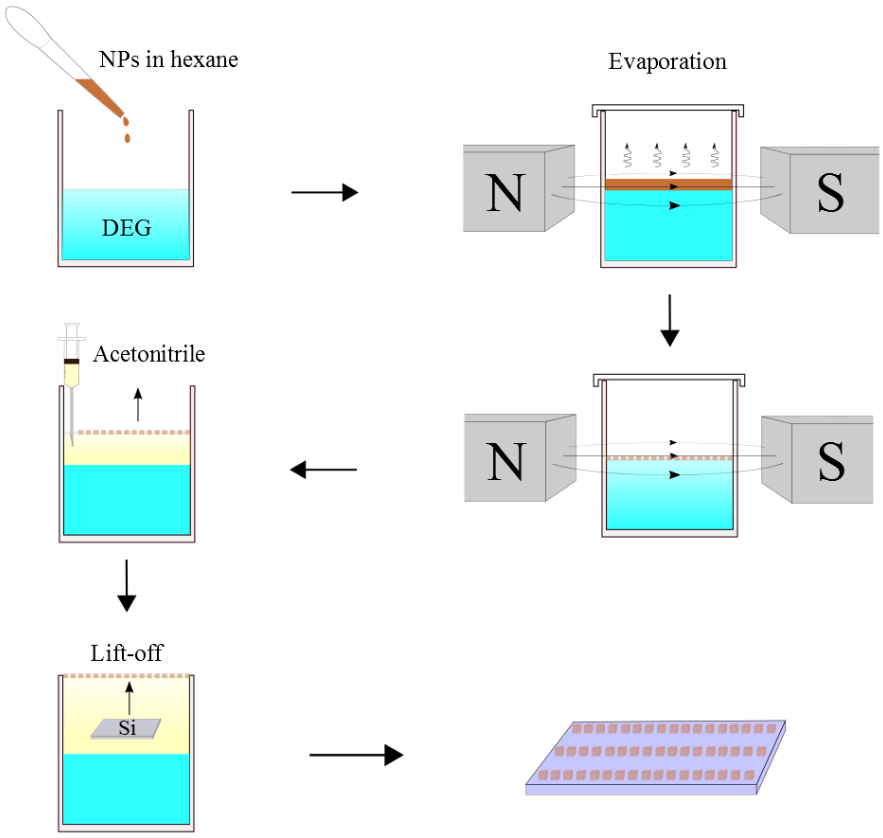

Figure 3.2: The liquid-air interface self-assembly process shown as six critical steps. First the nanoparticle-hexane dispersion is added to the DEG surface, forming a thin film. A magnetic field is switched on immediately after adding the dispersion and a lid is put on. As the hexane evaporates, the nanoparticles self-assembles in the magnetic field and deposit on top of the DEG. Acetonitrile is injected under the nanoparticle film by means of a syringe, to elevate the film. The lift-off is finally done on a Si-substrate, transferring the film from the liquid surface to the solid substrate.

3.2 Monte Carlo simulations

In order to gain insight to the physics behind the self-assembly process, **Markov Chain Monte Carlo** simulations were performed by employing the **Metropolis–Hastings** algorithm [38, 39]. The Monte Carlo method utilizes computational algorithms based on random steps, to find the most likely state of the outcome of a certain process, often mathematical or physical. When

dealing with complex physical systems with coupled degrees of freedoms, this method serves as an excellent tool to analyse everything from various subsystem mechanisms to the system as a whole.

The MCMC method is based on the generation of a Markov chain, which defines a stochastic process of transitions from one state to the next in a predefined state space. The transition probability from a certain state of the system to the next, depends only on the current state and not on previous events. Specifically named the Markov property, this results in a memoryless chain of events, hence the name Markov chain. The Markov chain method can further be divided into subclasses, in which a large and widely used subclass is the Random walk Monte Carlo. In this subclass, the Metropolis–Hastings algorithm is a widely used algorithm and relies on random walks of entities constituting the system. For each iteration the entities are subjected to random movement governed by a probability distribution to new states in state space, a step which is always accepted if the new state is more favourable than the current state and accepted only with a certain probability if the new state is less favourable than the current. By doing a sufficient number of iterations, the system will at the end be at its most favourable state. The Metropolis–Hastings algorithm is particularly useful when dealing with systems of several degrees of freedom which also can be coupled, meaning that a given displacement along one degree of freedom might have an influence of the displacement along the next.

It is important to note that the concept of time does not exist in the Monte Carlo method, but rather the number of steps each entity subjected to movement makes. Hence, a simulated mechanism can not directly rely on time, and time can not directly be used to determine the outcome of a simulation. However, other parameters such as the step size could rely on a predefined step time which can be utilized to give the simulation a more physical character, as well as provide a measure of the accuracy. A specific example is the step time τ from in Equation 2.19 in Section 2.7.2, used to define a mean square step size for both translational and rotational motion.

3.2.1 Implementation

The programming language MATLAB [40] was used to simulate magnetic field induced self-assembly of magnetic nanoparticles according to the MCMC method. Basic constituents of the system are the solvent media confined to a volume box with hard walls, and an ensemble of nanoparticles exhibiting the cubic morphology. Simulations were carried out on a particulate level, and are thus not based on first principles calculations. The system exhibits six degrees of freedom, in which three are translational along the x-, y- and z-axis, and three rotational about the x-, y- and z-axis. All possible vibrational degrees of freedom are not taken into consideration. All translational degrees of freedom are mutually independent, and all the rotational degrees of freedoms are mutually independent. However, there

exists coupling between the translational and the rotational degrees of freedom, meaning one of the types might determine the outcome of the others depending on the order in which they are prioritized.

The nanocubes are positioned at random sites in the defined volume in such a way that they do not overlap, and subsequently given random orientations. They are thereafter subjected to simulated translational and rotational Brownian motion, that is, a random walk model. A step in state space is generated for each degree of freedom for one cube at the time, according to a normal distributed step size. This is given by a random number from the normal distribution multiplied with the square root of the mean square displacement, given by Equation 2.19 in Section 2.7.2 for translational motion, and the same equation with D replaced with D_{r} for rotational motion. The step is always accepted if the next state is energetically favourable, that is, has a lower energy associated with it. If the next state is energetically unfavourable, the step is carried out with a probability given by the Boltzmann distribution, or more precisely the Boltzmann factor

$$\frac{P(E_2)}{P(E_1)} = e^{-\frac{(E_2-E_1)}{k_{\mathrm{B}}T}}, \tag{3.1}$$

which is basically the ratio of the Boltzmann probabilities of finding the system in state 2 (next state) and 1 (current state) [41, ch.10]. Thus, the larger the energy difference between the current state and the next, the lower is the probability for an accepted step.

The total energy of a state is calculated by considering the potentials of several interactions between particles, as well as between the particle itself and the applied magnetic field. Interparticular interactions considered in this model[5] are the van der Waals interactions, free energy of mixing and elastic compression of surfactant chains, magnetic dipole-dipole interactions, Zeeman interactions between the magnetic moment and the applied magnetic field which could be position dependent. In addition, magnetocrystalline anisotropy governing the orientation of the magnetic moment within the cube is considered. Entropy is automatically accounted for through translational and rotational Brownian motion. Different potentials used in this model are summarized in Table 3.1, with their associated parameter values used in the simulations given in Table 3.2. Table 3.2 also reports the viscosities of hexane and oleic acid, as well as the calculated translational and rotational diffusion coefficients. The reader is further directed to Appendix A for details about assumptions and calculations for the parameters.

Interparticle interaction potentials from Table 3.1, with parameters from Table 3.2, are plotted for two 12 nm nanocubes in Figure 3.3 as semilogarithmic plots. Figure 3.3a displays the van der Waals interaction energy between two nanocubes with a face-to-face configuration, both in hexane (blue curve) and oleic acid (red

[5]Interparticle interactions are multiplied with a factor of 1/2 to account for double counting.

Table 3.1: Potentials taken into consideration in the MCMC simulations, as well as the range of interaction (if it exists). References to previous sections in which the potentials were reported are also given. Associated parameter values are summarized in Table 3.2.

Interaction	Formula	Range	Reference
van der Waals	$u_{\mathrm{vdW}}(r) = -\frac{Aa^2}{12\pi}\left[\frac{1}{(r-a)^2} + \frac{1}{(r+a)^2} - \frac{2}{r^2}\right]$	$r > a$	2.7.2
Free energy of mixing	$u_{\mathrm{mix},1}(r) = k_{\mathrm{B}}T\frac{\pi a}{2V_{\mathrm{s}}}\phi_{\mathrm{av}}^2\left(\frac{1}{2} - \chi\right)\left[r - (a+2L)\right]^2$	$a + L < r < a + 2L$	2.7.2
Free energy of mixing	$u_{\mathrm{mix},2}(r) = k_{\mathrm{B}}T\frac{\pi a}{V_{\mathrm{s}}}\phi_{\mathrm{av}}^2\left(\frac{1}{2} - \chi\right)\left[3\ln\left(\frac{L}{r-a}\right) + 2\ln\left(\frac{r-a}{L}\right) - \frac{3}{2}\right]$	$a < r < a + L$	2.7.2
Elastic compression	$u_{\mathrm{elastic}}(r) = k_{\mathrm{B}}T\pi\nu a\left[(r-a)\left(\ln\left(\frac{L}{r-a}\right) - 1\right) + L\right]$	$a < r < a + L$	2.7.2
Magnetic dipole-dipole	$u_{ij}^{\mathrm{dd}}(\mathbf{r}) = \frac{\mu_0 m_{\mathrm{s}}^2}{4\pi}\left[\frac{\mathbf{M}_i \cdot \mathbf{M}_j}{\lvert\mathbf{r}_{ij}\rvert^3} - \frac{3(\mathbf{M}_i \cdot \mathbf{r}_{ij})(\mathbf{M}_j \cdot \mathbf{r}_{ij})}{\lvert\mathbf{r}_{ij}\rvert^5}\right]$	$r > 0$	2.7.2
Magnetocrystalline anisotropy	$u_i^{\mathrm{A}} = K_{\mathrm{A}}\left[(M'_{ix}M'_{iy})^2 + (M'_{ix}M'_{iz})^2 + (M'_{iy}M'_{iz})^2\right]$	–	2.6
Zeeman	$u_{\mathrm{Z}}(\mathbf{r}) = -\mathbf{m}_{\mathrm{s}} \cdot \mathbf{H}(\mathbf{r})$	–	2.1.1

curve). The Hamaker constants for magnetite in both hexane and oleic acid were found to be $2.2 \cdot 10^{-20}$ J and $2.8 \cdot 10^{-19}$ J, respectively, by applying Equation 2.25 (in Section 2.7.2) for the effective Hamaker constant and the associated reported Hamaker constants in Table 3.2. It is important to note that this energy is negative at all separations. The steric repulsion energy is given in Figure 3.3b for interparticle distances in the two regimes $a < r < a+L$ and $a+L < r < a+2L$, for both hexane and oleic acid. As can be seen is that there is a discontinuity between the inner regime where there exists both positive free energy of mixing and elastic compression, and the outer regime in which there only exists free energy of mixing. The energy of the inner regime is typically two orders of magnitude larger than the outer regime. Magnetic dipole-dipole interactions are displayed in Figure 3.3c and 3.3d, for parallel dipoles associated with two identical nanocubes oriented at an angle of 0 and $\pi/2$, respectively. Parallel magnetic moments with angle 0 will at all separations have a negative potential corresponding to an attraction between them, while perpendicular magnetic moments have a positive energy and repel

Table 3.2: Parameters with their associated symbols and values, used in the MCMC simulations. References to the literature in which the parameters were found, or other parameters imperative in the calculations of the ones reported in this table, are also given. Details about assumptions and calculations concerning different parameters are given in Appendix A.

Parameter	Symbol	Value	References
Particle size	a	12 nm	–
Viscosity, hexane	η_{hex}	0.300 mPa $\cdot$ s	[42]
Viscosity, oleic acid	η_{oa}	27.6 mPa $\cdot$ s	[43]
Trans. diffusion coeff., hexane	D_{hex}	$6.85 \cdot 10^{-11}$ m^2/s	–
Trans. diffusion coeff., oleic acid	D_{oa}	$7.44 \cdot 10^{-13}$ m^2/s	–
Rot. diffusion coeff., hexane	$D_{\text{r,hex}}$	$4.55 \cdot 10^{5}$ s^{-1}	–
Rot. diffusion coeff., oleic acid	$D_{\text{r,oa}}$	$4.94 \cdot 10^{3}$ s^{-1}	–
Hamaker constant, Fe_3O_4	$A_{Fe_3O_4}$	$12.6 \cdot 10^{-20}$ J	[22, 44]
Hamaker constant, hexane	A_{hex}	$4.33 \cdot 10^{-20}$ J	[45]
Hamaker constant, oleic acid	A_{oa}	$7.74 \cdot 10^{-19}$ J	[46]
Temperature	T	298 K	–
Chain length, oleic acid	L	2.08 nm	[47]
Oleic acid volume fraction	ϕ_{av}	1	[48, 49]
Molecular volume, hexane	$V_{\text{s,hex}}$	$2.018 \cdot 10^{-28}$ m^3	[42]
Molecular volume, oleic acid	$V_{\text{s,oa}}$	$5.240 \cdot 10^{-28}$ m^3	[49]
Flory parameter, hexane	χ_{hex}	0.364	[42, 50, 34]
Flory parameter, oleic acid	χ_{oa}	0.340	[50, 34]
# of surfactants per unit area	ν	$3.57 \cdot 10^{18}$ m^{-2}	[48]
Intrinsic magnetic moment	m_{s}	$7.47 \cdot 10^{-19}$ Am^2	[22]
Quartic anisotropy constant	K_{A}	$-1.1 \cdot 10^{4}$ J/m^3	[22, 26]

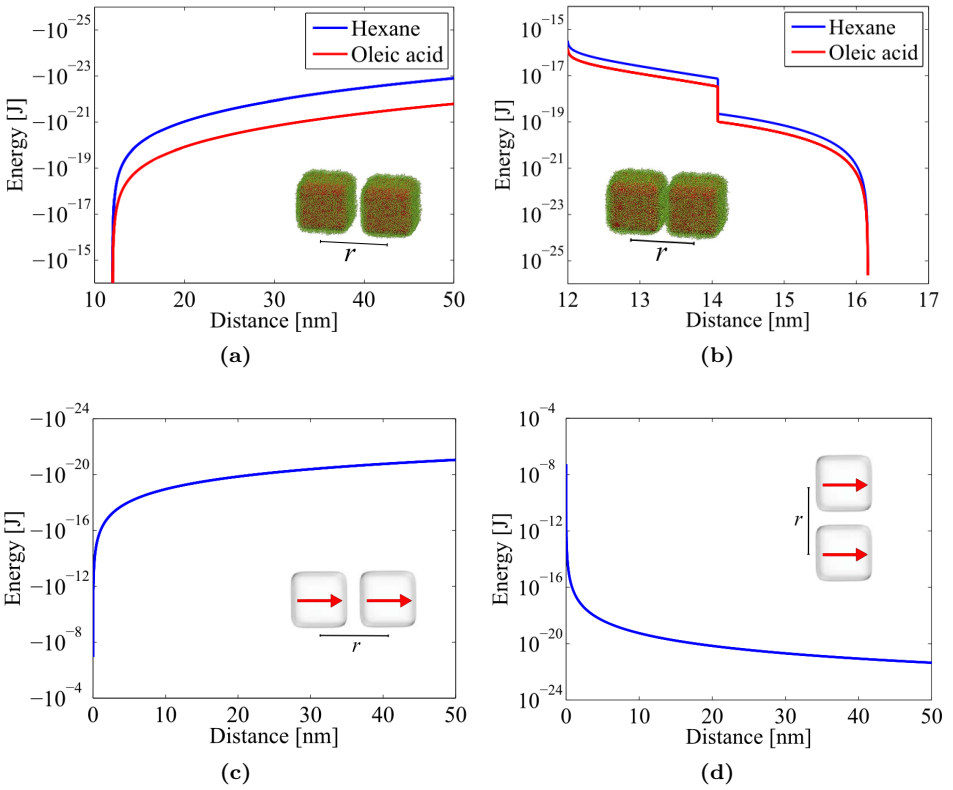

Figure 3.3: Interparticle interaction potentials from Table 3.1, with parameters from Table 3.2, are plotted for two 12 nm nanocubes as semilogarithmic plots. Figure (a) displays van der Waals interaction energies between the nanocubes in both hexane (red curve) and oleic acid (blue curve). The distance is given as center to center distance between the cubes with face-to-face configuration. (b) shows the steric repulsion energy between two nanocubes with face-to-face configuration. (c) and (d) shows magnetic dipole-dipole interactions between the magnetic moment associated with the nanocube at angles 0 and $\pi/2$.

each other at all separations.

The system in question is very complex with several factors affecting a displacement, both in translational and in rotational state space. In order to obtain a model with higher accuracy, evaluation of the displacement to the next state is first given for the rotational degrees of freedom, and finally the translational. When dealing with rotations in this system, several events could happen: Both the nanocube and the magnetic moment could rotate simultaneously, only the nanocube could rotate with the magnetic moment at its current state, or neither

the nanocube nor the magnetic moment rotate. In this regard, only orientation-dependent energy terms are evaluated to find $P(E_1)$ and $P(E_2)$ in Equation 3.1. To cover all the events in the best way, the code is designed in such a way that it initially checks, by applying Equation 3.1, whether only the cube rotate and not the moment, or neither the cube nor the moment rotates. If only the cube rotates, the code proceeds to check whether only the cube rotates, or both the cube and the moment. I both the cube and the moment rotate, the code will do a final check whether this rotation is favourable, or neither the cube nor the moment should rotate. Finally, when the orientation is determined the code checks whether the translational displacement to the next step is favourable. The orientation of the cube will to a certain degree affect the energies involved in this final determination, as there exist energy terms dependent on both orientation and position[6].

Evaporation of hexane is simulated through a decrease of the z-dimension of the volume box, defined by a set evaporation rate. This evaporation rate is again dependent on the step time τ. As the volume decreases for each iteration, hexane evaporates and oleic acid is left behind resulting in an increase of oleic acid concentration. Since solvent viscosity and density changes upon evaporation, so does the mean square step size and interactions such as van der Waals, free energy of mixing and elastic compression (see Figure 3.3). A volume weighted average of parameters constituting the potentials is calculated, to give an approximate corrected interaction in the hexane-oleic acid solution (see Appendix A for more details). As for the mean square displacement, $\langle x^2 \rangle = 2D\tau$, this value is kept constant in such a way that the step time τ is increased when D or D_r decreases as a result of increased viscosity upon hexane evaporation (see Equation 2.20 and 2.21 in Section 2.7.2). This way, the step time increases for each iteration, allowing less computational time to simulate a self-assembly time of for instance 1 s[7].

3.2.2 Assumptions

The code is designed in such a way that the model becomes as physically accurate as possible. However, certain assumptions have to be made in order to make the implementation viable, and computational time acceptable. First of all, the nanocubes are in the model assumed to be perfectly cubic, but in reality they have rounded corners and resemble superellipsoids more than cubes (see TEM image in Figure 2.12b) [22] from Section 2.12. Furthermore, magnetic moments are assumed to be point dipoles, and superparamagnetic effects are neglected. As observed in Table 3.1, the sixth-order anisotropy constant in the magnetocrystalline anisotropy

[6]Potentials given in Table 3.1 both orientation and position dependent, are the free energy of mixing, elastic compression, magnetic dipole-dipole interaction and the Zeeman interaction in case of non-uniform magnetic fields.

[7]In the Monte Carlo method, time does not really exist, but since the mean square step size is directly proportional to the step time τ, which needs to be defined, adding step times for each iteration can be done to get a sense of the physical time elapse of the simulated process.

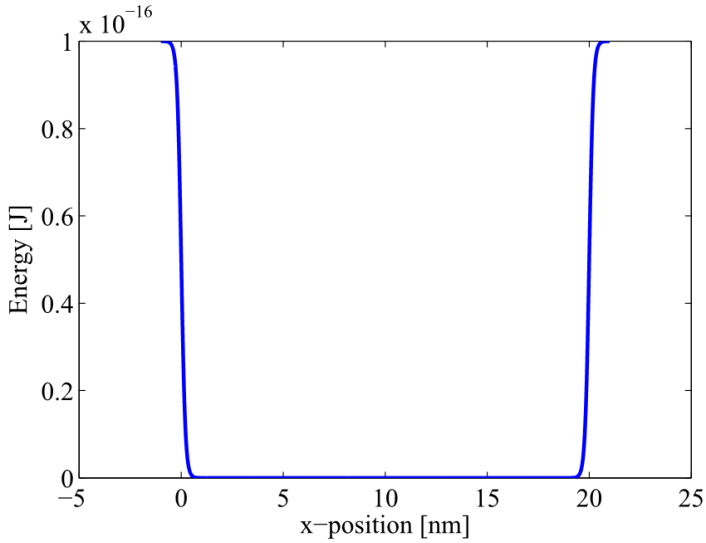

Figure 3.4: Two step functions from Equation 3.2 with k equal to 10 and multiplied with a factor of 10^{-16}, constitute the walls of the volume. In this particular case, the distance across the potential well corresponds to 20 nm, and is only displayed for the x-axis.

term is also neglected, as well as other corrections related to the cubic morphology of nanoparticles.

As far as interactions are concerned, gravity and buoyant forces acting on the nanocubes are neglected. The distance between nanocubes is very unlikely to reach a range in which Pauli repulsion becomes significant, due to steric repulsion, thus Pauli repulsion is neglected. Instead an algorithm written to detect if the magnetite cores of the moving particles overlap, and if so direct the steps of the nanocubes back to their previous respective positions in translational state space, is applied as a safety to prevent cores from merging into each other. However, this algorithm is very unlikely to be employed during the time lapse of the simulation. Furthermore, the van der Waals interaction potential between cubes in Table 3.1 assumes a face-to-face configuration, but is still being used as an approximation to all possible orientations of two interacting cubes. All position dependent interactions between cubes have a distance cutoff of 200 nm beyond which interactions are not considered.

Evaporation is assumed to occur uniformly over the solvent surface, that is, no turbulence is taken into consideration. Furthermore, oleic acid is assumed to be distributed uniformly over the remaining volume. When the volume fraction of oleic acid starts to approach 100 %, the evaporation rate is suppressed by using a step function approximated by $H(\phi_{\mathrm{oa}})$ through

$$H(\phi_{\mathrm{oa}}) = \frac{1}{1 + e^{k_{\mathrm{e}}(\phi_{\mathrm{oa}} - \xi)}}, \tag{3.2}$$

where ϕ_{oa} is the volume fraction of oleic acid, k_{e} is a constant for which a large value determines a sharper transition, and ξ sets the shift of the transition. This is a way to stop the volume decrease when all of the hexane has evaporated, such that subsequent iterations can be performed. How the actual evaporation rate behaves as a function of oleic acid volume fraction remains unknown at this point. Walls comprising the volume would in reality be infinite potentials, assuming inert walls. In the simulations, an approximated step function from Equation 3.2 with k equal to 10 was multiplied with a value of 10^{-16}, comparable to the inner region of the free energy of mixing, $u_{\mathrm{mix},2}$, from Table 3.1 (see Figure 3.3b), which will serve to keep the particles confined inside the volume. Of course, this step function would not be a function of ϕ_{oa}, but the nanocube corner closest to the wall. Figure 3.4 shows how two step functions constitute the walls of a potential well, here along the x-axis. The value of the step function corresponding to the surface of the solvent is multiplied by a factor of 0.9 to ensure that no particles will be pushed through the bottom, but instead be pinned down and immobilized if the height of the volume becomes smaller than the height of the actual self-assembled nanocubes. As mentioned above, interaction parameters are determined by a weighted volume average, something which may or may not be close to the actual values.

3.3 FMR measurements

The sample was scribed to a small square with sides corresponding to 3.5 mm or smaller. Grease was used to adhere the sample onto the bottom of a glass rod with diameter 5 mm if in-plane magnetic fields were desired, or to the wall of a cavity inside the glass rod if perpendicular magnetic fields were desired. The sample should not be to large, as it will disturb the standing wave in the cavity, resulting in a lower output signal. By means of the glass rod, the sample was lowered to the cavity of the EPR-machine. The standing microwave was adjusted to resonant condition by tuning the frequency to about 9.39 GHz and maximizing the amplitude, and thus the output signal.

The measurements were initiated by setting the angle to zero and then do a magnetic field sweep at every angle up to 358 °, with increments of 2 °. At every angle, the field was swept across a predefined interval in which magnetic resonance was expected, with a desired number of data point collected. The attenuation, and thus the microwave power, was set accordingly, to maximize the sensitivity of the signal.

Chapter 4

RESULTS

This chapter will serve to report the results obtained in the process of making one-dimensional magnonic structures by the self-assembly method highlighted in the last chapter, as well as results from Monte Carlo simulations. For convenience, the parameters of the self-assembly process are reported here in this chapter as further analysis and the associated results are based on former results. Line formation was initially investigated using uniform horizontal magnetic fields. First, a systematic study of the volumetric amount of nanoparticle dispersion was performed to find the optimal amount in terms of nanoparticle line formation in the self-assembly process. Later, the optimal strength of the magnetic field was investigated, using the optimal amount of dispersion, followed by an investigation of the structure dependence on the batch concentration of both oleic acid and nanocubes. Subsequent studies were performed with vertical gradient fields to study the potential formation of superstructured rods. Field strength-, gradient-, concentration- and volume studies were performed to investigate rod formation. Monte Carlo simulation were performed at conditions as similar as possible to the experiments, to give insight to the rich physics of magnetic field induces self-assembly. Finally, resulting structures were subjected to FMR spectroscopy, to investigate the occurrence of magnons in these structures.

4.1 Fabricating superstructures by self-assembly

As an initial step in the optimization of one-dimensional structures in the self-assembly process, a control needed to be established in which the self-assembly took place in the absence of any applied magnetic field. In this particular case, the batch concentration of nanoparticles in hexane was set to 2 mg/mL, the oleic acid concentration set to 25 µL/mL, and 20 µL was taken from the batch and added onto the DEG. The parameters are summarized in Table 4.1, in which this particular sample is labeled Sample 0. A high resolution SEM image of this self-assembled structure is shown in Figure 4.1, in which a monolayer of 12 nm magnetite nanocubes can be seen, though only exhibiting short range order. The short range order is also reflected in the FFT, shown in the inset, in which concentric circles appear as a result of small grains with random orientation causing points in reciprocal space to be smeared out.

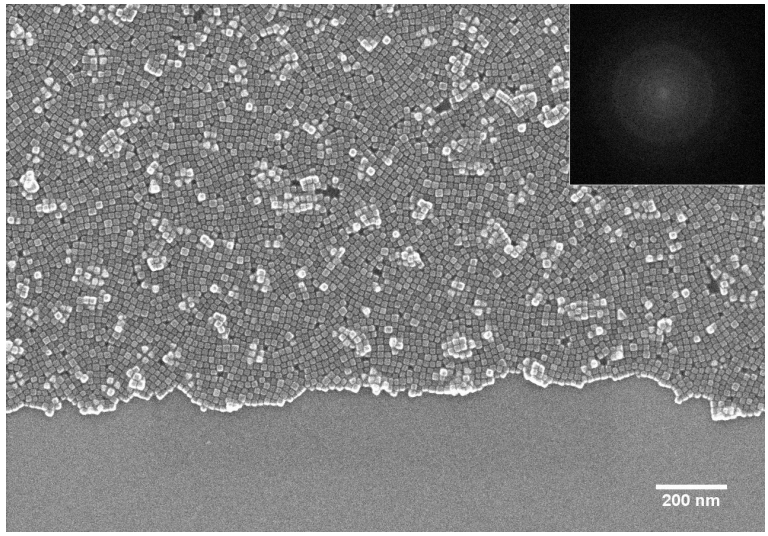

Figure 4.1: Control sample with the 12 nm magnetite nanocubes, self-assembled in the absence of an applied magnetic field. Experimental parameters for this sample, labeled Sample 0, are reported in Table 4.1.

4.1.1 Solvent amount study at 500 G

A solvent amount study was performed to find the optimal amount of dispersion which would result in self-assembled separated lines of nanoparticles. In this study the nanoparticle batch concentration, oleic acid batch concentration, and volume taken form the batch were held fixed at 2 mg/mL, 25 μL/mL and 20 μL, respectively. In addition the field was held fixed at 500 G, such that the only parameters varying from experiment to experiment were the amount of added hexane prior to self-assembly and thus the total amount of dispersion that was to be added in the cup. 5 samples, labeled Sample 2 - 6, with volumetric amounts of added solvent corresponding to 0, 20, 40, 60 and 80 μL, were made. The parameters are summarized in Table 4.1, and the SEM images of the resulting structures are reported in Figure 4.2.

According to Figure 4.2, the total volume of dispersion added seems to have a significance in terms of the resulting self-assembled structures. Figure 4.2a shows that 20 μL resulted in monolayered two-dimensional structures, in which supercrystal grains are clearly visible. The FFT of the monolayered film, displayed in the inset, shows that the grains are randomly oriented as the points are smeared out in circles, in the same manner as for Sample 0. Figure 4.2b shows how the supercrystal grains start to break up with a greater spacing between each other relative to Figure 4.2a. The three-dimensional beam-like structures at the bottom of Figure 4.2b are most probably due to folding of the rim of the nanoparticle-

Table 4.1: The parameters and observed structures with nanocube (NC) orientation and width (W) (if relevant) of the solvent amount study at a magnetic field of 500 G. Strength of the magnetic field, nanoparticle batch concentration, volumetric amount taken from the batch, volumetric amount pure hexane added to the dispersion, the total volume of the dispersion and the observed structure, are reported for Sample 0 - 5. The oleic acid batch concentration was for all samples chosen to be 25 µL/mL.

Sample #	Field [G]	Batch conc. [mg/mL]	Batch amt. [µL]	Amt. added solv. [µL]	Total amt. [µL]	Observed structure
0	0	2	20	0	20	Short range order; monolayer
1	500	2	20	0	20	Grains; monolayer
2	500	2	20	20	40	Grains broken up; monolayer
3	500	2	20	40	60	Lines; monolayer; [100]; W: 6 NCs
4	500	2	20	60	80	Lines; multilayer; W: 500 nm
5	500	2	20	80	100	Lines; multilayer; W: > 1 µm

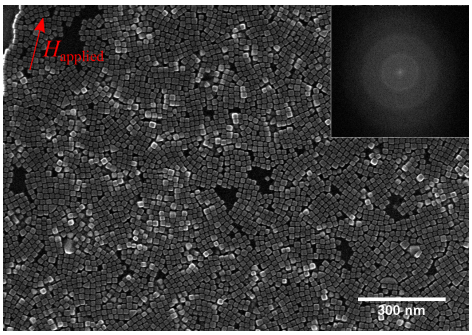

(a) 20 µL

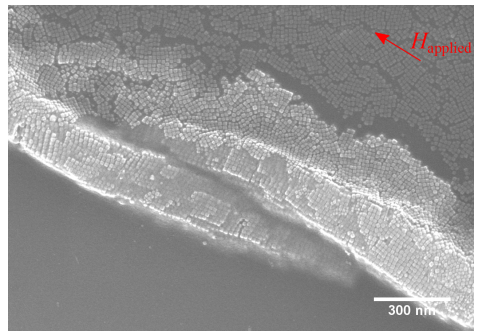

(b) 40 µL

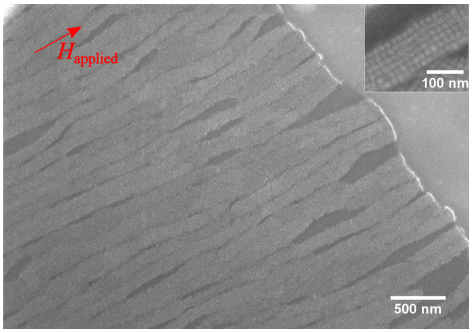

(c) 60 µL

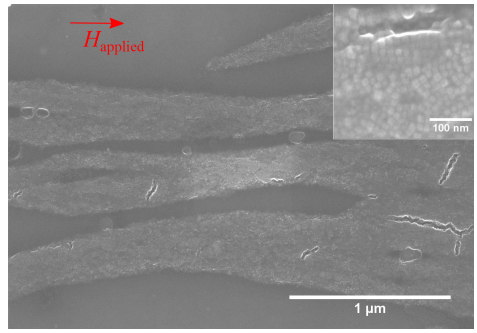

(d) 80 µL

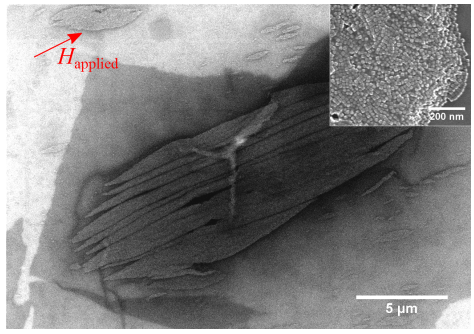

(e) 100 µL

Figure 4.2: High resolution SEM images depicting self-assembled structures obtained from the solvent amount study at 500 G (direction indicated by red arrow), for Sample 1 - 5 with parameters given in Table 4.1. Figure (a) with included FFT, (b), (c), (d) and (e) show the results obtained from self-assembly with a total dispersion volume corresponding to 20, 40, 60, 80 and 100 µL, respectively.

oleic acid film upon lift-off, as a bilayer can be seen terminated close to the beam. Lines with a width corresponding to 6 nanocubes on average, can be observed in Figure 4.2c, in which a total volume of 60 μL was used during self-assembly. The inset reveals that the lines consists of monolayers and the cubes seem to be oriented with the [100]-direction parallel to the applied field. Increasing the volume further to 80 μL seems to yield wider multilayered lines, about 500 nm wide on average, as shown in Figure 4.2d. The inset reveals a rather amorphous surface morphology. Furthermore, even wider and thicker lines appears in Figure 4.2e when the volume was increased to 100 μL. As in 4.2d, the inset reveals a line with an amorphous surface and a thickness of several layers.

4.1.2 Solvent amount study at 2000 G

An additional study equivalent to the one above was performed, this time at a higher field strength corresponding to 2000 G. All parameters, except the amount of added hexane to the dispersion, were kept constant at the same values as in the case of the solvent amount study at 500 G. In addition to the five different solvent amounts reported, a sample was made in which a total volume of 200 μL dispersion was used. The self-assembly parameters of Sample 6 - 11, are reported in Table 4.2, and high resolution SEM images of the these six samples are shown in Figure 4.3.

Figure 4.3a shows that networks of nanoparticle belts are forming already at 20 μL. Moreover, these networks seem to be at least two layers thick. Similar structures are depicted in Figure 4.3b, when the volume of the dispersion was increased to 40 μL, in which the networks appear more stretched out and resembles lines to a greater extent than in the case of Figure 4.3a. By further increasing the dispersion volume to 60 μL, more distinct lines appear in Figure 4.3c, although twisted in a helical manner, which also can be seen in the inset. The lines seem to be around 200 nm wide, more or less overlapping with each other. Shorter and wider lines appear to form when the volume was further increased to 80 μL, as depicted in Figure 4.3d. The inset reveals several layers of nanocubes stacked on top of each other, and the width of the lines seems to range from 0.5 to 1.5 μm. Even wider lines, with widths in the range 1.5 to 3 μm, are depicted in Figure 4.3e, in the case of a total amount of 100 μL. From the inset in this figure, the crack in the depicted line suggests that the number of layers has increased as well with respect to Sample 9. A completely different structure appears as the volume is increased to 200 μL, as in Sample 11. Figure 4.3f reveals in this case the formation of monolayered islands clustered together, with the size of the islands being in the range 0.5 to 1 μm, as also can be seen in the inset.

In general the lines obtained in this study seem to be oriented with [110]-direction parallel to the field, but twisting and more or less amorphous surfaces make it difficult to draw any certain conclusions about the nanocube orientation within the lines.

Table 4.2: The parameters and observed structures with nanocube orientation and average width (W) (if relevant) of the solvent amount study at a magnetic field of 2000 G. Strength of the magnetic field, nanoparticle batch concentration, volumetric amount taken from the batch, volumetric amount pure hexane added to the dispersion, the total volume of the dispersion and the observed structure, are reported for Sample 6 - 11. The oleic acid batch concentration was for all samples chosen to be 25 µL/mL.

Sample #	Field [G]	Batch conc. [mg/mL]	Batch amt. [µL]	Amt. added solv. [µL]	Total amt. [µL]	Observed structure
6	2000	2	20	0	20	Anisotropic networks; multilayer
7	2000	2	20	20	40	Anisotropic networks; multilayer
8	2000	2	20	40	60	Twist. lines; multilayer; W: 200 nm
9	2000	2	20	60	80	Short lines; multilayer; W: $0.5 - 1.5$ µm
10	2000	2	20	80	100	Short lines; multilayer; W: $1.5 - 3$ µm
11	2000	2	20	180	200	Islands; monolayer; W: $0.5 - 1$ µm

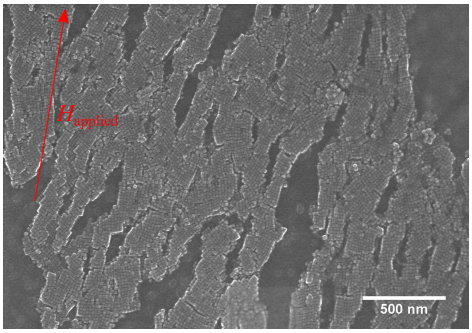

(a) 20 µL

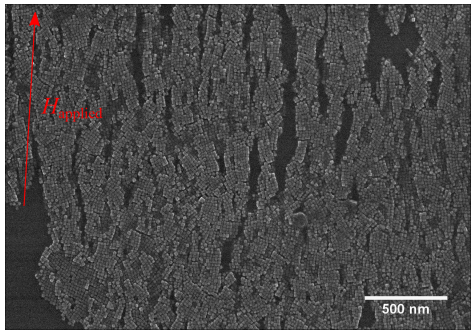

(b) 40 µL

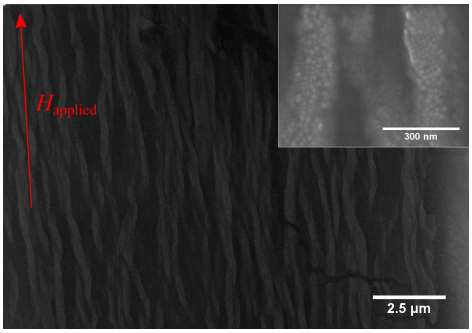

(c) 60 µL

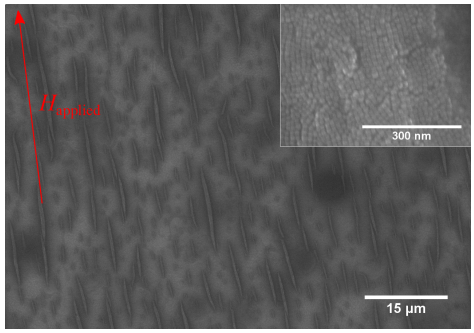

(d) 80 µL

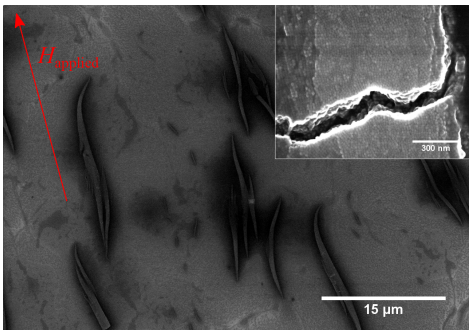

(e) 100 µL

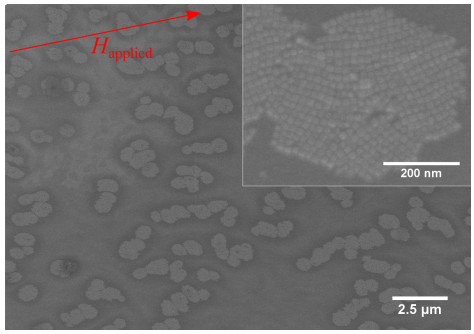

(f) 200 µL

Figure 4.3: High resolution SEM images depicting self-assembled structures obtained from the solvent amount study at 2000 G (direction indicated by red arrow), for Sample 6 - 11 with parameters given in Table 4.2. Figure (a), (b), (c), (d), (e) and (f) show the results obtained from self-assembly with a total dispersion volume corresponding to 20, 40, 60, 80, 100 and 200 µL, respectively.

4.1.3 Magnetic field strength study at a fixed volume

The strength of the applied magnetic field obviously has a profound influence on the formation of one-dimensional superstructures, as seen in the Figures 4.2 and 4.3, from the solvent amount study performed at 500 G and 2000 G, respectively. It may seem from both figures that the optimal conditions, in terms of the total dispersion volume, for obtaining monolayered lines, is 60 μL. Using this knowledge, self-assembly with different magnetic field strengths was performed on six samples, in which the total dispersion amount was held fixed at 60 μL, oleic acid batch concentration held fixed at 25 μL/mL, and the magnetic field set to 250, 500, 750, 1000, 1500 and 2000 G. The parameters are summarized in Table 4.3 for the six samples, labeled Sample 12 - 17.

As these experiments were performed, motion of the oleic acid-nanoparticle film towards one side of the cup was observed upon injection of acetonitrile. This will compress the film such that initially separated lines can be pushed toward each other, and could in addition cause lines to bend or break up. Moreover, it makes the thickness of the oleic acid matrix larger such that removing it sufficiently with ethanol would be more difficult, which in turn could lead to a higher degree of charging in the context of electron microscopy characterization, thus making the lines harder to resolve.

SEM images of resulting structures from the magnetic field strength study are shown in Figure 4.4. Figure 4.4a, depicting the result from the self-assembly at 250 G, shows how lines are indeed forming. However, the inset in this figure reveals that these lines are not monolayers, but consisting of several layers. The lines are squeezed together, exhibiting a width between 100 and 500 nm, and oriented along the [100]-direction with respect to the field. Moving on to Sample 13, self-assembled at 500 G, it can be seen in Figure 4.4b that more narrow lines are forming, with an average width of the most uniform lines being 6 nanocubes, what from the inset also appear to be monolayers with [100]-orientation. The non-uniform width of certain lines is most probably due to merging upon acetonitrile injection. As the field is increased to 750 G, the lines depicted in Figure 4.4c, with widths between 5 and 7 nanocubes, appear more distinct and separated from each other. The inset of this figure shows that the morphology of the lines seems to be a mix of the [100]- and [110]-orientation, with a thickness of at least a bilayer, thus making them less prone to merging as in the case of Figure 4.4b. Self-assembly at 1000 G, in the case of Sample 15, seems to give the lines a more helical-like twist, as shown in Figure 4.4d. However, the width of these lines seems to be approximately the same as for Sample 13 and 14. The excess oleic acid causes a shadow effect which makes the lines appear dark in this image. Figure 4.4e shows the result from the self-assembly at 1500 G. It seems like several narrow lines are squeezed together, still exhibiting a twisting associated with them, as also can be seen in the inset. Finally, at 2000 G, the width of the lines seems to be rather unchanged from the former samples in this magnetic field strength study, and the inset reveals that these lines are not monolayers. Although it is difficult to see due

Table 4.3: The parameters and observed structures with nanocube (NC) orientation and width (W) of the magnetic field strength study at a constant total solvent amount corresponding to 60 µL. Strength of the magnetic field, nanoparticle batch concentration, volumetric amount taken from the batch, volumetric amount pure hexane added to the dispersion, the total volume of the dispersion and the observed structure, are reported for Sample 12 - 17. The oleic acid batch concentration was for all samples chosen to be 25 µL/mL.

Sample #	Field [G]	Batch conc. [mg/mL]	Batch amt. [µL]	Amt. added solv. [µL]	Total amt. [µL]	Observed structure
12*	250	2	20	40	60	Lines; multilayer; [100]; W: $100 - 150$ nm
13*	500	2	20	40	60	Lines; monolayer; [100]; W: 6 NCs
14*	750	2	20	40	60	Lines; multilayer; [100]/[110]; W: 6 NCs
15*	1000	2	20	40	60	Twist. lines; multilayer; [110]; W: 6 NCs
16*	1500	2	20	40	60	Twist. lines; multilayer; [110]; W: 6 NCs
17*	2000	2	20	40	60	Twist. lines; multilayer; [110]; W: 6 NCs

*Film movement observed upon acetonitrile injection.

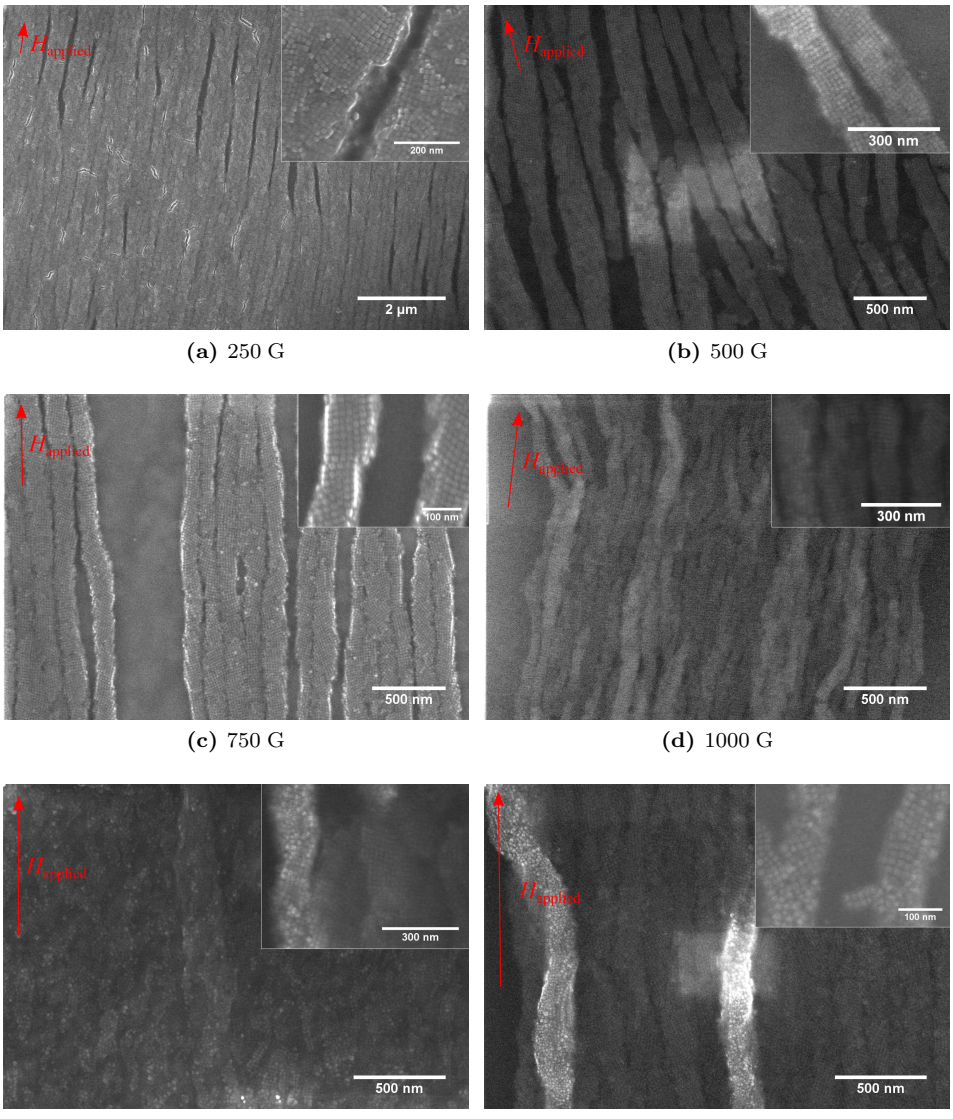

(a) 250 G **(b)** 500 G

(c) 750 G **(d)** 1000 G

(e) 1500 G **(f)** 2000 G

Figure 4.4: High resolution SEM images depicting self-assembled structures obtained from the magnetic field strength study at dispersion volume of 60 µL, for Sample 12 - 17 with parameters given in Table 4.3. Figure (a), (b), (c), (d), (e) and (f) show the results obtained from self-assembly with field strengths corresponding to 250, 500, 750, 1000, 1500 and 2000 G (direction indicated by red arrow), respectively.

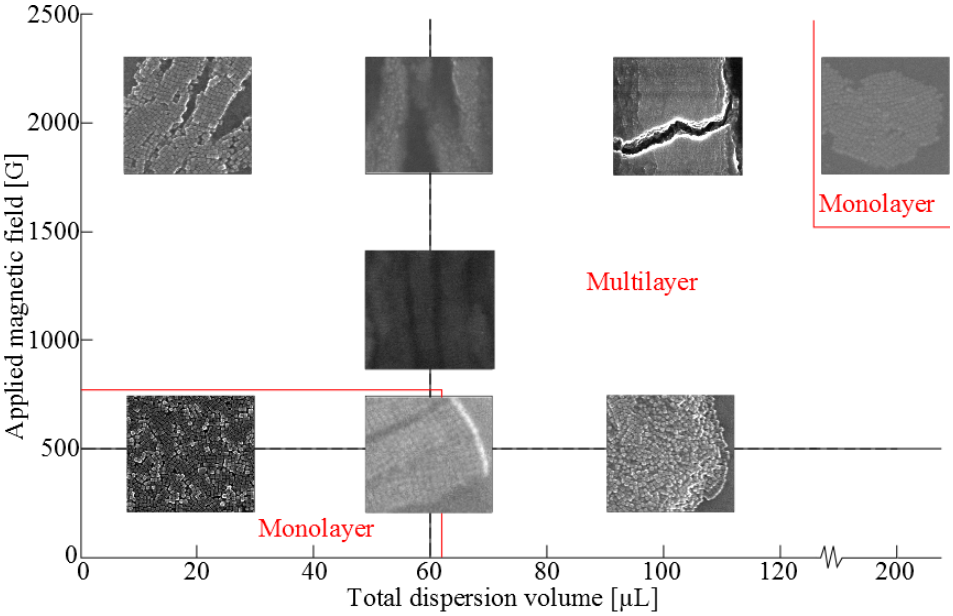

Figure 4.5: Overview of the obtained results from the studies done so far, all at a nanoparticle batch concentration of 2 mg/mL. The optimal total dispersion volume and applied magnetic field are indicated by black solid lines in the diagram. The regions in which monolayers and multilayers were obtained are indicated by red solid lines.

to twisting, the lines in Figure 4.4d, 4.4e and 4.4f seem to show a [110]-orientation with respect to the applied field.

4.1.4 Oleic acid study

Taking into consideration the results from the previous two solvent amount studies and the field strength study, as reported in the Figures 4.2, 4.3 and 4.4, it seems like the amount of solvent yielding the most uniform self-assembled lines, exhibiting just a monolayer, is 60 µL. Furthermore, from the field strength study, around 500 G seems to be the magnetic field strength which results in the most narrow monolayered lines. The results so far are summarized in an overview diagram, shown in Figure 4.5. Here, representative structures are indicated at their associated total dispersion volume- and applied magnetic field parameters. Optimal volume and field are indicated by black solid lines, and regions in which monolayers and multilayers were obtained are indicated by red solid lines.

A study of self-assembly with different oleic acid batch concentrations was performed to investigate the significance of oleic acid concentration on the

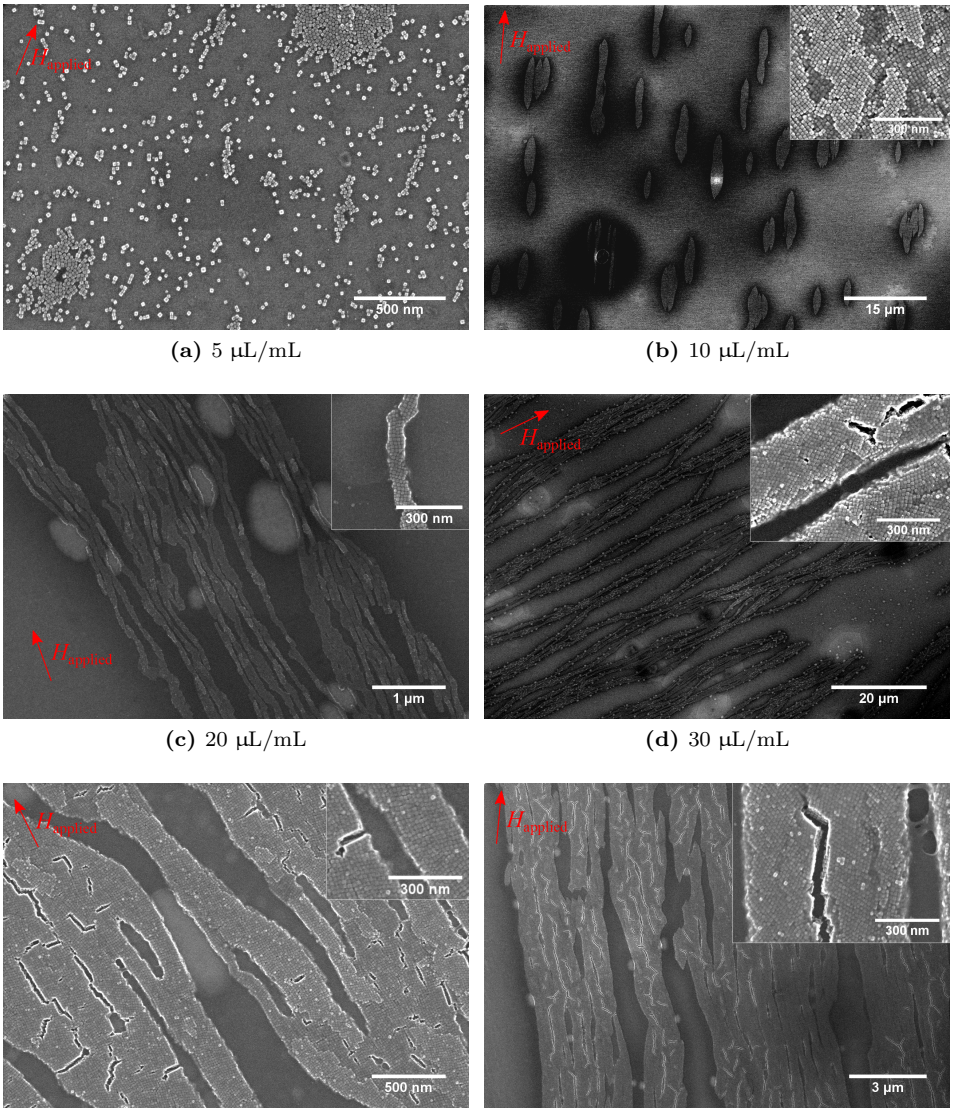

(a) 5 µL/mL **(b)** 10 µL/mL

(c) 20 µL/mL **(d)** 30 µL/mL

(e) 40 µL/mL **(f)** 50 µL/mL

Figure 4.6: High resolution SEM images depicting self-assembled structures obtained from the oleic acid study at a dispersion volume of 60 µL and a magnetic field strength of 500 G (direction indicated by red arrow), for Sample 18 - 23 with parameters given in Table 4.4. Figure (a), (b), (c), (d), (e) and (f) shows the results obtained from self-assembly with an oleic acid concentration corresponding to 5, 10, 20, 30, 40 and 50 µL/mL, respectively.

outcome of the self-assembly process. Six experiments, with oleic acid batch concentrations of 5, 10, 20, 30, 40 and 50 μL/mL, were performed in which the total dispersion volume and magnetic field strength were held fixed at 60 μL and 500 G, respectively. The nanoparticle batch concentration was lowered from 2 mg/mL to 1.5 mg/mL in the attempt to obtain larger spacing between the lines. Parameters used for the six samples, Sample 18 - 23, of the oleic acid study are summarized in Table 4.4, and high resolution SEM images of the obtained self-assembled structures are shown in Figure 4.6.

Figure 4.6a shows how the self-assembled particles at a low oleic acid concentration of 5 μL/mL are more or less scattered randomly over the substrate. However, evidence of magnetic field induced self-assembly can be seen as short lines of particles appear at several locations on the sample. As this sample was not cleaned with ethanol prior to characterization, regions of oleic acid can be observed as dark spots surrounding the particles. When the concentration was raised to 10 μL/mL, the particles seem to more clustered together into worm-like structures with average length and width close to 10 and 1.5 μm, respectively. This can be seen in Figure 4.6b, and the inset in this figure reveals that a polycrystalline layer-by-layer stacking comprises the surface morphology, with what seems to be a [110] nanoparticle orientation. As in the case of 5 μL/mL, this sample was not cleaned prior to characterization, and dark spots of oleic acid surrounding the lines appear more pronounced. By further increasing the oleic acid concentration to 20 μL/mL, narrow lines with an average width of 5 nanocubes were forming as observed in Figure 4.6c, and the inset reveals that these lines are bilayers oriented in a [100]-manner with respect to the magnetic field. When it comes to 30 μL/mL in Figure 4.6d, the lines become wider than for 20 μL/mL and seem to stick more to each other than in the case of 20 μL/mL. The width of these individual lines is on average close to 300 nm. As can be seen in the inset, the lines become thicker as well, with at least four layers stacked well on top of each other. Furthermore the orientation of the nanocubes seems to be along the [110]-direction in terms of the surface layer, but the layer underneath seems to show more of a [100]-character. Figure 4.6e shows that an oleic acid concentration of 40 μL/mL causes even wider lines, merged into each other. At closer inspection, excellent long range order in a [100]-manner exists within the lines, as seen in the inset. Apparent cracks in the lines were most likely to form during cleaning, and show that the coherent stacking of several layers is generally very good. As the oleic acid concentration is increased to 50 μL/mL, depicted in Figure 4.6f, the lines become even wider and thicker, as can also be seen in the inset, but seem to still maintain a good coherent stacking of layers in the same manner as for 40 μL/mL. A slight film movement was observed upon acetonitrile injection for Sample 22 and 23, depicted in Figure 4.6e and 4.6f.

Table 4.4: The parameters and observed structures with nanocube (NC) orientation and width (W) (if relevant) of the oleic acid study at a constant total solvent amount of 60 µL and a magnetic field strength of 500 G. Nanoparticle batch concentration, oleic acid (OA) batch concentration, volumetric amount taken from the batch, volumetric amount pure hexane added to the dispersion, the total volume of the dispersion and the observed structure, are reported for Sample 18 - 23.

Sample #	Batch conc. [mg/mL]	OA conc. [µL/mL]	Batch amt. [µL]	Amt. added solv. [µL]	Total amt. [µL]	Observed structure
18*	1.5	5	20	40	60	Scattered NCs; monolayer
19*	1.5	10	20	40	60	Worm-like; multilayer; W: 1.5 µm
20	1.5	20	20	40	60	Lines; bilayer; [100]; W: 5 NCs
21	1.5	30	20	40	60	Lines; multilayer; [110]; W: 300 nm
22†	1.5	40	20	40	60	Merged Lines; multilayer; [100]
23†	1.5	50	20	40	60	Merged lines; multilayer; [100]

*Sample not cleaned prior to SEM characterization.

†Slight film movement observed upon acetonitrile injection.

Table 4.5: Self-assembly parameters and observed structures with nanocube (NC) orientation and width (W) for the line formation optimization. Strength of the magnetic field, nanoparticle batch concentration, volumetric amount taken from the batch, volumetric amount pure hexane added to the dispersion, the total volume of the dispersion and the observed structure, are reported for Sample 24 and 25.

Sample #	Field [G]	Batch conc. [mg/mL]	Batch amt. [µL]	Amt. added solv. [µL]	Total amt. [µL]	Observed structure
24*	500	3	20	40	60	Dense lines; monolayer; [100]; W: 5 NCs
25	500	3	10	50	60	Lines; monolayer; [100]; W: 4 NCs

*Film movement observed upon acetonitrile injection.

4.1.5 Further line optimization

To further optimize the self-assembled structure, the aim was to separate the lines to such an extent that the magnetic coupling between them is negligible. Two samples were made for this purpose, in which the nanoparticle concentration of the batch was increased to 3 mg/mL, and the oleic acid batch concentration set to 25 μL/mL. Sample 24 was self-assembled by taking out 20 μL from the batch whereas Sample 25 was self-assembled by taking out a volume of 10 μL, followed by dilution with hexane to a total volume of 60 μL, as summarized in Table 4.5. Note that in the case of Sample 25, the amount of oleic acid constituting the self-assembled film is reduced to half of the value corresponding to Sample 24, together with the number of nanocubes. The effective nanoparticle and oleic acid batch concentrations in the case of Sample 25 would therefore be equal to 1.5 mg/mL and 12.5 μL/mL, respectively, as compared to Sample 24.

In Figure 4.7, high resolution SEM images depicting the self-assembled superstructures in Sample 24 and 25, are shown. Upon injection of acetonitrile prior to lift-off, movement of the film was observed for Sample 24. Figure 4.7a shows a low magnification overview of the lines obtained in Sample 24, as they appear after self-assembly. Some of the lines appear thicker and wider than others, which after inspection turned out to be bundles consisting of thinner lines squeezed together, possibly during acetonitrile injection. A higher magnification image of Sample 24, depicting how the nanocubes are situated in the lines, is shown in Figure 4.7b. Also in this image, the lines seem distorted to some degree, possibly due to film compression. However, the width of the lines seems consistently within the sample to be $4 - 6$ nanocubes and the orientation is of the [100]-type. An overview image of Sample 25, self-assembled with a batch amount of 10 μL, is shown in Figure 4.7c, showing lines rather uniformly distributed over the substrate exhibiting a [100]-configuration, an average distance between lines of around 3 μm and with minimal bundle formation. The width of the lines seems uniform, which can from Figure 4.7d, depicting a single representative line at higher magnification, be determined to be on average 4 cubes.

4.1.6 Self-assembly in gradient magnetic fields

Studies were performed in which a gradient magnetic field was utilized in self-assembly. Due to the fact that a gradient field by definition changes its value with position, vertical fields in which the field would be uniform across the surface of the liquid film and gradients resulting in a field strength decrease with respect to increasing height, were taken into consideration to investigate self-assembled structures. A potential different mechanism associated with gradient field induced self-assembly suggests that optimal parameters obtained previously for horizontal lines can no longer be used. Nanoparticle batch concentrations up to 9 mg/mL and a consistent smaller oleic acid concentration of 3 μL/mL were used in the following

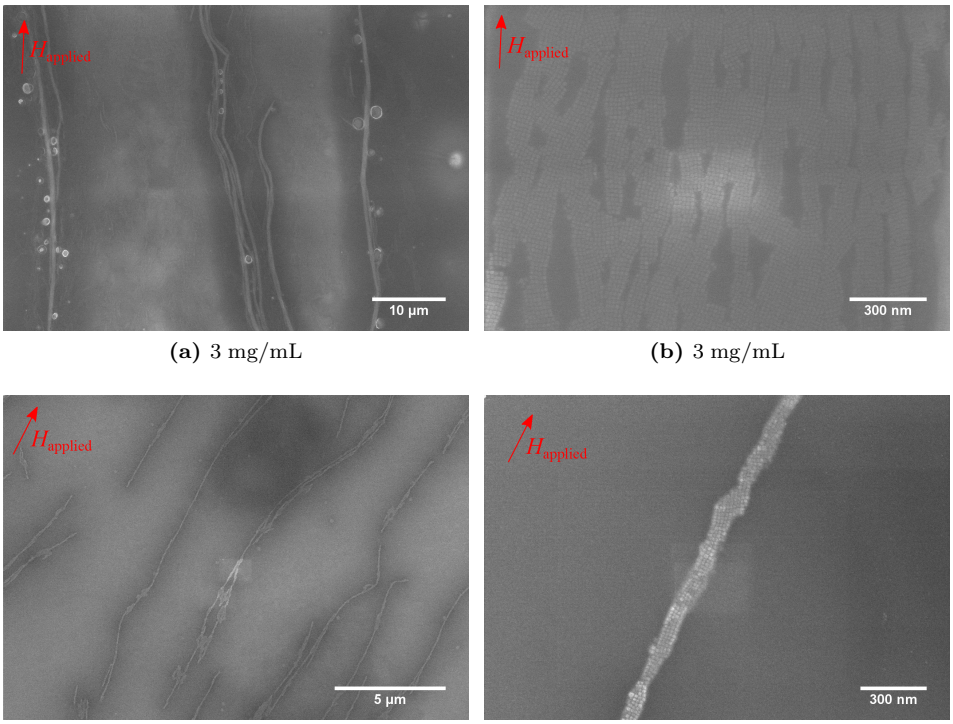

(a) 3 mg/mL **(b)** 3 mg/mL

(c) 1.5 mg/mL **(d)** 1.5 mg/mL

Figure 4.7: High resolution SEM images depicting two self-assembled structures from the line optimization, at dispersion volume and field corresponding to 60 µL and 500 G (direction indicated by red arrow), respectively. Self-assembly parameters of the two samples, Sample 24 and 25, can be found in Table 4.5. Figure (a) and (b) show an overview image and an image captured with a higher magnification, respectively, for Sample 24 at a nanoparticle batch concentration of 3 mg/mL. Figure (c) and (d) show an overview image and an image captured with a higher magnification, respectively, for Sample 25 at an effective concentration of 1.5 mg/mL.

experiments. Unless stated otherwise, a dispersion volume of 40 µL was taken out directly from the batch without any further dilution. Self-assembly experiments were performed in which the effects of magnetic field, gradient, nanoparticle concentration and volume were investigated.

For convenience, parameters for the following samples are reported in Table 4.6 at the end of this subsection, together with the obtained structure and associated mean cross section size, height and aspect ratio. The mean cross section size

was calculated on the basis of 50[1] measurements and the height was calculated considering 100 measurements. Resulting mean cross section size, height and aspect ratio, with associated standard deviations, for relevant samples are also displayed as bar charts in Figure 4.11 at the end of this subsection, for easier comparison.

Gradient magnetic field study

As an initial study, the significance of the magnetic field gradient was investigated for the six samples labeled Sample 26 - 31 in Table 4.6, with a nanoparticle batch concentration of 9 mg/mL. Figure 4.8a shows high resolution SEM images of the self-assembled structures of Sample 26, obtained at a uniform vertical field of 1500 G. The main image is taken in top-view and the inset is a cross-sectional SEM image. Dense rod-like superstructures seem to appear at these conditions, with a rather irregular cross-sectional shape. The mean cross section size and height of the rods were measured to be 123 nm and 198 nm, respectively, resulting in an aspect ratio of 1.6. As the field is set to vary with height, resulting in a gradient equal to 100 G/cm, similar structures to the previous sample appear, as can be seen in Figure 4.8b. In this case, the mean cross section size, height and aspect ratio were measured to be 144 nm, 112 nm and 0.77, respectively, indicating that these structures were more cylinder-like than rods and on average shorter and thicker. In addition, the cylinders grew less densely than the previous sample. As the gradient is further increased to 200 G/cm, like in the case of Sample 28, higher and thinner rod-like structures were obtained, as depicted in Figure 4.8c. The inset on the left hand side of this figure shows a higher magnification micrograph, and the right hand side inset shows a cross-sectional image. Mean cross section size, height and associated aspect ratio were measured to be 124 nm, 216 nm and 1.7, respectively. A gradient of 300 G/cm, being the strongest gradient considered in this study, resulted in the highest rods obtained so far, as depicted in Figure 4.8d for Sample 29. With a mean cross section size, height and aspect ratio corresponding to 141 nm, 229 nm and 1.6, respectively, the rods also grew less denser than in the previous samples of this gradient study, but still exhibited a rather similar cross-sectional morphology.

In addition to the varying gradient study, two experiments were performed in which the gradient was held fixed at 200 G/cm and the magnetic field strength at the liquid film level was changed. Sample 30 was self-assembled with a magnetic field strength of 100 G and Sample 31 with 400 G. As for Sample 30, the weak field resulted in self-assembled nanocubes onto multilayered pads with various sizes and shapes, as depicted in Figure 4.8e. Due to the high concentration of nanoparticles, island can be seen to grow on top of the pads as well. Because of the lack of one-dimensionality in the obtained structures of Sample 30, mean cross section

[1]Obtaining good cross-sectional SEM images of self-assembled structures has been proven difficult due to a necessary scribing step which tend to destroy proximal structures. Hence only 50 rods were taken into consideration.

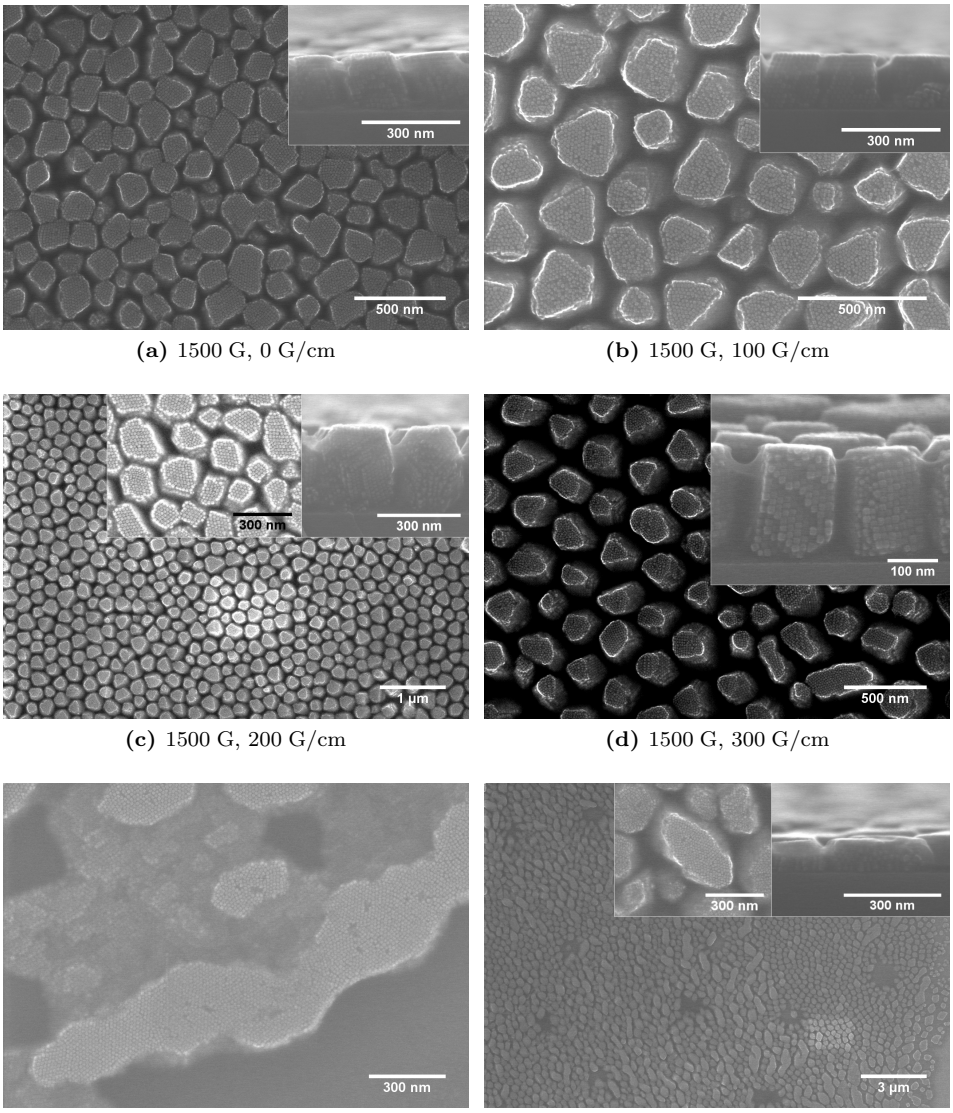

(a) 1500 G, 0 G/cm **(b)** 1500 G, 100 G/cm

(c) 1500 G, 200 G/cm **(d)** 1500 G, 300 G/cm

(e) 100 G, 200 G/cm **(f)** 400 G, 200 G/cm

Figure 4.8: High resolution SEM images depicting self-assembled structures obtained from the gradient magnetic field study at a dispersion volume of 40 µL and a batch nanoparticle concentration of 9 mg/mL, for Sample 26 - 31 with parameters given in Table 4.6. Figure (a) shows structures obtained in a uniform vertical field of 1500 G, (b) 1500 G with gradient 100 G/cm, (c) 1500 G with gradient 200 G/cm, (d) 1500 G with gradient 300 G/cm, (e) 100 G with gradient 200 G/cm and (f) 400 G with gradient 200 G/cm. Main images were captured in top-view and insets (right inset in case of two) were captured in cross-sectional view.

size, height and aspect ratio were not measured and are thus not reported in Table 4.6. Sample 30 is therefore also not included in the bar charts of Figure 4.11. In the case of Sample 31, 400 G seems to yield more separated one-dimensional-like structures, as depicted in Figure 4.8f. At closer inspection, the right hand side inset reveals that the obtained structures are more disc-like than rod-like. The left hand side inset shows a higher magnification micrograph of the cross sections of the discs, revealing together with the main image a rather irregular morphology. Mean cross section size, height and associated aspect ratio were measured to be 193 nm, 77 nm and 0.40, respectively.

Nanoparticle concentration study

From the magnetic field gradient study reported above, it seems like the stronger the gradient, the more uniform cross section size, height and morphology could be obtained. A strong field at the liquid level seems also to yield higher aspect ratio structures. Knowing this, a concentration study was performed to investigate whether tuning rod cross section size and height by varying the concentration could be achieved. Three experiments were performed at concentrations 3, 5 and 5 mg/mL, in which the vertical magnetic field was held fixed at 1200 G and the field gradient held fixed at 300 nm. High resolution SEM images for the three samples, Sample 32 - 34, are shown in Figure 4.9.

Figure 4.9a and 4.9b show a top-view and a cross-sectional SEM image, respectively, of the self-assembled structures obtained from Sample 32 at 3 mg/mL. A slight film movement was observed for this sample upon acetonitrile injection. As for Figure 4.9a, the cylindrical structures appear more or less merged into each other. The inset, showing a 40° tiled view, reveals discs of approximately $6 - 7$ cubes stacked coherently on top of each other, which also is confirmed in Figure 4.9b. Mean cross section size, height and aspect ratio for the discs were measured to be 128 nm, 89 nm and 0.70, respectively. As the concentration was increased to 5 mg/mL, densely packed short thin filaments with a mean cross section, height corresponding to 90 nm, 127 nm and 1.4, respectively, were obtained. The filaments, shown in top-view in Figure 4.9c and cross-sectional view in Figure 4.9d, exhibit a rather regular cross section and clearly bear the imprint of the cubic constituents, as seen in the inset of Figure 4.9c. It should be noted that for this particular sample the filaments did not cover it uniformly, but rather concentrated in islands with size in the range $5 - 10$ µm. Further increase of the concentration to 9 mg/mL resulted in rod formation, as seen from the top-view and cross-sectional SEM images displayed in Figure 4.9e and 4.9f, respectively. Figure 4.9e shows rather uniformly spaced rods and the inset reveals a circular-like cross section where the nanocubes seem to have grown around the lengthwise axis of the rods. The sample was in this case uniformly covered with rods. Figure 4.9f depicts the rods, more or less covered in oleic acid, with an inset showing a top-view image of rods that has been falling over and thus lying horizontally on the substrate. The mean cross section size and height were for the rods measured

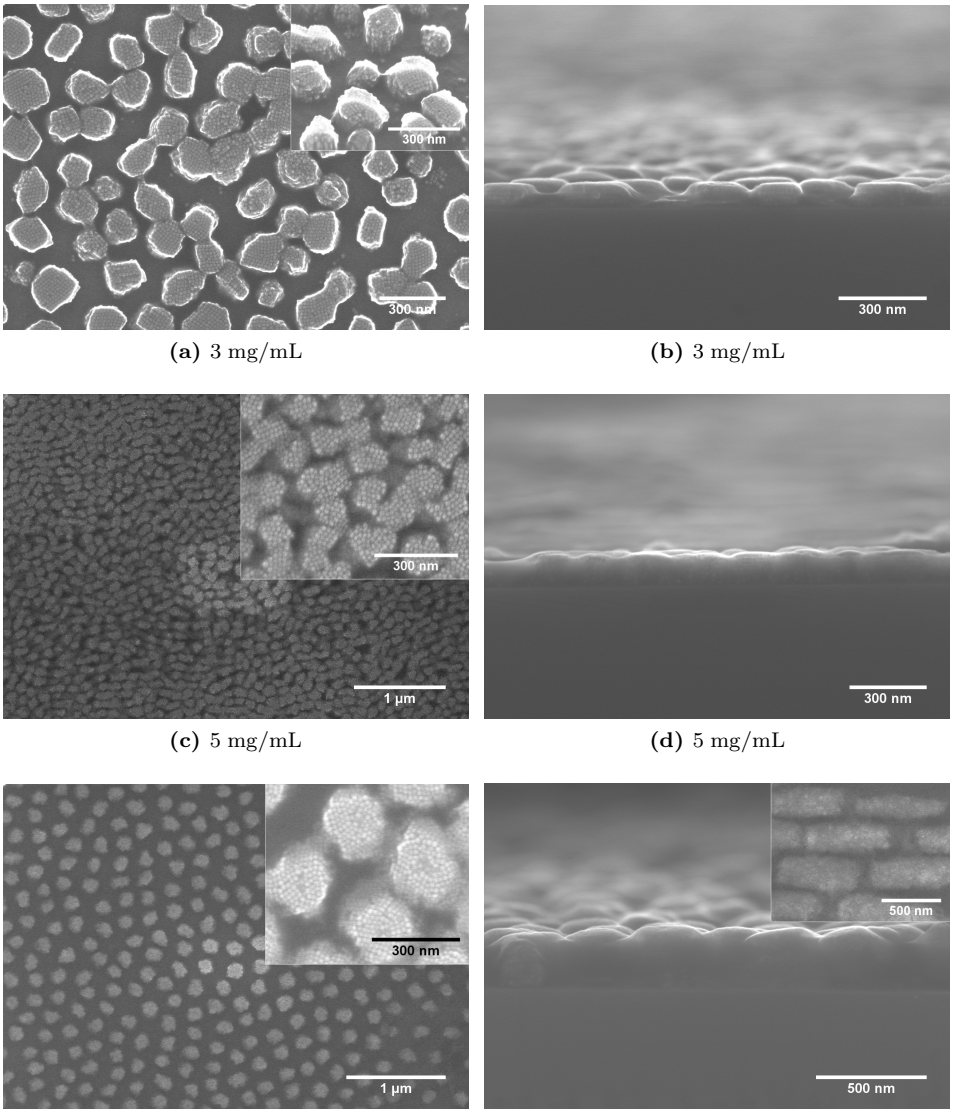

(a) 3 mg/mL **(b)** 3 mg/mL

(c) 5 mg/mL **(d)** 5 mg/mL

(e) 9 mg/mL **(f)** 9 mg/mL

Figure 4.9: High resolution SEM images depicting self-assembled structures obtained from the nanoparticle concentration study at a dispersion volume of 40 µL, for Sample 32 - 34 with parameters given in Table 4.6. The magnetic field and gradient in this study were held fixed at 1200 G and 300 G/cm, respectively. Figure (a) and (b) show the results obtained from self-assembly with a nanoparticle concentration of 3 mg/mL, (c) and (d) 5 mg/mL, and (e) and (f) 9 mg/mL. Figure (a), (c) and (e) were captured in top-view whereas (b), (d) and (f) are cross-sectional images.

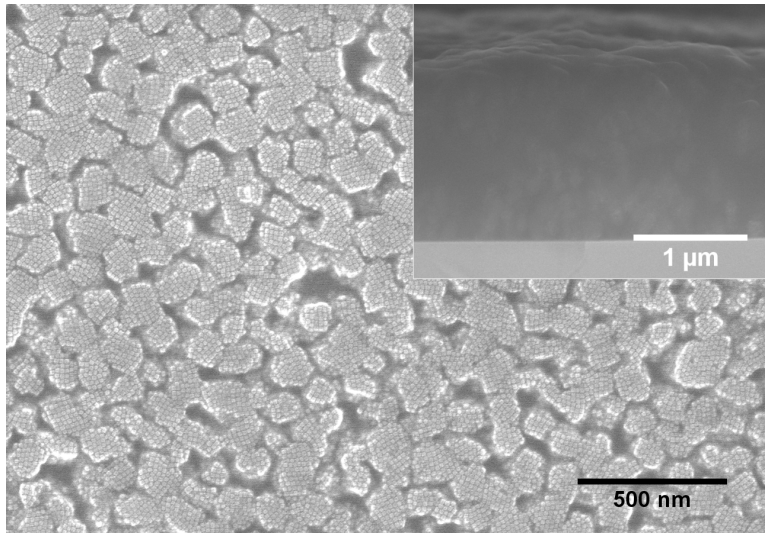

Figure 4.10: High resolution SEM images depicting self-assembled structures obtained from the volume study at a dispersion volume of 100 µL and a batch oleic acid concentration of 3 µL/mL, for Sample 35 with parameters given in Table 4.6. The magnetic field and gradient of experiment were held fixed at 1200 G and 300 G/cm, respectively.

to be 191 nm and 410 nm, respectively, with a mean aspect ratio of 2.1.

Volume study

In order to understand the effect of the dispersion volume, one final experiment was performed with 100 µL dispersion volume instead of the usual 40 µL, in which the the concentration was chosen to be 9 mg/mL and all other variables identical to the concentration study above. SEM images showing the obtained structures from Sample 35 are displayed in Figure 4.10. A volume of 100 µL seems to yield densely packed filaments with cross-sectional morphology very similar to to Sample 33 in Figure 4.9c. However, in this case the filaments covered the substrate uniformly. The inset, captured with cross-sectional SEM, reveals that these filaments are much longer than previous obtained structure lengths, and that they seem to be growing in a more curly manner. The mean cross section size and height were measured to be 87 nm and 1182 nm, respectively, resulting in a mean aspect ratio of 13.6.

Table 4.6: The parameters and observed structures, with associated mean cross section size (CS), height (H) and aspect ratio (AR), of the gradient magnetic field study at different magnetic fields, gradients, nanoparticle batch concentrations and volumes. Strength of the magnetic field and field gradient at surface of the liquid film, nanoparticle batch concentration, volumetric amount taken from the batch, oleic acid batch concentration and the observed structure, are reported for Sample 26 - 35.

Sample #	Field [G]	Gradient [G/cm]	Batch conc. [mg/mL]	Batch amt. [μL]	OA conc. [μL/mL]	Observed structure
26	1500	0	9	40	3	Rods; CS: 123 nm; H: 196 nm; AR: 1.6
27	1500	100	9	40	3	Cylinder-like; CS: 144 nm; H: 112 nm; AR: 0.77
28	1500	200	9	40	3	Rods; CS: 124 nm; H: 216 nm; AR: 1.7
29	1500	300	9	40	3	Rods; CS: 141 nm; H: 229 nm; AR: 1.6
30	100	200	9	40	3	Pads
31	400	200	9	40	3	Disc-like; CS: 193 nm; H: 77 nm; AR: 0.40
32*	1200	300	3	40	3	Discs; CS: 128 nm; H: 89 nm; AR: 0.70
33	1200	300	5	40	3	Dense filaments; CS: 90 nm; H: 127 nm; AR: 1.4
34	1200	300	9	40	3	Rods; CS: 191 nm; H: 410 nm; AR: 2.1
35	1200	300	9	100	3	Dense filaments; CS: 87 nm; H: 1182 nm; AR: 13.6

*Film movement observed upon acetonitrile injection.

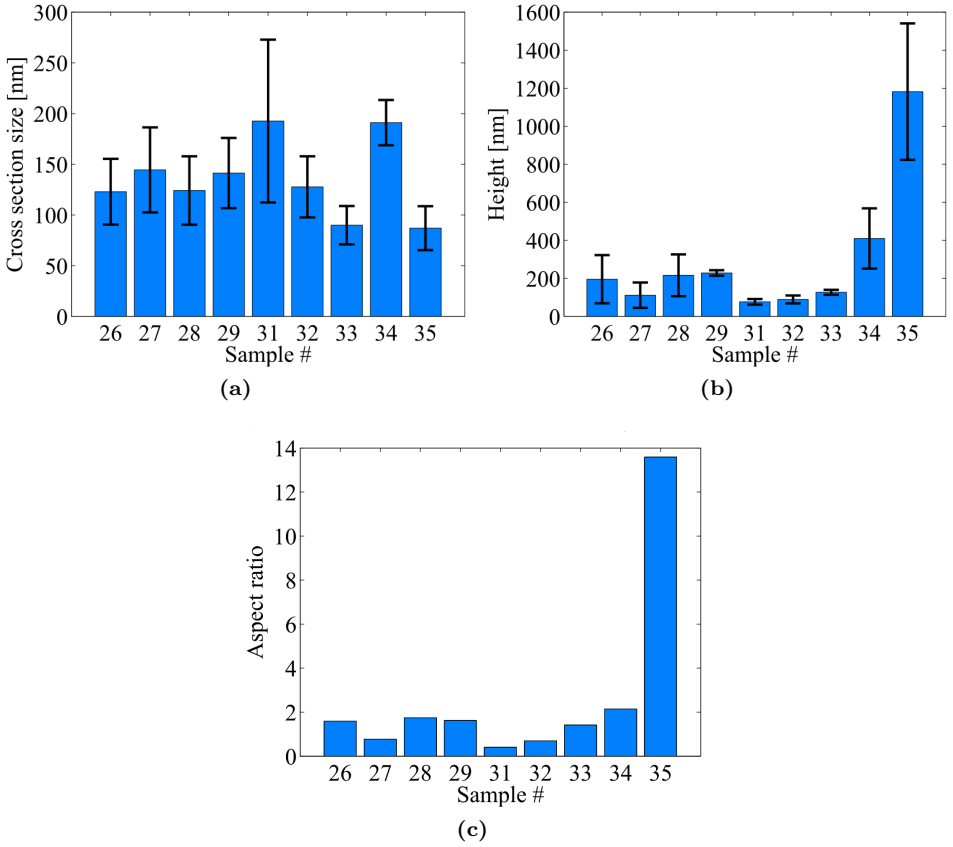

Figure 4.11: Bar charts showing measured cross section sizes in (a) and heights in (b), with associated standard deviations, for the obtained structures from samples reported in Table 4.6. 100 cross section sizes and 50 heights were measured for each sample. Height-cross section aspect ratios based on mean values are also reported in (c). Sample 30 is not reported.

Summary

What can be said in general about the results obtained from the measurements of structure dimensions reported in Figure 4.11, is that stronger fields seem to give a higher degree of one-dimensionality, in terms of aspect ratio, than weaker fields. The same statement does not necessarily seem to hold true for stronger and weaker gradients. It can be noted, however, that stronger gradients tend to give smaller standard deviations in the respective dimensional distributions of the obtained structures. No clear trend can be seen for the separate cross section sizes in Figure 4.11a and heights in Figure 4.11b, in terms of the applied magnetic field

and gradient. The applied field needs nevertheless to be strong enough in order to obtain structures with an acceptable one-dimensionality, that is, at least stronger than 100 G. Furthermore, increasing nanoparticle concentration seems to yield a correlated increase in both the structure height and aspect ratio, something which also holds true for increasing dispersion volumes. However there seems to be no correlation between the concentration or volume and the measured mean cross section size.

4.2 Monte Carlo simulations

Interesting results were obtained in the previous section as a result of a very complicated process of physical interactions that may change with the time elapse of the process. Monte Carlo simulations were performed to gain physical insight to the mechanism of self-assembly for both line and rod formation.

Simulating processes like magnetic field induced self-assembly poses certain challenges when it comes to choosing parameters that make the simulation as physical as possible, and at the same time keeping it computationally viable. Unless stated otherwise, parameters with associated symbols and values used in the simulations which are not related to any potentials (see Table 3.2 in Section 3.2.1) are summarized in Table 4.7. The number of steps was chosen to be 100000, 20 nanocubes were considered and the solvent volume set to a cube with size 150 nm. The oleic acid concentration was set to 200 μL/mL, approximately an order of magnitude higher than in the experiments, by assuming that some of solvent has already evaporated to reach this point and that nothing significant happens to the system in terms of self-assembled structures when the oleic acid concentration is lower than 200 μL/mL. The initial concentration of nanocubes would correspond to approximately 5 mg/mL, slightly higher than the one used in most uniform field experiments. The volume is, however, substantially smaller in the simulation which makes it possible to investigate monolayer formation with a smaller number of cubes than under experimental conditions. Furthermore, the step time was set to 5 ns which corresponds to a mean step size of 0.2 nm in a haxane solution with 200 μL/mL oleic acid. The choice of the step time would be a measure on the accuracy through the resulting step size, and 5 ns was considered to be acceptable in the context of 12 nm cubes. By adding step times for each iteration, the parameters reported in Table 4.7 would result in a total self-assembly process time of about 20 ms.

In order to speed up the evaporation process, the evaporating rate was set to 10^7 nm per simulated second, or 10^{-2} nm/ns, five orders of magnitude larger than the actual one reported in Section 3.1 to be 30 nm/s. The motivation for this crude increase is that the simulated time of 20 ms would merely correspond to a height reduction of the liquid film of 0.6 nm, assuming experimental conditions. Moreover, the evaporation rate needed to be high enough to allow all the hexane

to evaporate during the course of 1000000 steps (more steps would just result in an unacceptable long computation time), and at the same time low enough to allow the particle to diffuse from the liquid-air interface to prevent aggregation. The parameters k_e and ξ, associated with the evaporation time step function (see Equation 3.2 in Section 3.2.2), were set to 20 and 0.41, respectively, to ensure that exactly 100 % of the hexane evaporates during the time elapse of the simulation.

4.2.1 Self-assembly in the absence of a magnetic field

As an initial test, a simulation was performed with nanocubes in the absence of a magnetic field. Snapshots of the process are displayed in Figure 4.12 after the number of steps, n, corresponding to 0, 100000, 500000, 800000, 900000 and finally 1000000. In the beginning of the process, the nanocubes are randomly dispersed in the volume as expected. After $n = 100000$ steps of the simulation, most of the solvent has already evaporated and the particles are approaching each other. As the iterations progress from $n = 500000$ to 900000, the cubes self-assemble in increasingly ordered patterns, as can be seen in the figure in top-view. Finally after $n = 1000000$ steps, the cubes have organized themselves in an ordered pattern, seemingly with magnetic moments head-to-tail in a square configuration. Side-view reveals an alternating positive and negative perpendicular component. An SEM image depicting the self-assembled structure obtained in the absence of a magnetic field, shows grains with the same ordering and approximately equal size as the obtained simulated structure.

4.2.2 Uniform horizontal magnetic fields

When a uniform magnetic field is applied, the simulated self-assembly mechanism seems to be rather different than in the absence of a field, as can be seen from the snapshots in Figure 4.13, in the case of 500 G. After 100000 steps, the

Table 4.7: Parameters with their associated symbols and values, used in the Monte Carlo simulations.

Parameter	Symbol	Value
# of steps	n	10^6
# of particles	N	20
Step time	τ	$5 \cdot 10^{-9}$ s
Solvent volume	V_{solvent}	150^3 nm^3
OA conc.	c_{oa}	200 μL/mL
Evaporation rate	v_{evap}	10^7 nm/s
Step funct. const.	k_e	20
Step funct. shifting	ξ	0.41

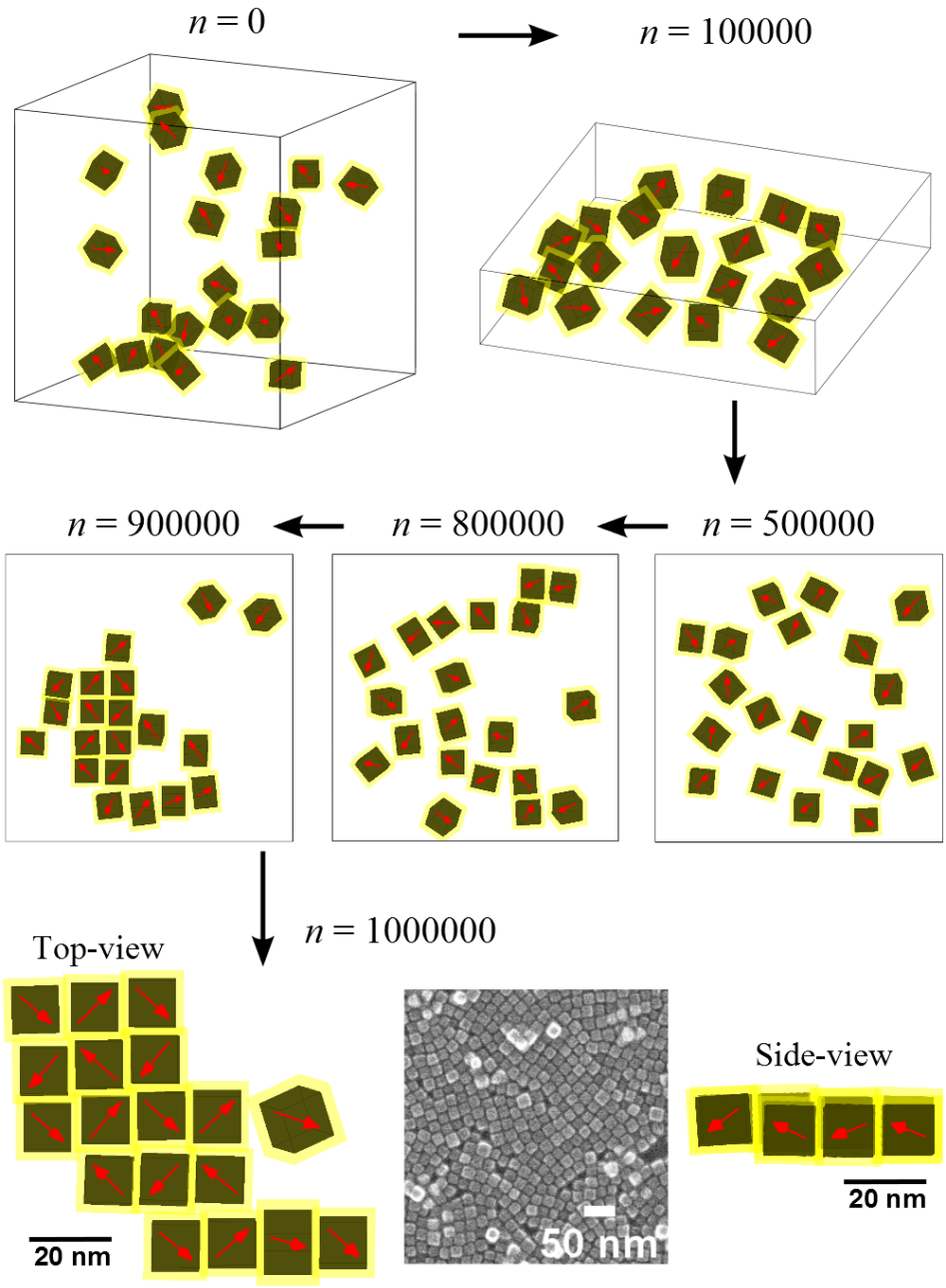

Figure 4.12: Snapshots from the Monte Carlo simulation of nanocubes in the absence of a magnetic field. Snapshots after n equal to 0, 100000, 500000, 800000, 900000 and 1000000 steps are shown, together with an SEM image of an obtained structure from the equivalent experiment.

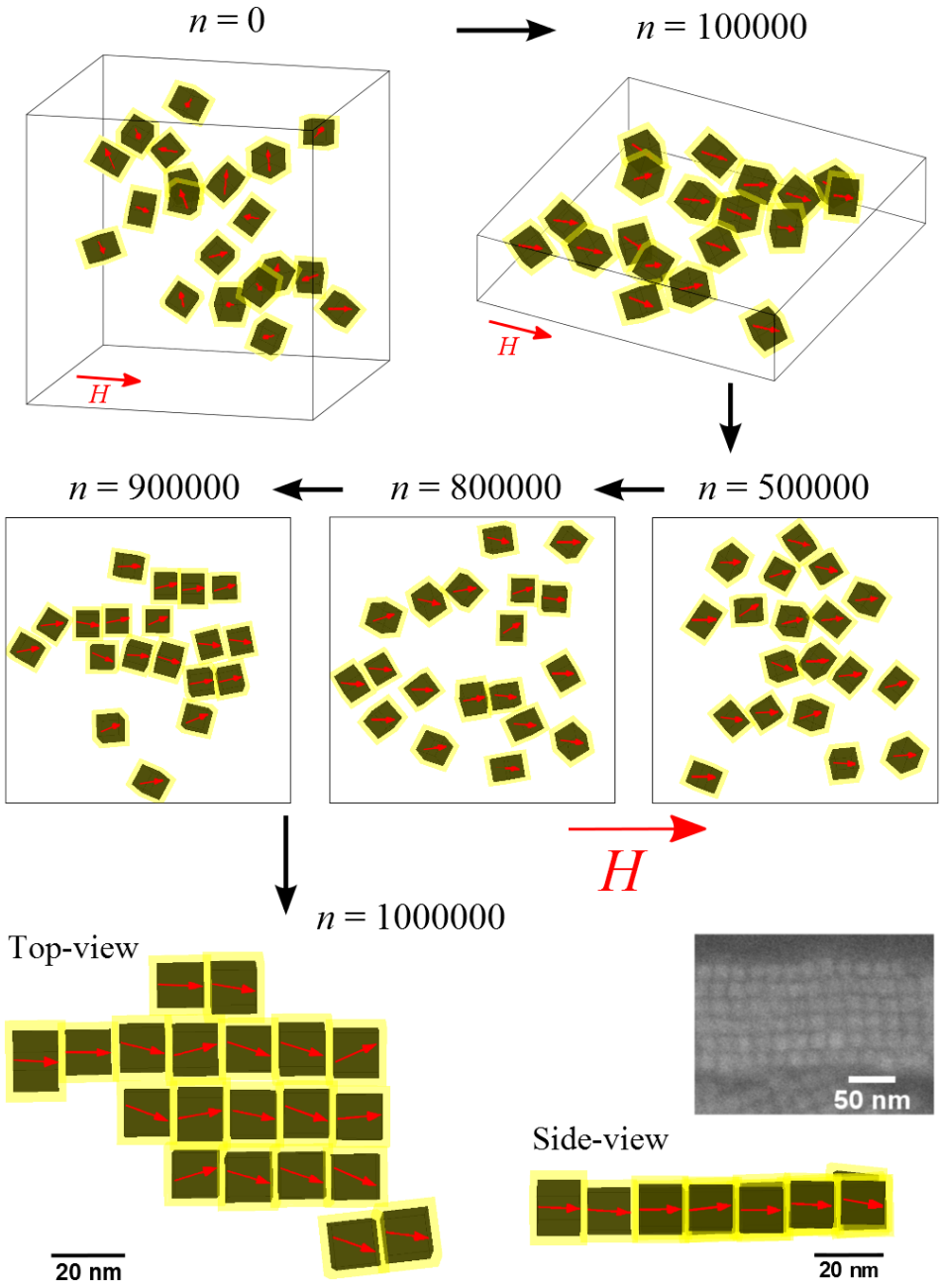

Figure 4.13: Snapshots from the Monte Carlo simulation of nanocubes in an applied uniform horizontal magnetic field H, of 500 G. Snapshots after n equal to 0, 100000, 500000, 800000, 900000 and 1000000 steps are shown, together with an SEM image of an obtained structure from the equivalent experiment.

snapshots show how the magnetic moment are aligning in the direction of the applied magnetic field, as opposed to the previous simulation shown in Figure 4.12. As the iterations progress from $n = 500000$ to 900000, the cubes self-assemble in increasingly ordered line-like patterns with moments still more or less aligned in the field direction, as seen in top-view in the figure. After $n = 1000000$ steps, the cubes have self-assembled in lines aligned along the [100]-direction. This result is consistent with experimental results obtained at the same applied magnetic field, as seen in the SEM image in the lower right of the figure. In the top-view image, the magnetic moments seem to be situated in a zigzag pattern, with most of the moments exhibiting head-to-tail configuration. The side-view image reveals that the perpendicular components of the magnetic moments are close to zero. Mean angular deviation of the moments from the field direction was calculated to be 15.3 °, with a standard deviation of 5.6 °.

Figure 4.14 shows snapshots from a simulation similar to the one above, but performed in a magnetic field corresponding to 2000 G. It can be observed that after $n = 100000$ steps, the moments are to a greater extent aligned in the direction of the field, as can be expected according to theory. The top-view snapshots corresponding to $n = 500000$, 800000 and 900000 steps show, similar to the case of 500 G, that the cubes are self-assembling in a line-like fashion. However, the majority of cubes seem to be aligned along the field in the [110]-direction as the simulation reaches 900000 steps. This is indeed the case after $n = 1000000$ steps, as a line consisting of cubes aligned in the [110]-direction can be seen in the top-view snapshot. This configuration is also consistent with experimental results obtained at 2000 G, as seen in the SEM images in the lower right of the figure. Magnetic moments associated with the nanocubes also seem to be well aligned in the direction of the field, both in the top-view and in the side-view. The calculated mean angular deviation of the magnetic moments from the direction of the field was found to be 4.0 °, with a standard deviation of 2.5 °.

So far, simulation results are consistent with experimentally obtained structures in the field study, as summarized in Figure 4.4. In the attempt to find the magnetic field strength at which the morphology of the lines makes a transition from [100]- to [110]-orientation, four additional simulations were performed at identical conditions as above, except for the magnetic field strength which was set to 250 G, 750 G, 1000 G and 1500 G. Due to similar obtained mechanisms as with 500 G and 2000 G, only the end results are considered, as shown in top-view in Figure 4.15. For 250 G shown in Figure 4.15a, the magnetic moments adopt the same zigzag pattern obtained in the case of 500 G and the lines exhibit [100]-morphology. The mean deviation from the direction of the field was in this case found to be 27.7 °, with a standard deviation of 4.6 °. Interestingly at 750 G in Figure 4.15b, there seems to be line formation in both [100]- and [110]-orientation. Mean deviation from the direction of the field was in this case found to be, 6.2 °, with a standard deviation of 5.1 °. As the field strength is raised to 1000 G, Figure 4.15c shows that only the [110]-morphology is represented. The mean deviation from the direction of the field was calculated to be, 8.2 °, with a standard deviation

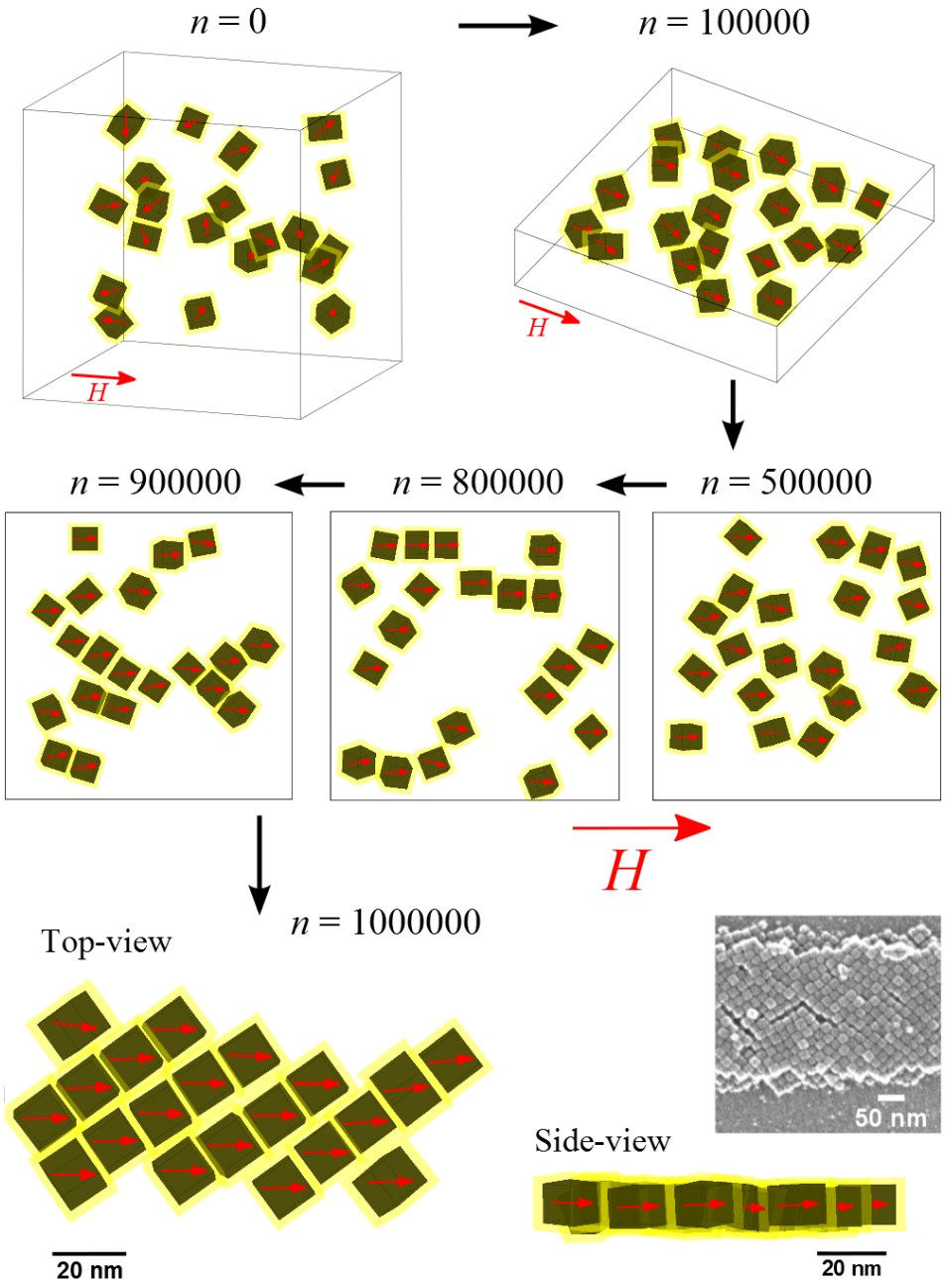

Figure 4.14: Snapshots from the Monte Carlo simulation of nanocubes in an applied uniform horizontal magnetic field H, of 2000 G. Snapshots after n equal to 0, 100000, 500000, 800000, 900000 and 1000000 steps are shown, together with an SEM image of an obtained structure from the equivalent experiment.

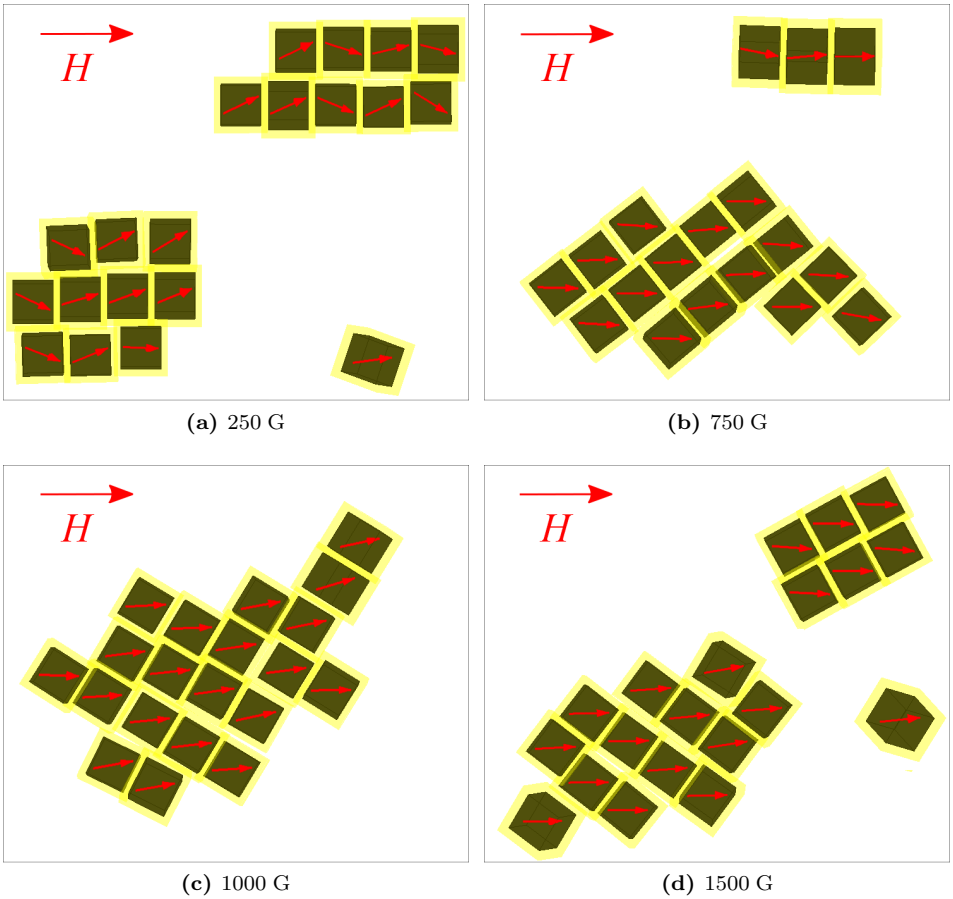

(a) 250 G **(b)** 750 G

(c) 1000 G **(d)** 1500 G

Figure 4.15: End result from the Monte Carlo simulations of nanocubes in an applied uniform horizontal magnetic field H. Figure (a), (b), (c) and (d) show the self-assembled structures obtained at a magnetic field of 250 G, 750 G, 1000 G and 1500 G, respectively.

of 3.9 °, thus a larger value than for 750 G. For 1500 G, the [110]-morphology is also obtained, as displayed in Figure 4.15d, with moments deviating from the direction of the field with an average angle of 5.1 ° and with a standard deviation of 4.4 °.

4.2.3 Vertical gradient magnetic fields

A simulation was performed with a vertical gradient magnetic field, in which the field strength at the bottom of the volume was set to 1200 G, and the gradient set to 1 G/nm (decreasing with increasing height), or 10^7 G/cm. This gradient is five orders of magnitude larger than the experimental value. All parameters in Table 4.7 were left unchanged, except for the number of particles N which was increased to 100, the z-dimension of the box which was increased to 600 nm, and k_e and ξ which were respectively set to 18.8 and 0.45. Snapshots of the simulation after $n = 0$, 100000, 600000, 900000 and 1000000 steps are shown in Figure 4.16. At $n = 0$, the particles are randomly dispersed throughout the volume, as should be the initial condition. After 100000 steps, most of the hexane has already evaporated, and the the magnetic moments of the particles are aligned in the vertical direction. As the steps progress from $n = 100000$ to 900000 the particles seem to approach each other more and more, concentrated towards the center of the volume, with moments still aligned in the vertical direction. Finally after 1000000 steps, the particles have self-assembled into a rod like structure with the [110]-direction facing upward in the direction of the applied field, together with the magnetic moments. This configuration is very similar to the results obtained experimentally with vertical gradient magnetic fields, as shown in the SEM image in the lower right of the figure.

4.3 FMR characterization

FMR spectroscopy was performed on three samples exhibiting three different types of magnonic structures, Sample 0 as the control, Sample 19 exhibiting lines of nanocubes and Sample 34 with rods. For Sample 0, the attenuation was set to 5 dB, corresponding to a microwave power of 63.25 mW, whereas in for Sample 19, an attenuation of 0 dB was used, corresponding to a maximum microwave power of 200.0 mW. For both samples, in-plane magnetic fields were employed, and the field was for every considered angle swept from 100 to 7100 G with the number of data point collected within one sweep corresponding to 3500. In the case of Sample 34, the attenuation was set to 15 dB, corresponding to a microwave power of 6.33 mW. The sample was positioned vertically in the cavity such that the rods were oriented in-plane to the applied magnetic field. At every angle, the field was swept from 250 to 5500 G with the number of data point collected within one sweep corresponding to 2000.

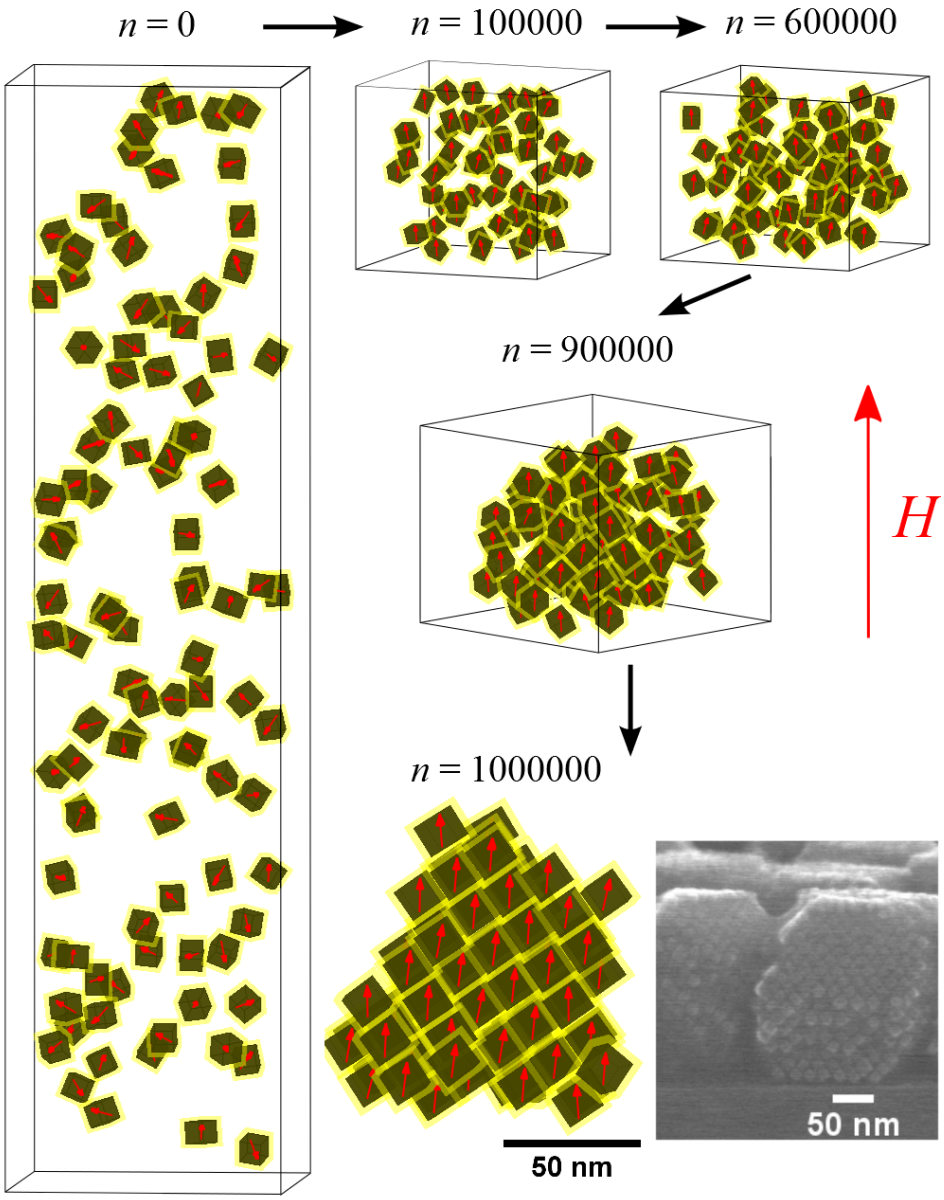

Figure 4.16: Snapshots from the Monte Carlo simulation of nanocubes in an applied vertical gradient magnetic field indicated by H. The value of the field at the bottom of the volume box was set to 1200 G, and the gradient was set to 1 G/nm (decreasing with increasing height), or 10^7 G/cm. Snapshots after n equal to 0, 100000, 600000, 900000 and 1000000 steps are shown, together with an SEM image of an obtained structure from the equivalent experiment.

4.3.1 Sample 0 - control

FMR spectroscopy was initially performed on the the control sample, that is, Sample 0, according to the method stated in Section 3.3. Self-assembly parameters for Sample 0 were given in Table 4.1. Results from the characterization of Sample 0 are shown in Figure 4.17. As stated in Section 2.4, the reported signal is the derivative of the actual peak, which corresponds to the bottom curve in Figure 2.10 from Section 2.10. The angular dependence of the signal, obtained from the magnetic field sweep, is illustrated as a surface plot in Figure 4.17a, in which the spectrum from the field sweep corresponding to each angle is shown by color coding the signal level according to the colorbar on the right hand side. This way, signal maxima in each spectrum appear read, and minima appear blue. The signal is reported as arbitrary units. In addition, an SEM image of the analysed structure of Sample 0, with the associated FFT, are given for comparison.

In Figure 4.17a, the uniform precession is indicated by the vertical red belt, occurring at a magnetic field strength of approximately 2400 G with an associated linewidth of 550 G. There seems to be one additional peak occurring at the angles 152 ° and 332 °, indicated by red arrows in the spectrum. Note that these two angles are separated by exactly 180 °. To further investigate the existence of second peaks in the spectrum, cross sections of angles corresponding to 62 °, 152 °, 242 ° and 332 °, were plotted in Figure 4.17b for comparison. Here it can be seen that there indeed exists a second peak at the angles 152 ° (red curve) and 332 ° (green curve), positioned at approximately 3900 G in both cases. Furthermore there seems to be no observable second peak at the angles in between.

4.3.2 Sample 19 - lines

As the control has been established, FMR spectroscopy was performed on Sample 19, exhibiting separated monolayered lines, with parameters given in Table 4.5. The resulting spectrum together with an SEM image of one of the lines is displayed in Figure 4.18a. A rather different behaviour is shown here, in which the uniform precession varies in a wave-like manner with respect to the angle of the applied magnetic field. The position of the uniform precession varies from 2500 to 3100 G with a linewidth varying between 400 and 900 G, in which higher field peak positions result in larger linewidths. Furthermore, there seems to be second peaks at the angles 62 ° and 242 °, as indicted by red arrows in the spectrum. In this case as well, there is exactly a difference of 180 ° between the angles at which second peaks occur.

As in the case of the control sample, cross sections corresponding to the angles at which second peaks were observed, that is, 62 ° and 242 °, were plotted in Figure 4.18b together with two angles in between, namely 152 ° and 332 °. It can be seen that there is a significant difference between the spectra at the angles 62 ° (blue curve) and 242 ° (black curve), and at the angles 152 ° (red curve) and 332 °

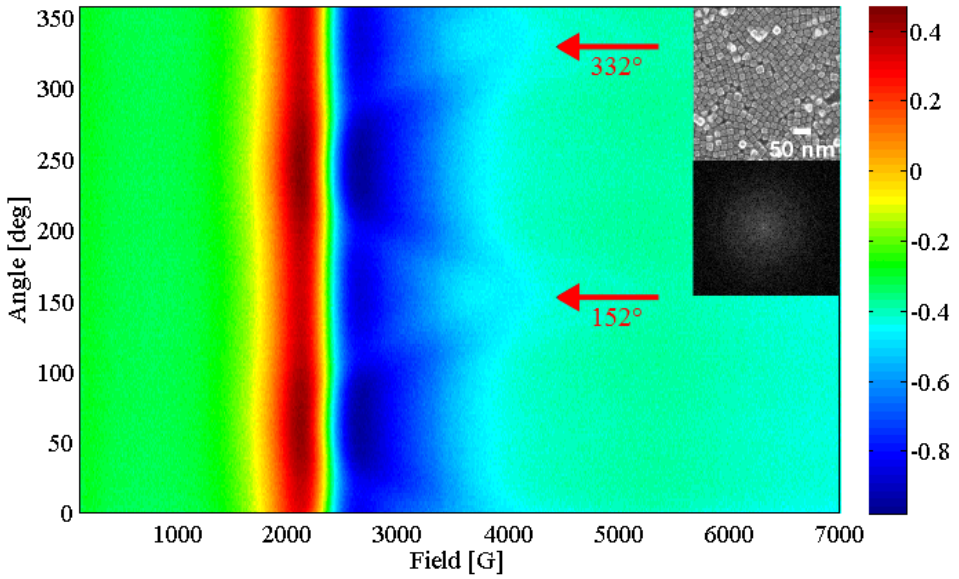

(a)

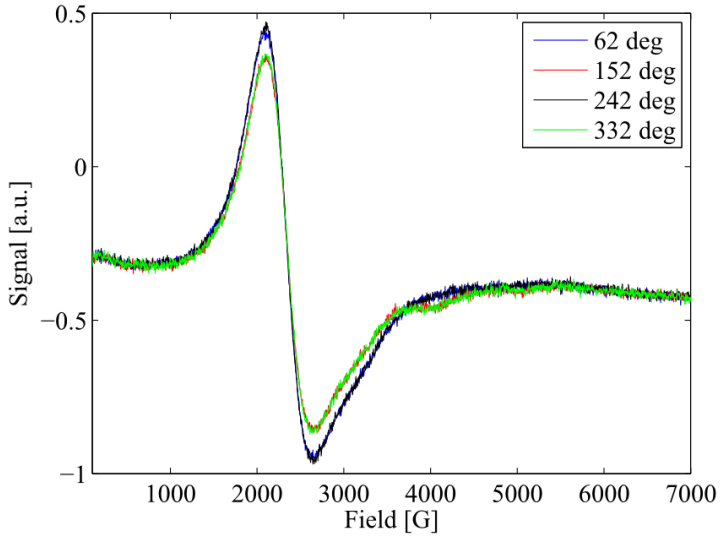

(b)

Figure 4.17: FMR spectroscopy results obtained for the control sample, that is, Sample 0, with parameters given in Table 4.1. Figure (a) shows a combination of the FMR spectra corresponding to each angle of the applied field. The signal is given as a color code corresponding to the colorbar with arbitrary units. Second peaks in the spectrum are indicated by red arrows, and an SEM image of Sample 0 with associated FFT are given. (b) shows the spectra corresponding to the angles 62 ° (blue curve), 152 ° (red curve), 242 ° (black curve) and 332 ° (green curve).

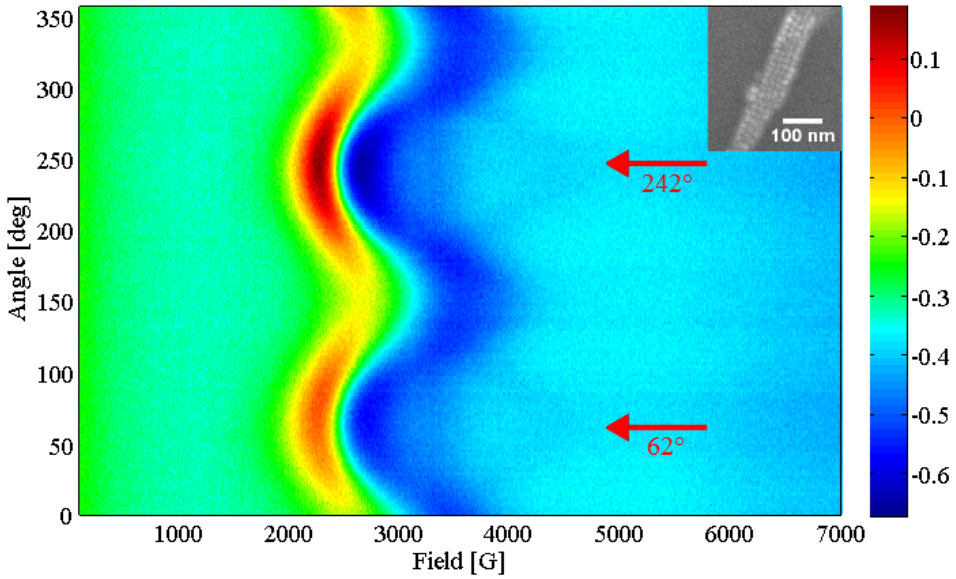

(a)

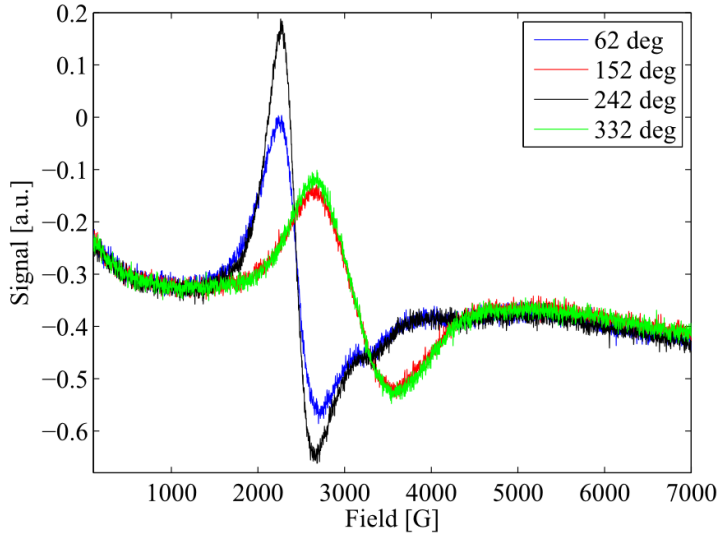

(b)

Figure 4.18: FMR spectroscopy results obtained for the lines in Sample 19, with parameters given in Table 4.5. Figure (a) shows a combination of the FMR spectra corresponding to each angle of the applied field. The signal is given as a color code corresponding to the colorbar with arbitrary units. Second peaks in the spectrum are indicated by red arrows, and an SEM image of Sample 19 is given. (b) shows the spectra corresponding to the angles 62 ° (blue curve), 152 ° (red curve), 242 ° (black curve) and 332 ° (green curve).

(green curve). A second peak can be observed in both of the spectra corresponding to 62 ° and 242 °, in both cases with a position of around 3200 G. The main peaks of these two curves exhibit a stronger signal, and are shifted horizontally at lower fields with respect to the curves corresponding to the angles 152 ° and 332 °, which is consistent with the full spectrum shown in Figure 4.18a. Furthermore, there seems to be no observable second peak at the angles 152 ° and 332 °.

4.3.3 Sample 34 - rods

The final FMR measurement was performed on Sample 34, being the sample in which the highest aspect ratio rods with largest spacing between them was obtained. Parameters for this particular sample were reported in Table 4.6. The resulting spectrum is displayed in Figure 4.19a together with a top-view SEM image of fallen rods. Similar to the lines in Sample 19, Sample 34 also exhibits clear evidence of anisotropy in the obtained spectrum. The uniform precession appear in a wave-like shape, generally with a slightly higher value of the main peak position, corresponding to the range 3000 to 3250 G and linewidth in the range 800 to 900 G, where higher field peak positions result in smaller linewidths in this particular case. Furthermore, a second peak seems to appear at angles corresponding to 86 ° and 266 °, exactly separated by an angle of 180 °. These angles are indicted by red arrows in the spectrum in 4.19a. Also for this sample also, there are no observable second peaks at angles in between 86 ° and 266 °.

Cross sections corresponding to the angles at which second peaks were observed are plotted in Figure 4.19b together with two angles in between. The angular cross sections considered from Figure 4.19a are 86 °, 176 °, 266 ° and 356 °. A second peak seems to appear at the angels 86 ° and 266 °, at a field strength corresponding to 4300 G in both cases, being the highest value observed for a second peak in this analysis. At these two angles, the uniform precession has been shifted horizontally towards higher fields, as oppose to Sample 19 where the shifting for second peak curves occurred in the lower field direction.

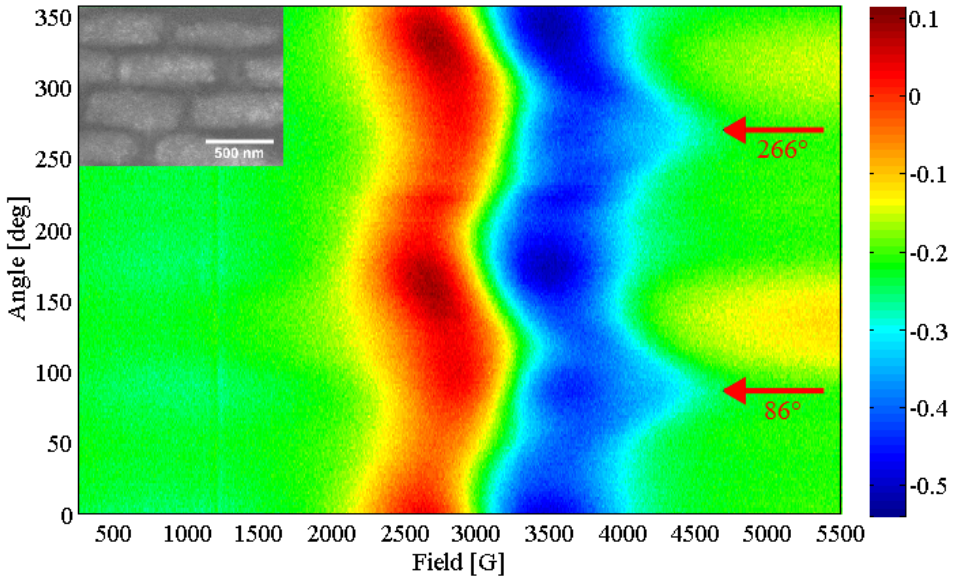

(a)

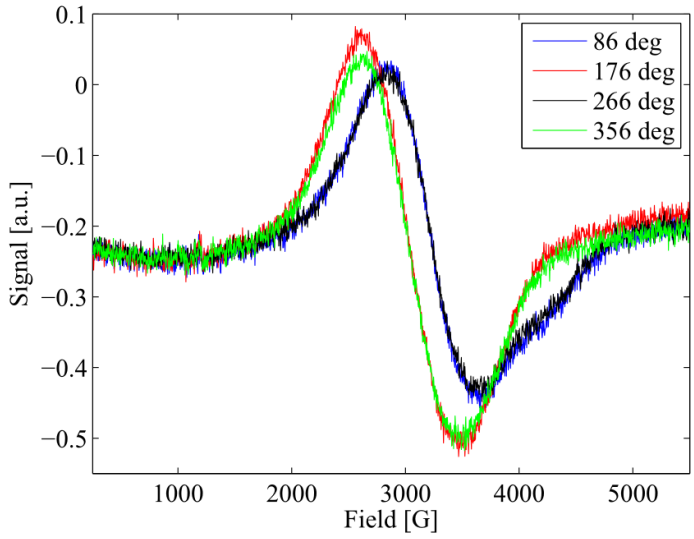

(b)

Figure 4.19: FMR spectroscopy results obtained for the rods in Sample 34, with parameters given in Table 4.6. Figure (a) shows a combination of the FMR spectra corresponding to each angle of the applied field. The signal is given as a color code corresponding to the colorbar with arbitrary units. Second peaks in the spectrum are indicated by red arrows, and an SEM image of Sample 34 is given. (b) shows the spectra corresponding to the angles 86 ° (blue curve), 176 ° (red curve), 266 ° (black curve) and 356 ° (green curve).

Chapter 5

DISCUSSION

As seen in the former chapter, there are several parameters that control the self-assembly process. This chapter discusses the physics behind the self-assembly process guiding the superstructure formation, followed by a discussion of the FMR results obtained for these superstructures.

5.1 The physics of self-assembly

There is no doubt that the self-assembly system considered in this work is complex with many parameters that can be tuned to control the outcome of the process. Magnetic moments associated with the nanoparticles, interact with the applied magnetic field and line up in its direction, allowing them to further interact magnetically with each other. It turns out that one-dimensional superstructure formation is a competition between magnetic dipole-dipole interactions and increasingly pronounced van der Waals interactions, in which the significance of the magnetic interactions is reflected through the degree of both superparamagnetism and up-lining as a function of the magnetic field strength. In addition, the distance between particles in solution, given by the number of particles and the dispersion volume, is imperative in order to obtain uniform ordered superstructures. Hence, it is likely to exist both optimal dispersion volumes and applied magnetic field strengths.

5.1.1 The significance of an applied magnetic field

Clearly the strength of the magnetic field has a profound influence on the outcome of self-assembly. This can be seen by taking into consideration the control Sample 0, Sample 6 and Sample 12, shown in Figure 4.1, 4.2a and 4.3a in Section 4.1, respectively. The three samples were self-assembled under identical conditions, except for the field strength which was set to 0, 500, and 20000 G, in the case of Sample 0, 6 and 12, respectively. The attention is first brought to the case of an absent magnetic field.

Zero field

In terms of zero field, only short range order was observed with the nanocubes situated in rather small supercrystal grains. Monte Carlo simulations performed

with zero magnetic field strength, shown in Figure 4.12 in the previous chapter, revealed a potential mechanism in this case. Governed by the van der Waals interaction and dipole-dipole interactions, nanocubes organize themselves face-to-face with top-view magnetic moments head-to-tail in a square manner, which effectively reduces the demagnetization field. Reducing the demagnetization field is also evident i the side-view as alternating positive and negative perpendicular components of the magnetic moment was obtained, at the same time as the magnetocrystalline anisotropy energy was kept to a minimum. If more particles were included in the simulation, there would probably have been several supercrystal nucleation sites in the defined volume box, giving rise to grains and short range order. Since the demagnetization field can be assumed to be effectively removed when crystals are formed, there is no longer a driving force to direct the individual grains in an ordered manner. The formation and size of the grains will of course depend on the kinetics of the process, regarding the rate of evaporation of the solvent, temperature, and the initial spacing between the particles. Furthermore, the morphology of the nanoparticles complicate things in terms of self-assembly into ordered superlattices. Cubic shapes exhibit lower symmetry than spherical shapes, which thus makes it harder to obtain long range order. If the particles exhibited spherical morphologies, the superlattice would be of the close packed type, thus making long range order more likely.

As outlined in Section 2.6, magnetite nanoparticles will be superparamagnetic for sizes under 26 nm at a temperature ~ 300 K, assuming spherical shape. Even though the particles exhibit cubic morphology, it would be safe to assume that 12 nm nanocubes are in fact superparamagnetic. Spontaneous flipping of magnetic moments between equivalent magnetic easy axes would result in weaker magnetic interactions, something which was not included in the Monte Carlo simulations. However, the local field exerted on one particle from the neighbouring particles, might be strong enough to lock the magnetic moment in the direction of this field. For instance, the local magnetic field from a 12 nm nanocube at a distance 16 nm is calculated to be 365 G, using Equation 2.32 in Section 2.7.2.

To investigate to what an extent the magnetic moment is locked in the direction of an applied magnetic field, magnetocrystalline anisotropy energy for a 12 nm nanocube in an applied magnetic field along the diagonal of the cube, $u_{\mathrm{A}}(r, \theta, \varphi) + u_{\mathrm{Z}}$ (see Table 3.1 in Section 3.2.1), with r set to 1, was plotted in a Cartesian coordinate system, displayed in Figure 5.1. As stated in Figure 2.13 in Section 2.6, the magnetocrystalline anisotropy energy landscape in the absence of an applied magnetic field showed eight equivalent minima in the direction of each corner. Figure 5.1a shows the energy landscape in an applied field corresponding to 100 G, and already at this field strength some of the minima start to disappear. The minimum corresponding to the direction of the field, located at approximately $(1, 3\pi/10, \pi/4)$, is getting deeper than the other remaining minima, and the minimum corresponding to the corner antiparallel to the field direction, located at approximately $(1, 7\pi/10, 5\pi/4)$, has been elevated considerably. At 150 G, displayed in Figure 5.1b, only two minima still seem to remain, that is, the

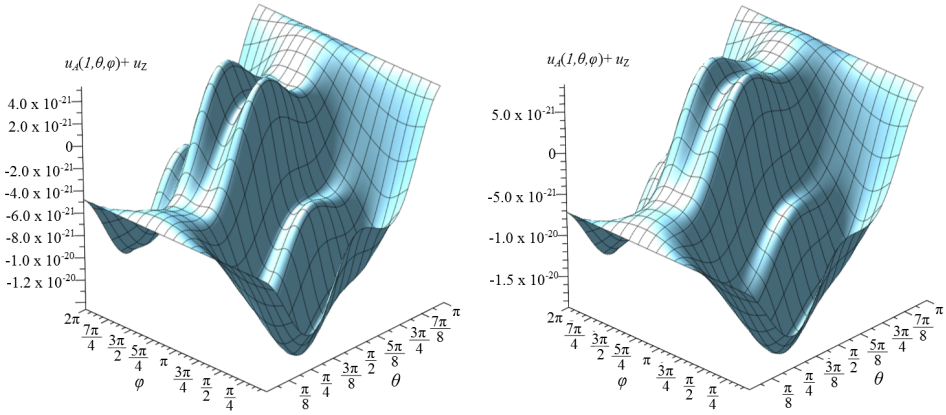

(a) 100 G

(b) 150 G

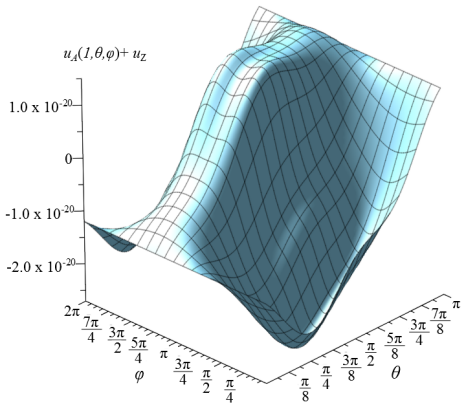

(c) 250 G

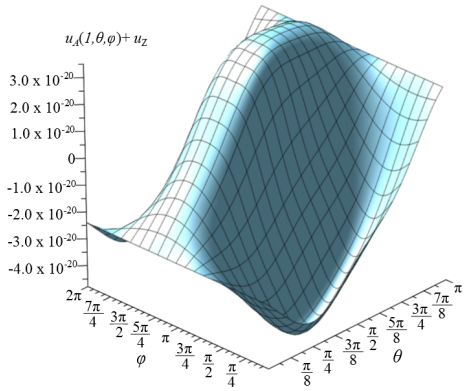

(d) 500 G

Figure 5.1: Magnetocrystalline anisotropy energy of a 12 nm nanocube in an applied magnetic field along the diagonal of the cube, $u_{\mathrm{A}}(r,\theta,\varphi)+u_{\mathrm{Z}}$, with r set to 1, and plotted in a Cartesian coordinate system. Figure (a), (b), (c) and (d) show the energy landscapes in an applied magnetic field corresponding to 100 G, 150 G, 250 G and 500 G, respectively. in the direction $(1, 3\pi/10, \pi/4)$.

minimum corresponding to the corner in the direction parallel and antiparallel to the applied field. By further increasing the field to 250 G in Figure 5.1c, the minimum corresponding to the corner in the direction parallel to the field is lowered even more, and the minimum corresponding to the corner in the direction antiparallel to the field is practically gone. Thus, the particle in an applied field of 250 G will probably exhibit a very low degree of superparamagnetism. At 500 G, the remaining minimum is further lowered relative to the 250 G case, as seen in

Figure 5.1d.

As the energy landscapes are established in Figure 5.1, relaxation times can be calculated using Equation 2.9 in Section 2.2.3. The attempt time τ_0 for magnetite was reported in the literature to be 10^{-9} s [51]. In the case of an applied magnetic field, two relaxation times need to be considered. τ_+ is associated with the relaxation from a lower minima to a higher minima, the lower one being the minima of the cube corner in the direction of the applied field, with coordinates $(1, 3\pi/10, \pi/4)$, and the higher one considered to be the corner antiparallel to the field, with coordinates $(1, 7\pi/10, 5\pi/4)$. τ_- is the relaxation from the higher minima and back to the lower one. Only the smallest existing energy barrier was considered, being in this case the energy barrier associated with the [110]-directions. At zero field (see Figure 2.13 in Section 2.6), for all minima $\tau_+ = \tau_-$, calculated to be $1.47 \cdot 10^{-9}$ s. As the field is increased to 100 G, τ_+ and τ_- were calculated to be $5.72 \cdot 10^{-8}$ s and $1.01 \cdot 10^{-9}$, respectively, yielding a ratio $\tau_+/\tau_- = 56.6$. When the field is increased to 150 G, the barrier associated with the [110]-direction is non-existing, and hence there is no minima any more. τ_- would therefore be equal to just τ_0. τ_+ was in this case calculated to be $3.57 \cdot 10^{-7}$ s, in which the corner at $(1, 7\pi/10, 5\pi/4)$ was considered to be the barrier. As a result $\tau_+/\tau_- = 357$ indicating that a transition from parallel to antiparallel direction will require a 357 times longer time than the relaxation back. For 250 G and 500 G, τ_+ was calculated to be $2.38 \cdot 10^{-5}$ s and 0.569 s, respectively, with a ratio of τ_+/τ_- equal to $2.38 \cdot 10^4$ and $5.69 \cdot 10^8$, respectively. Just for the sake of comparison, τ_+ is calculated for 750 G and 1000 G to be $1.36 \cdot 10^4$ s and $3.23 \cdot 10^8$ s, respectively. Depending on how the threshold for the locking of magnetic moment in the direction of field is defined, it would nevertheless be safe to assume that there exist a very low degree of superparamagnetism at least for magnetic field strengths of 500 G and higher.

In all experiments performed, except for the one in the absence of a magnetic field, the particles can be assumed to have been effectively ferrimagnets. Local fields from the neighbouring particles themselves will also make a contribution to the locking of magnetic moments. Neglecting superparamagnetism in the Monte Carlo simulations was therefore not a crude assumption, as no applied fields smaller than 250 G were considered. As for the zero field case, including superparamagnetism in the simulation may or may not have resulted in the same assembled structure as the one obtained in Figure 4.12 in Section 4.2.2. The question remains whether the the self-assembled system in zero field is superparamagnetic. Consider four particles with in-plane moment components in a head-to-tail square configuration and perpendicular components in a zigzag configuration. The field exerted on one particle from the three others, in the direction of the magnetic moment of the particle, is calculated from Equation 2.32 in Section 2.7.2 to be 758 G. By further considering a particle surrounded by eight other particles in the same configuration as in Figure 4.12, the field exerted on one particle from the three others is calculated to be 1194 G, which suggests that the self-assembled system in zero field is ferrimagnetic.

Applied uniform magnetic fields

When the magnetic field is switched on, the magnetic moments of the nanocubes immediately couples to the field through the Zeeman interaction, as described in Section 2.4. Assuming a perfectly uniform applied magnetic field, no net force is exerted on the magnetic particles by the field, as the attractive force on the appropriate pole is equal in magnitude but oppositely directed to the repulsive force on the pole with opposite polarity. The Zeeman interaction causes the magnetic moments to line up in the direction of the field, and the stronger the field, the stronger is the Zeeman interaction, and to a higher degree the magnetic moments of the particles tend to line up. This is reflected in the micrographs shown in Figure 4.2a and 4.3a, where 2000 G yields a higher degree of up-lining in the direction of the applied magnetic field than in the case of 500 G. Interestingly, fields below 750 G seem to consistently yield line formation with nanocubes oriented with the [100]-direction parallel to the applied magnetic field, as depicted in Figure 4.4. Furthermore, at 750 G the particles seem to adopt a mix of the [100]- and the [110]-configuration, and above 750 G a dominating [110]-configuration. This strongly suggests there exists a critical field H_{critical}, or a field strength interval in which a the $[100] - [100]$-transition is evident.

Results from the Monte Carlo simulations performed in Section 4.2.2 in the case of uniform fields at 500 and 2000 G, showed a behaviour consistent with experimental observation and gave valuable insight to the mechanism. At 500 G, the Zeeman interactions are not sufficiently strong enough to keep the magnetic moments of the nanocubes aligned in the field direction at all times, that is, rotational Brownian motion causes the moments to deviate with a certain average angle, found from the simulation to be $15.3\,^\circ$ in-field, such that the cubes self-assemble face-to-face with magnetic moments in a zigzag configuration, seen in Figure 4.13. This way, the magnetic moment is in a [110]-configuration with respect to the cube and the cube itself is in a [100]-configuration with respect to the applied field. As for 2000 G, the Zeeman coupling is so strong that only a slightest deviation from the field direction would cause an energy cost so great that this configuration becomes unfavourable. Hence, when the nanocubes are approaching each other, they still self-assemble in a face-to-face manner, but with moments locked in the direction of the field giving rise to the observed [110]-orientation, which is also more favourable in terms of magnetocrystalline anisotropy. Simulation results from Figure 4.15 report that the transition from [100]- to [110]-morphology might happen close to 750 G as mixed morphologies were obtained for this field strength, and field strengths of 250 G, 1000 G and 1500 G resulted in [100]-, [110]- and [110]-orientation, respectively. Interestingly the mean angular deviation of the magnetic moments in 750 G was smaller than in the case of 1000 G, for reasons unknown at this point.

The simulation does not, however, give any insight to what happens to the magnetic moments associated with the nanocubes when the applied magnetic field is relaxed. If the magnetocrystalline anisotropy is dominating, the moments will most probably relax the the nearest corner of the cubes, resulting in a

zigzag configuration, both in-plane and perpendicular to the plane for the [100]-morphology, and merely perpendicular to the plane for the [110]-morphology. If the local field from the neighbouring particles is strong enough, the moment might not reorient themselves much. Probably, the dictation of the final orientation of the moments would be a balance between both the magnetocrystalline anisotropy and the local field.

Gradients

When a gradient field is applied to the self-assembly system, a rather different mechanism occurs. In addition to lining up, there will exist a net force on the magnetic moments pulling them towards the the magnetic pole with the highest field strength. In the context of rod formation, gradients, together with high concentrations, seem to be significant when it comes to obtaining high aspect ratio structures, as seen in Figure 4.8. One possible mechanism in the formation of rods is that the gradient is pulling the nanocubes towards the pole, and the nanocubes are simultaneously experiencing a local field from the neighbouring particles governing up-lining as they are pulled towards the pole. This way, regions of higher local concentrations are obtained in the remaining volume in the final stage of the process, which could potentially turn into rods.

The Monte Carlo simulation, performed for the growth of a single rod in Figure 4.16, shows how particles are more and more clustered together as the volume evaporates, before eventually forming a rod. Interestingly in this case, the nanocubes are oriented in [110]-manner with respect to the vertical field, consistent with experimental results. Although it is important to keep in mind that the simulation was performed with an evaporation rate and a gradient five orders of magnitude higher than the actual parameters used in experiments, the results still give some valuable insight to how the rods are formed. The gradient, both used in the simulation and experiments seems nevertheless to be sufficiently strong so that particles are not aggregating in the solvent air interface as result of a too high evaporation rate.

Optimal magnetic field strength

The question arises if there exists an optimal applied magnetic field strength, H_{optimal}, at which narrow uniform monolayered lines and high aspect ratio rods can be obtained, and why. In terms of narrow monolayered lines, the magnetic field strength study with results reported in Figure 4.4, seems to reveal that $H_{\text{optimal}} \sim 500\,\text{G}$ for the system considered in this work, as seen in Figure 4.4b. Furthermore, this result, in spite of being subjected to film compression, is consistent with the result obtained for the solvent amount study at 500 G at basically the same conditions, shown in Figure 4.2c. As the attention is again directed to how the lines are forming, Brownian motion could explain why different

morphologies are obtained at different field strengths, like in the field strength study in Figure 4.2c. The magnetic interactions between the particles at H_{optimal}, are just strong enough such that the particles have time to diffuse together into monolayered narrow lines at the end of the self-assembly process, when most of the volume has evaporated.

When the magnetic field is decreased, it will result in a higher degree of rotational Brownian motion. This will in turn cause a weaker magnetic interaction between the nanocubes, which thus causes the line formation to take a longer time, giving the van der Waals interaction an advantage. Fewer but wider and thicker lines can be expected in this case, explaining the result in Figure 4.4a for 250 G. If the field is increased above 500 G, the Zeeman interaction is sufficiently strong such that a higher degree of up-lining can be expected. This will in turn result in a more rapid line formation at several height levels in the solution, and as the solvent has evaporated significantly, lines stack on top of each other. This explains why only bilayered, or thicker, superstructures were forming in the solvent study at 2000 G, as reported in Figure 4.3.

Interestingly, Figure 4.4 reveals that bilayers are starting to form already around 750 G. It also looks like from this figure, that at fields corresponding to 1000 G or higher, causes a twisting in the lines, something which is difficult to explain according to the knowledge at this point. The system of consideration is truly complex, and twisting could have occurred as a combination of high field and film compression, as the samples in Figure 4.4 were in fact observed to be subjected to film movement upon acetonitrile injection. However, the result obtained in Figure 4.3c, consistent with the result from Figure 4.4f obtained under the same conditions, was obtained with minimal film movement prior to lift-off, which suggests that the twisting might happen during the actual self-assembly process, but interestingly only for a dispersion volume close to 60 µL.

In terms of rod formation, higher magnetic fields seems to give more uniform and higher aspect ratio rods than lower fields, as outlined in section 4.1.6. This is a rational result considering that the alignment of the magnetic moments becomes more profound for higher field, which would in turn result in a higher degree of one-dimensionality. In terms of gradients, an existing force exerted on the particles will be pulling them towards the pole with the strongest field, which might cause induced nucleation and rod growth. A too strong gradient might not be favourable due to a kinetic effects dominating the process, which may case amorphous structures. As for Figure 4.8, the gradient considered did not seem to make much of a difference of the one-dimensionality of the obtained structures, although smaller standard deviations in cross section size and height for larger gradients seemed to occur.

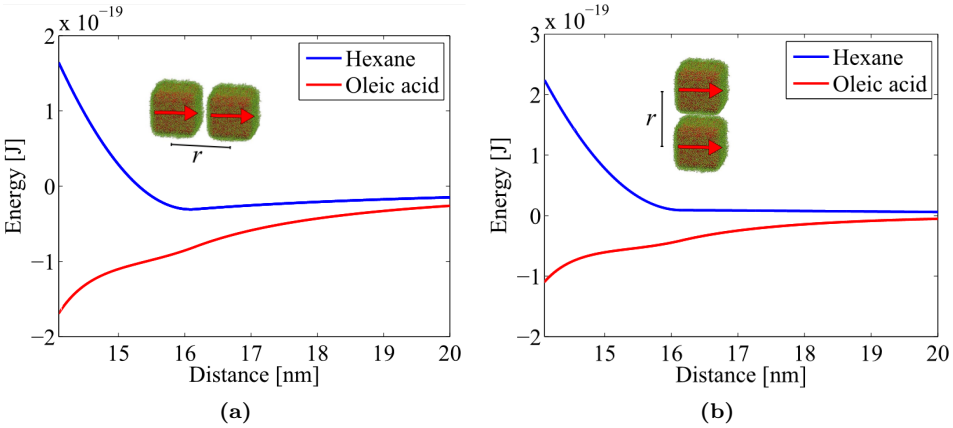

Figure 5.2: Sum of interparticle potentials from Table 3.1, with parameters from Table 3.2. Magnetic dipole-dipole interaction, van der Waals interaction, and steric repulsion in the outer regime corresponding to $a + L < ra + 2L$, are considered for two 12 nm nanocubes with a face-to-face configuration in both hexane and oleic acid. Figure (a) displays interaction energies between the nanocubes with parallel magnetic moment at angle 0. (b) displays the same energy at an angle of $\pi/2$.

5.1.2 The role of oleic acid

The oleic acid study shown in Figure 4.6 in Section 4.1.4 performed at a uniform magnetic field strength and total dispersion volume corresponding to 500 G and 60 µL, respectively, shows that adding an excess amount of oleic acid is imperative in the formation of ordered self-assembled structures. At a rather small oleic acid concentration of 5 µL/mL, only distorted structures with only traces of lines were observed. Singh et al. reported the same importance of excess oleic acid, in which no excess resulted in highly distorted structures [22]. It is evident from the oleic acid study that increasing the oleic acid concentration somehow causes the particles to aggregate and form ordered structures.

When the oleic acid concentration is increased, two important features happen. First of all, the viscosity of the solvent increases with increasing oleic acid concentration, causing the friction coefficient (see Equation 2.21 in section 2.7.2) to increase and particles to diffuse slower than in pure hexane. Secondly, the van der Waals interaction and steric repulsion between particle changes considerably, as outlined in the Figure 3.3 in Section 3.2.1. A sum of the potentials displayed in Figure 3.3 is plotted in Figure 5.2 for two a =12 nm magnetite nanocubes with a surfactant layer of L =2.08 nm, in both hexane and oleic acid. The range of interaction considered is $a + L < r < 20$ nm, that is, only the outer regime of the steric repulsion in which only free energy of mixing exists. Figure 5.2a, in the case of parallel magnetic moments situated at an angle of 0 with respect to each other,

shows two completely different behaviours in hexane and oleic acid. In hexane there is as small minimum close to a center-to-center separation of $2L$. The depth of this well is $\sim 4k_BT$, meaning that two cubes situated face-to-face with parallel magnetic moments are likely to aggregate. In oleic acid, the well is decreasing towards a depth which is one order of magnitude deeper than in hexane. At the bottom of this well the steric repulsion in inner regime $a < r < a + L$ will make a jump of approximately two orders of magnitude in the positive energy direction, as can be seen for this potential in Figure 3.3b. In the case of parallel magnetic moments situated at an angle of $\pi/2$ with respect to each other, as shown in Figure 5.2b, the potential minima in hexane is gone and only positive energies are present resulting in a repulsion between the particles at all separations r. In oleic acid, the energy is still negative at all separations in the considered range but with a smaller decrease towards the bottom relative to orientation at angle 0. One point is immediately clear from this observation; the van der Waals interaction in oleic acid is completely domination the steric and magnetic repulsion in the considered range, which will result in an aggregation of particles. Thus, a dispersion with a high oleic acid concentration will not be stable over time, but is imperative in the final stage of self-assembly to obtain ordering.

As the oleic acid concentration increases, magnetic field induced self-assembly yielded a higher degree of one-dimensionality in the obtained structures, as seen in Figure 4.6. Figure 4.6b and 4.6c show that the nanoparticles are forming bilayered lines or thicker, respectively, as the oleic acid concentration is increased from 20 µL/mL to 30 µL/mL. At 30 µL/mL, individual lines even start to stick to each other, and a further increase yielded thicker and wider lines more or less merged into each other. The results clearly shows that the higher the oleic acid concentration the faster the nanoparticles start to aggregate as a result of dominating van der Waals interactions.

In terms of an optimal oleic acid concentration, $c_{\text{oleic acid}}^{\text{optimal}}$, for narrow monolayered lines, the concentration has to be high enough so that the entire sample is uniformly covered, but at the same time low enough so that van der Waals interactions start to be dominating at the very final stage of the self-assembly process when the particles are lined up in separated lines. Furthermore, the oleic acid matrix in which the lines are embedded should be sufficiently thick to make the lines less prone to distortions. From the oleic acid study, $c_{\text{oleic acid}}^{\text{optimal}}$ seems to lie somewhere between 10 µL/mL and 20 µL/mL. Considering the line optimization reported in Figure 4.7, the most narrow monolayered lines with largest spacing was actually obtained for Sample 25 at an oleic acid concentration of 12.5 µL/mL, suggesting that the optimal concentration lies closer to 10 µL/mL than 20 µL/mL. It is important to keep in mind that only one experiment was performed at 12.5 µL/mL, and that other factors not considered, such as temperature fluctuations, may also have contributed to optimal lines for this particular sample.

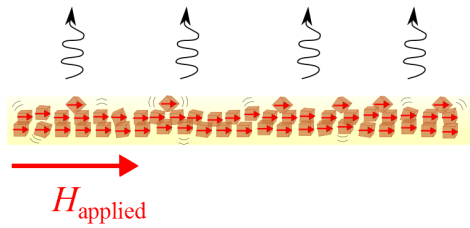

(a) $V < V_{\text{optimal}}$

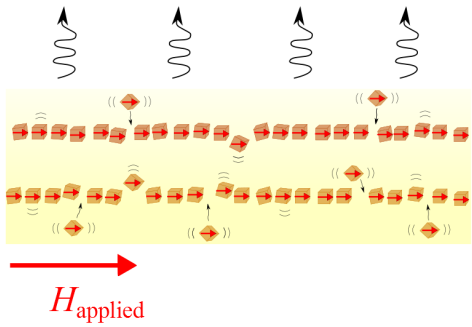

(b) $V = V_{\text{optimal}}$

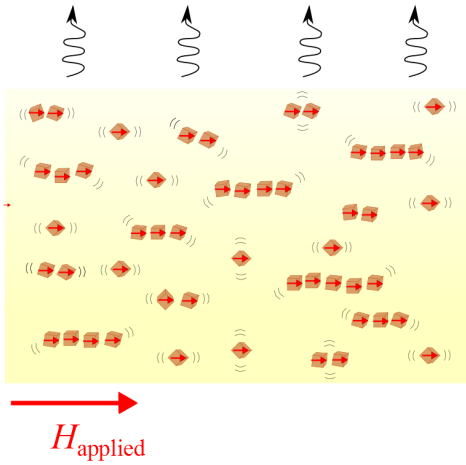

(c) $V > V_{\text{optimal}}$

Figure 5.3: Proposed mechanism of self-assembly of a fixed number of magnetic nanocubes at different dispersion volumes. The direction of the applied magnetic field is indicated, and it is assumed that the field is strong enough such that the indicated magnetic moments of the nanoparticles are aligned in the direction of the field at all times. Surfactants are not shown. Figure (a) shows self-assembly with a too low total dispersion volume for line formation. (b) shows optimal volume for line formation. (c) shows a too large volume for optimal line formation.

5.1.3 The role of the dispersion volume in line formation

It is also clear from the obtained results that the total volume of the dispersion of nanoparticles is important, in terms of obtaining separated lines. Given H_{optimal} $\sim$ 500 G and a fixed number of particles, this can be understood from a diffusional point of view, in which larger volumes provides both a longer diffusion time for the particles and a larger region in space at which the particles are allowed to move. As the solvent evaporates, this region becomes smaller, and that is when particles start to interact with each other. If the magnetic moments of the particles are perfectly oriented in the direction of the field, particles close to each other will interact in a way that reduces the total free energy of the system.

It might not be hard to imagine that, given an area constraint, a fixed number of particles and a solvent, there exists an optimal volume, V_{optimal}, at which particles self-assemble into one-dimensional superstructures in a static magnetic field. If the volume is too small, the particles will not have time to diffuse and line up, and thus more disordered structures can be expected, as illustrated in Figure 5.3a. This phenomenon is also reflected through the obtained results, such as the cases of Sample 6 and 7 depicted in the Figures 4.2a and 4.2b, from the solvent amount study at 500 G. Basically the same phenomenon could be observed in the Figures 4.3a and 4.3b, depicting Sample 12 and 13 from the solvent amount study at 2000 G, in which disordered structures are obtained.

If the dispersion volume is too large, the particles are allowed to diffuse for a longer period of time. Hence, there would be a higher probability for one particle to approach and interact with another one at still significant volumes. At one point, there would likely be short lines of nanocubes which itself would diffuse around in the solution and interact with other short lines of nanocubes, as illustrated in Figure 5.3c. Short lines in the solution will in turn move slower, due to suppressed Brownian motion, causing the line assembly to take a longer time at the final stage of the process. Transmission electron microscopy images, obtained by Singh et al. [22], shown in Figure 5.4, show that short lines consisting of 12 nm magnetite nanocubes are indeed forming when the number of particles is low compared to the volume.

The higher the dispersion volume at the initial stage of the self-assembly process, the shorter would the lines be, and the higher is the number of lines present in the solution at at certain time point at the initial stage of the self-assembly process. As the solvent evaporates the lines approach and interact with each other as independent units. Suppressed diffusion of these short lines causes the assembly into longer lines, in a head-to-tail manner, to take a longer time, such that the majority of units do not make it. This would give van der Waals interactions an advantage, causing the lines to stick perpendicular to the lengthwise direction. If the there exist a higher number of short lines, like it presumably would at large volumes, the process will yield on average shorter, but wider and thicker self-assembled lines. This seems consistent by reviewing the Figures 4.2d and 4.2e, in

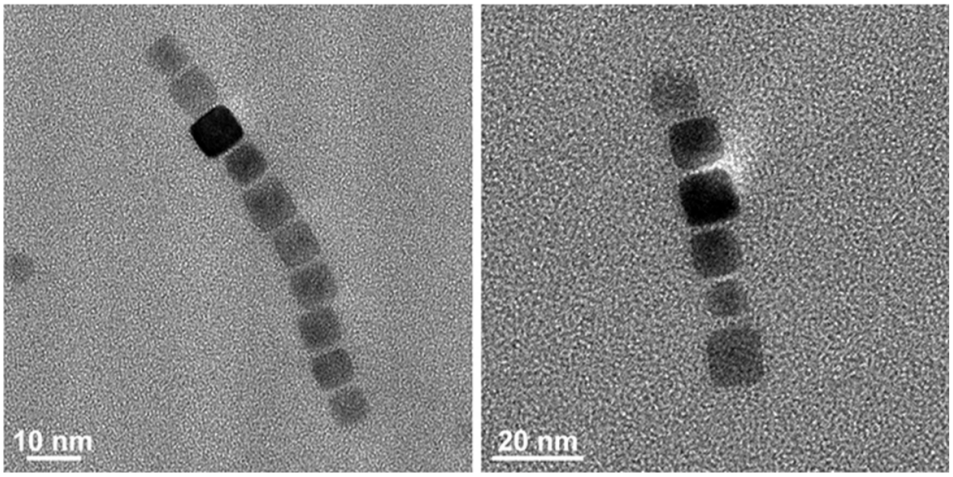

Figure 5.4: TEM micrographs showing short lines consisting of 12 nm magnetite nanocubes, obtained at a low number of particles compared to the solvent volume. Taken from [22].

the case of Sample 4 and 5, at 500 G. The same trend can be observed in the Figures 4.3d and 4.3e, depicting the structures obtained for Sample 15 and 16, at 2000 G. Interestingly, at very high volumes, like in the case of Sample 17, shown in Figure 4.3e, where 200 µL was used, this effect seems even more pronounced. It seems like very high volumes yield very short and evenly distributed lines, with a length of just a few nanocubes, which self-assemble into monolayered islands during evaporation. These islands seem rather evenly distributed over the substrate, but some of them were sufficient close to interact magnetically with each other and thus merge into each other in a heat-to-tail fashion, with the aid of van der Waals interactions.

Finding V_{optimal} for line formation is all about finding a balance between the rate of evaporation and the average distance between evenly dispersed nanoparticles, allowing them to diffuse and self-assemble into long lines before all the solvent has evaporated. This is illustrated in Figure 5.3b. From the solvent amount studies performed at both 500 G and 2000 G, shown in the Figures 4.2 and 4.3, respectively, it may seem that in the case of a cup with diameter of 2 cm, this optimal volume turns out to be close to 60 µL. The lines in the Figures 4.2c and 4.3c, at 500 G and 2000 G, respectively, seems to exhibit the most uniform and, not to mention, the most narrow width.

A proposed self-assembly mechanism at both optimal volume and applied magnetic field is illustrated in Figure 5.5. Surfactants are not shown in the figure. At the initial stage of the self-assembly, right after the magnetic field is switched on, the magnetic moments associated with each nanocube align themselves in such a way

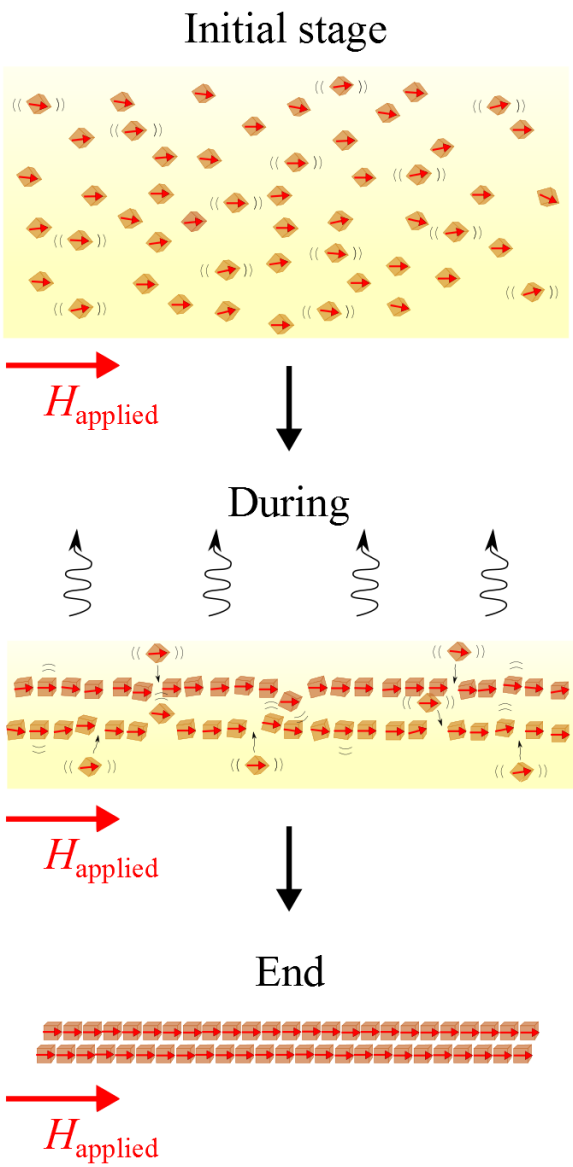

Figure 5.5: Proposed mechanism of self-assembly of magnetic nanocubes at optimal dispersion volume and applied magnetic field. The direction of the applied magnetic field is indicated, as well as the dipole moments of the nanocubes. Surfactants are not shown. At the initial stage, particles are uniformly dispersed. During evaporation, the particles approach each other and diffuse into lines with magnetic moments in the direction of the applied field. Finally as the solvent has evaporated, lines of nanocubes are left behind on the surface.

that the magnetic easy axis is directed in the direction of the applied magnetic field. However, rotational Brownian motion causes a certain probability for a small deviation from the direction of the field, as established above from the simulations. The magnetic interactions between the particles are just strong enough such that the particles self-assemble into monolayered narrow lines at the end of the self-assembly process, when most of the optimal volume has evaporated. Governed by the increasing van der Waals interactions, the cubes align face-to-face with a certain spacing between them, perpendicular magnetic moment components close to zero and in-plane components in a zigzag configuration.

5.1.4 The significance of the number of particles

As the optimal volume and field is established for line formation, the discussion is directed towards the batch concentration and the total concentration of the nanoparticle dispersion. The same discussion applies for rod formation as well.

Lines

In terms of lines, it seems like a nanoparticle batch concentration of 2 mg/mL yields both narrow and uniform lines, but not sufficiently separated. Ideally the lines should be separated to such an extent that a a slight film movement prior to lift-off does not bring the lines into contact. Furthermore the density of lines should also be sufficiently high such that a clear signal can be obtained in subsequent FMR characterization. Figure 4.7a and 4.7b show in the case of Sample 18, that increasing the batch concentration to 3 mg/mL, and at the same time keeping the volume and magnetic field fixed at 60 μL and 500 G, respectively, yields a higher density line formation. Some of the lines were aggregated into bundles, possibly due to film compression prior to lift-off, but it nevertheless seems like most of the lines consist solely of monolayers. Figure 4.7c and 4.7d show in the case of Sample 19, that the density of lines is reduced significantly if only 10 μL is taken from the 3 mg/mL batch followed by dilution to 60 μL. This corresponds to half the number of particles self-assembled in Sample 18. Thus, fewer lines with a larger spacing between them, are forming in the solution . Since the volume is optimal, there are no stacking of lines heightwise. There must, however, exist a minimum number of particles n_{min}, below which lines are not forming at V_{optimal} and H_{optimal}, but islands like in the case of Sample 12 in Figure 4.3e. Similarly there must exist a maximum number of particles, n_{max}, above which two-dimensional structures are forming rather than lines.

From Sample 18 and 19, with parameters given in Table 4.5, it seems like it might be possible to tune the density of lines by controlling the batch concentration and keeping all other parameters constant. Interestingly enough, the optimal volume seems to be 60 μL regardless of the number of particles in the dispersion, as long as this number lies between n_{min} and n_{max}. It might be tempting to think that the

concentration of particles after dilution is an important parameter, but it is really the volume in which the particles are dispersed, that is the critical parameter. Taking Sample 19 into consideration, the total concentration of the dispersion is 0.5 mg/mL. It might seem that this is equivalent to taking 20 μL from a 2 mg/mL batch and diluting it to 80 mg/mL, yielding basically the same concentration. However, Sample 4, shown in Figure 4.2d, shows that this is not the case. This is because the area of the cup is held fixed, and the thickness of the liquid film in the initial stage of self-assembly is different for the two samples, being of course greater in the case of 80 μL. A too thick liquid film would just give line formation at different heights to a greater extent, which in turn would lead to wide multilayered self-assembled lines at the end of the self-assembly process. Hence, the volume, and thus the thickness of the liquid film, is the critical parameter, given a number of particles between $n_{\min}$ and $n_{\max}$.

Rods

The nanoparticle concentration study in terms of rod formation, reported in Figure 4.9, shows how rod morphology and aspect ratio, self-assembled at a constant volume and magnetic gradient field, changes with the number of particles involved. Since the rods are growing heightwise, a larger number of particles is required relative to monolayered line growth. At a concentration of 3 mg/mL, discs were obtained as a result of too few particles in solution. Further increase to 5 mg/mL yielded dense short thin filaments, with a height slightly larger than the 3 mg/mL-case but with a smaller cross section size, as reported in Figure 4.11. However, the filaments were densely packed only in islands on the sample surface, and thus there existed regions where no filaments were observed. A higher local number of particles would result in a larger number of nucleation sites in solution, which might serve as an explanation to why a smaller cross section size is obtained for 5 mg/mL in the islands. As for 9 mg/mL, the height was further increased as expected, and the cross section size had also increased relative to 5 mg/mL with a larger obtained spacing between individual rods. With more particles the cross section size grows bigger at the expense of spacing between the rods, compared to the 5 mg/mL-case. In general, increasing the number of particles in the self-assembly experiments with a vertical gradient field resulted in increased mean aspect ratios, as reported in Figure 4.11 for Sample 32, 33 and 34.

Another way to increase the aspect ratio of self-assembled rods is to keep the concentration constant and increase the volume used in the experiment. 40 μL was used as a standard volume in vertical magnetic field experiment, except for Sample 35 depicted in Figure 4.10 for which 100 μL was used. This resulted in high aspect ratio filaments, densely packed. No straight continuous filaments could be observed inset of Figure 4.10, indicating that nucleation may have happened at several height levels resulting in a high degree of distortions along the filaments, explaining the observed standard deviation in height for this particular sample in Figure 4.11.

5.1.5 Advantages and disadvantages using an electromagnet

Using an electromagnet in self-assembly has several advantages associated to it, but also a few limitations. Indeed, the ability to tune the magnetic field as desired by simply controlling the current through through the electromagnet is considered a useful asset and have proven important in terms of self-assembly of magnetic nanoparticles and obtained structures. Electromagnets can also be used to obtain highly uniform tunable fields, something which is difficult and experimentally cumbersome in terms of permanent magnets. However, generating high fields requires high currents causing heating of the magnet, which again requires some form of cooling, for instance with water, to keep the temperature constant. Maybe the most disadvantageous feature, at least in terms of magnetic field induced self-assembly, is an existing radial magnetic field gradient on the poles. This radial gradient arises as a result of the rim of the pole being closer the coils in which current is passing through, thus generating a stronger field at this location and a weaker field in the center of the magnetic pole. Even though the vertical field is uniform, there would still exist a radial gradient which might make a difference in terms of self-assembly. This could serve as an explanation for why high standard deviations were observed in the context of rod formation in Figure 4.11. Perhaps it is the reason why rods with aspect ratio close to 2 were obtained in a uniform vertical field, since obtaining self-assembled film merely from the center of pole, where the field is most uniform, is inevitable.

5.2 FMR interpretation

In terms of the main peak corresponding to the uniform precession, the spectra reported in Figure 4.17, 4.18 and 4.19, in Section 4.3, of the considered three samples expressed evident shape anisotropy reflected from the structures associated with the samples. Interestingly, all three samples subjected to FMR spectroscopy seemed to result in second peaks in the FMR spectrum, at two different angles separated by exactly 180 °. These second peaks most probably correspond to excited low k spin waves in the magnonic structures.

5.2.1 Control sample

Interestingly enough, second peaks were observed in the control sample, a two-dimensional system being more or less isotropic. This may indicate that there were parts of this sample that exhibited long enough order, allowing magnons to be excited. The fact that the second peaks in this spectrum appeared at two angles separated by exactly 180 °, indicates that the magnons were excited only along this specific direction along which the ordering was expressed. Furthermore, the fact that the position of the peaks, at approximately 2400 G, corresponding

to uniform precession were more or less angle independent, shows that there is a low degree of shape anisotropy as it would be in the context of a more isotropic system.

From Figure 4.17b, it seems like the main peak is slightly wider at the angles 62 ° and 242 °, at which spin waves were not observed. From Section 2.4, it was stated that the width of the main peak describes the degree of damping in the structure. In principle for two-dimensional structures, the wider the linewidth, the higher degree of damping. Figure 4.17b reports a more narrow peak in the directions at which spin waves possibly were excited, which can also support the suggestion that there exists less disorder in the superstructure along this direction.

An interesting analysis would be to compare the control sample to a magnetite thin film of equal thickness. Consider a magnetite thin film comprising a single crystal with in-plane saturation magnetization and thickness 12 nm. To account for a disordered surface layer, the bulk saturation magnetization should me multiplied with a factor of 0.9, as justified in Appendix A.4. With a bulk saturation magnetization and g-factor reported in Section 2.6 to be $4.80 \cdot 10^5$ A/m and 2.12, respectively, the magnetic field corresponding to the main peak position for a frequency of 9.39 GHz can be calculated according to the Kittel formula reported in Section 2.4, in which demagnetization factors $N_x = N_z = 0$ and $N_y = 1$ are used. This yields a peak position close to 1450 G. This value is about 1000 G smaller than the peak obtained for the control sample, suggesting that a smaller effective magnetization in the case of the control sample requires a higher external applied magnetic field to align the magnetic moments to obtain resonance, than it would in a continuous thin film. This is highly consistent with the obtained results from the Monte Carlo simulations performed in Section 4.2 at zero applied magnetic field, in which the moment associated with the nanoparticles arranged themselves in a square manner seen in top-view. As established earlier in this chapter, the magnetic moments associated with the nanocubes seemed to be locked in the ferrimagnetic state due to the local field from the neighbouring nanoparticles, suggesting that the self-assembled system of the control sample is ferrimagnetic. Results from the FMR analysis strongly suggest that this system is in fact ferrimagnetic from the existence of second peaks in the spectra, which could not have been obtained for a superparamagnetic system.

5.2.2 Lines

As expected, the lines of Sample 19, shown in Figure 4.7c and 4.7d, resulted in a completely different FMR spectrum than the control Sample. First of all, the main peak corresponding to the uniform precession exhibited an angle dependence, reflecting the shape anisotropy of the system. When the applied field is directed parallel to the lines, the majority of spins are aligned in a head-to-tail manner, as in Figure 2.4 in Section 2.2.2. Conversely, when the magnetic field is applied in the direction perpendicular to the lines, the majority of spins are aligned side-by-side

in parallel manner corresponding to an unfavourable energy associated with the system. This explains why a higher magnetic field needs to be applied in order to compensate for the energy cost of the side-by-side alignment, and thus line up the spins and give rise to the uniform precession peak. To compare the main peak of the lines consisting of nanocubes to a continuous film with the same aspect ratio, a similar analysis as in the case of the control was performed for the lines, using the Kittel formula. Considering a monolayered line with an average line width of four nanocubes oriented with the [100]-direction along the lengthwise direction, this would correspond to an aspect ratio of $12\,\mathrm{nm}/54\,\mathrm{nm} = 2/9$. The line can be approximated by a special case of an ellipsoid, assumed to be infinitely long along one of the principal axes, with magnetization along this axis. By setting $N_z = 0$, N_x and N_y can be found to be equal to $9/11$ and $2/11$, respectively, knowing that $N_x/N_y = 2/9$ and that $N_x + N_y = 1$. From this, the field strength associated with the position of the peak is found to be close to 890 G, considerably smaller than the equivalent peak of the lines with nanoparticle, found to be close to 2500 G. As in the case of the control sample, this also reflects a lower degree of magnetization along the lines consisting of nanoparticles than in the equivalent continuous film, consistent with the results obtained from the Monte Carlo simulation in Figure 4.13 in Section 4.2.2, where magnetic moments deviating from lengthwise direction of the line were obtained.

From Figure 4.18a, it can also be observed that the second peak appears at the angles at which the spins are aligned in a head-to-tail manner parallel to the lines, which suggests that the observed spin waves are excited upon these alignments as well. The spin waves could in theory be excited along the lines when the spins are aligned perpendicular to the lines, that is with $\mathbf{k}$ perpendicular to the magnetization, but these exhibit higher energy and thus require higher magnetic fields than the range used in this FMR characterization, in order to be excited [25, ch.10]. Moreover, at the length scale in question the exchange interaction, which plays a vital role in excitations with perpendicular $\mathbf{k}$, is effectively decoupled, suggesting that this kind if excitation does not take place.

Lines of Sample 19 expressed a [100]-morphology, and would probably have had moments oriented along the magnetic hard directions when spin waves were excited. The Monte Carlo simulations performed in uniform magnetic fields showed that high fields (higher than 750 G) tend to yield lines with particles oriented along the [110]-direction. Thus upon magnetization along this direction, a lower energy associated with magnetocrystalline anisotropy would be a reality which would in turn require lower external applied magnetic field to reach the resonant condition. Magnons may or may not be excited at lower field strengths. In this case the alignment of spins might be better, but nanocubes in a line with aligned spins along the [110]-direction will also result in an increased distance between the moments, and thus a weaker dipole-dipole coupling.

A different feature that might be looked upon as related to the long range order the lines expressed, is the position of the second peaks in this FMR spectrum,

relative to the position of the second peaks in the FMR spectrum of the control. As reported in Section 4.3, the second peaks in the FMR spectrum of the control appeared at a field strength of 3900 G, whereas in the case of lines the position was 3200 G. This might be reflected in the ordering of the superstructure, in which higher degree of order allows low k magnons to be excited at lower fields, like in the case of the ordered lines. It is important to keep in mind that the magnetic moments of the nanoparticles in the control was not found to be ordered in lines, which might be a contributing factor to an observed peak position at higher fields for the control. Therefore a measure of order can not be directly inferred merely from the second peak positions. There also might be an additional third peak in the spectra corresponding to 62 ° and 242 ° in Figure 4.18b, but the reported signal is too poor to draw any certain conclusions.

5.2.3 Rods

It is immediately clear from the main peak in the FMR spectrum of Figure 4.18 that for Sample 34, exhibiting superstructured rods, the shape anisotropy is well represented, similar to the lines. Compared to the lines, the main peak position occurs generally at higher fields, something that might be due to the observed morphology in which nanocubes seem to have grown around the lengthwise axis of the rods. According to the results from the Monte Carlo simulation in Figure 4.16, the majority of the magnetic moments were aligned vertically along the [110]-direction of the cubes at basically the same applied field strength used in the experiment. Hence a rather small magnetocrystalline anisotropy energy compared to the lines would be associated with a smaller field at the resonance condition. This is not, however, the case which might suggest that the nanocubes are not well ordered within the rods of this particular sample.

The main peak for the rods was also observed to be generally wider than for the control and the lines. This might not be reflected solely by the damping mechanism in the rods. If the rods are looked upon as three-dimensional objects rather than one-dimensional, magnetic dipolar coupling between the particles situated in a three-dimensional array might be the origin to the observed wide peak. In addition, as outline in Section 4.11, there is a distribution of heights in the Sample. Given a similar morphology for all the rods, in terms of the orientation of nanocubes within the rods, a higher rod will require a smaller field in order to align the magnetic moments due to the contribution from shape anisotropy, and conversely a shorter rod will require a higher field. A height distribution might therefore result in broader main peaks.

A rather peculiar feature about the FMR spectrum obtained for the rods is that the curves in 4.18b show a shift towards a higher field for the main peak at angles where a second peak also appears, relative to angels where no second peak appears. As stated above, the opposite behaviour was observed for the lines where the position of the main peak was shifted towards lower fields. What can be observed

in the SEM images for the rods in Figure 4.9f, is that some of the rods have fallen over and were thus lying horizontally on the substrate. A possibility is that the second peak in the FMR spectrum of the rods actually comes from the uniform precession associated with the fallen rods as the field is directed perpendicular to the plane of the substrate. However, this does not explain why the main peaks at these angles are shifted towards higher fields. Another possibility is that the peak positions corresponding to the smallest field were obtained from the vertical rods, since the signal is slightly stronger at these specific angles, and that the peak positions shifted towards a higher field correspond to the fallen rods. These fallen rods may have fallen like dominos with the majority of rods with their lengthwise direction close to the in-plane field direction, and a minority with their lengthwise direction with a large deviation from the in-plane field direction. This way the main peak might at the angles in-plane is shifted slightly compared to the angles perpendicular to the plane, and the second peak corresponds to the rods with a lengthwise direction strongly deviating from the direction of the applied field.

Chapter 6

CONCLUSIONS

The method of liquid-air interface self-assembly in a magnetic field can be employed to successfully fabricate ordered one-dimensional superstructures consisting of 12 nm magnetite nanocubes. This method offers great flexibility in terms of the direction and strength of the applied magnetic field, as well as the size, morphology and concentration of the nanoparticles involved, which can be used to an advantage to produce several kinds of desired superstructures at a shorter timescale than conventional methods.

Markov Chain Monte Carlo simulations can indeed be performed to give valuable insight to the behaviours of nanoparticles in a self-assembly system. Since the self-assembly system is highly complex and expresses several degrees of freedom in terms of both motion and interactions, numerical simulations serve as an excellent tool to give insight to and support experiments on a theoretical basis.

Solvent amount studies, performed at uniform magnetic field strengths of 500 and 2000 G, seemed to yield the most uniform narrow lines at a total dispersion volume of 60 μL, which indeed seemed to be close to the optimal amount. The magnetic field strength study, performed at the optimal volume 60 μL, gave the best line formation, in terms of width and uniformity, at a field strength of 500 G, which seemed to be close to the optimal field strength for the self-assembly system considered in this work. An excess amount of oleic acid was found to be critical in obtaining ordered self-assembled structures, and in the context of lines the optimal concentration seems to lie in the range 10 to 20 μL/mL. Upon decreasing the number of particles in the solution, still keeping the volume and magnetic field strength at optimal conditions, separated narrow monolayered lines were obtained, exhibiting on average a width of only 5 nanocubes, and a spacing of approximately 3 μm. Interestingly, lines obtained from the experiments at field values below 750 G seems to consistently express a [100]-morphology, and above a [110]-morphology, suggesting that there might be a transition at 750 G. This result was highly consistent with the Monte Carlo simulation results in which a mix of the two morphologies were obtained at 750 G.

In terms of rods, the studies performed with varying magnetic field strengths and gradients, as well as concentration of nanocubes and dispersion volume, revealed that the level of one-dimensionality in terms of aspect ratio tend to increase with increasing magnetic fields, but did not seem to show any clear correlation to the value of the gradient. In addition, increasing both concentration and volume resulted in an increase of aspect ratio. The height of the rods seems to increase with both higher field and concentration, but no certain correlation

was found for the cross section size. More experiments need to be conducted in order to accurately establish the importance of a gradient field and its correlation to structure dimensions.

Experiments supported by the Monte Carlo simulations revealed valuable insight to the rich physics the self-assembly mechanism considered in this work represents. Self-assembly of nanocubes into ordered structures are governed by both dipole-dipole interactions and van der Waals interactions between the cubes. A very important detail which is considered a prerequisite for self-assembly is the increasing van der Waals interactions between nanocubes, as a result of an increase in oleic acid concentration upon solvent evaporation. This allows the cubes to first line up in the magnetic field before they eventually are forced together by the dominating van der Waals attraction at the end, favouring a face-to-face configuration. The cubes position themselves in such a way that the total energy of the dipole-dipole interactions between cubes, Zeeman interactions with the applied field, magnetocrystalline anisotropy, van der Waals interactions and steric repulsions, is kept to a minimum. At applied horizontal fields weaker than 750 G, a weaker Zeeman coupling allows for rotational Brownian motion to cause a significant deviation of magnetic moments from the field direction, mediating line formation with a [100]-morphology. If the volume is optimal, these lines will be monolayered and separated. At fields higher than 750 G, the Zeeman interactions are so strong than only a small deviation from the field is a fact, leading to the [110]-morphology rather than [100]. At field values of 500 G or higher, calculations of relaxation times suggests that the nanoparticles are effectively ferrimagnetic rather than superparamagnetic.

Low k magnons appear to be excited in the obtained one-dimensional superstructures, appearing as second peaks in the FMR spectrum. These second peaks were probably obtained only when the applied magnetic field was directed in the lengthwise direction of the lines and rods. This also suggests that an otherwise superparamagnetic system is locked in the ferrimagnetic state after self-assembly. From FMR experiments, the average magnetization of nanocubes constituting monolayers were found to be lower than the equivalent thin film. Furthermore, the shape anisotropy exhibited by the one-dimensional superstructures was to a high degree reflected in the FMR spectra, as angle dependent main peaks were observed.

Chapter 7

PROSPECTS

As far as self-assembly is concerned, this conceptually easy method may result in highly ordered patterns of nanoparticles which could be done in only a fraction of the time used to obtain equivalent structures by means of thin films and patterning methods. Moreover, fabricating periodic structures at the length scale of a few nanometers has proven difficult with conventional patterning methods [52, 53]. Due to the short timescale self-assembly represents, this will in turn imply higher throughputs in the aim of industrializing these types of magnonic structures discussed in this work. The method of self-assembly offers great flexibility in terms of the building block involved, which is not restricted to nanoparticles, but also nanorods, or nanofibers, if one-dimensional building blocks constituting the superstructures are desired. The material of choice could also be varied as desired, together with its size and morphology. A potential application for the structures considered here in this work is magnonic waveguides to convey spin waves to desired devices. Line could be used when a horizontal supply of magnons is desired, and rods could be used if a vertical supply is desired, for instance in magnonic integrated circuit design.

As for future research, improving the range of the order and uniformity in the self-assembled structures is the primary objective, together with accurately controlling the structure density. In this context, the number of nanoparticles, and hence the batch concentration, at optimal volume and field need a thorough investigation in order make the structure density tunable. Both stronger applied magnetic fields strengths and gradients, deserves an investigation as well, as novel structures could result. In addition, other solvents than hexane should be considered, which could yield different interactions between the particles in solution. The same argument applies for different surfactants, as both the interparticle interaction and the post-assembled spacing between the particles could be tuned. Moreover, this interparticle spacing is also important in terms of the magnetic dipole-dipole coupling between particles and hence the excitation of magnonic modes. In addition, the particle sizes used in this work correspond to superparamagnetic states, which would more weakly couple to the applied magnetic field, and to each other, than particles in their ferromagnetic state, or ferrimagnetic state in terms of magnetite. Increasing the size of the magnetite nanocubes to the ferrimagnetic state, or decreasing the size to a more pronounced superparamagnetic state could in turn result in different interesting obtained structures. It might be of interest to investigate other materials with a different coercivity than magnetite, and with magnetic easy axes in the $\langle 100 \rangle$-directions which could potentially result in a higher degree of ordering. In terms of Monte Carlo simulations, improvements

to avoid crude approximations, and thus make the system as real as possible, and at the same time keep the simulation computationally viable, should be a goal. Improvements in the algorithm, or using a different algorithm to make the simulation more efficient could be of interest. A specific suggestion is the **Multiple-try Metropolis** algorithm which makes the simulation more efficient in terms of moving a single particle in a confined space with a high number of degrees of freedom.[54].

At the time of writing, the main emphasis has been put on the investigation of one-dimensional structures of nanoparticles. The self-assembled system offers a more rich physics as the dimensions are extended to two-dimensional, and eventually three-dimensional, superlattices. Optimal conditions for these different superlattices need to be established, in order to successfully control the order of the system, and hence the magnonic properties.

In terms of magnetic characterization, several other characterization techniques than conventional FMR, considered here, can be employed in order to gain more insight to physics of the self-assembled magnonic system. Among them, is **flip-chip coplanar waveguide FMR** which allows magnetic field sweeps at several microwave frequencies [55]. **Magnetometry** is another technique of interest, which can be used to measure strength and direction of the magnetization of a point in space. This can be used to determine whether a self-assembled film of superparamagnetic nanoparticles, as a whole, is in the superparamagnetic or ferromagnetic state. For this particular purpose, sensitive magnetometers, such as a **superconducting quantum interference device** (SQUID) [56], is required. A similar analysis can be done with **magnetic force microscopy** (MFM), in which the orientation of the magnetic moments at the surface of the superstructures can be determined [57]. **Brillouin scattering** offers a way to experimentally determine the dispersion relation of magnonic modes, in which energy versus k-space can be determined [58].

There are, however, certain limitations associated with the self-assembled magnonic system considered in this work. First of all, magnetic field induced self-assembly is only restricted to magnetic materials, that is, antiferromagnetic materials can not be utilized. It is also difficult to control specifically at which locations the structures are deposited. This can potentially be solved by utilizing lithography methods [59], that is, pattern a photoresist where lines are wanted and then do a lift-off. Another limitation is film compression observed upon acetonitrile injection, which is likely to result in squeezed and distorted lines. Last but not least is the radial magnetic field gradient associated with any electromagnet used in magnonic structure fabrication, which would cause inhomogeneity in the applied field leading to obtained structures self-assembled at inequivalent areas of the sample.

Appendix A

PARAMETERS USED IN MONTE CARLO SIMULATIONS

The parameters used in the Monte Carlo simulations are given in Table 3.2 in Section 3.2.1. In this appendix, the calculations done to obtain certain parameters are revised as well as assumptions underlying the calculations given. Any repeated equations are reprinted from Section 2.7.2.

A.1 Brownian motion

The translational diffusion coefficient of the nanocubes was calculated according to Equation 2.19

$$D = \frac{k_B T}{f},$$

and a calculation based on Stokes formula, given by Equation 2.21

$$f = 6\pi\eta R,$$

was used to find the friction coefficient. The viscosities for hexane η_{hex} and oleic acid η_{oa}, were reported in Table 3.2 to be $0.300\,\text{mPa}\cdot\text{s}$ and $27.6\,\text{mPa}\cdot\text{s}$, respectively. However, Stokes formula assumes spherical shape, and can not be used directly. Instead the radius of the equal volume sphere of the cubes[1], calculated to be 10.03 nm, multiplied by a scaling parameter found to be 1.06 for cubes, was reported by Hubbard et al. to give a good estimate of the real cube friction coefficient [60]. Calculated translational diffusion coefficients for nanocubes in hexane D_{hex} and oleic acid D_{oa}, were $6.85 \cdot 10^{-11}\,\text{m}^2/\text{s}$ and $7.44 \cdot 10^{-13}\,\text{m}^2/\text{s}$, respectively. As far as the rotational friction coefficient is concerned, the same method applies. Since the rotational friction coefficient scales with volume of the moving body, or R^3, a factor of 1.06^3 is used with the cubed equal volume sphere radius. Calculated rotational diffusion coefficients for nanocubes in hexane $D_{\text{r,hex}}$ and oleic acid $D_{\text{r,oa}}$, were $4.55 \cdot 10^5\,\text{s}^{-1}$ and $4.94 \cdot 10^3\,\text{s}^{-1}$, respectively.

[1] That is, for the total moving cube size, equal to $a + 2L$, or 16.2 nm.

A.2 Hamaker constants

In order to calculate the Hamaker constant for the solvent, A_{hex} and A_{oa} was calculated for hexane and oleic acid, respectively. This was achieved by using the method based on the thermodynamics of liquids and by applying Equation 2.26

$$A = \frac{3}{4} k_B T \left[1 - \frac{3 + 6\alpha T}{3 + 7\alpha T} \right]^{-1}.$$

With T set to 298 K, the thermal expansion coefficients α_{hex} and α_{oa} at this temperature were found from the literature to be $1.475 \cdot 10^{-3}\ \text{K}^{-1}$ [45] and $6.49 \cdot 10^{-4}\ ^\circ\text{C}^{-1}$ [46], for hexane and oleic acid, respectively. α_{oa} was found by extrapolation, given the two values $6.86 \cdot 10^{-4}\ ^\circ\text{C}^{-1}$ at 100 °C and $7.35 \cdot 10^{-4}\ ^\circ\text{C}^{-1}$ at 200 °C, assuming a linear decrease with temperature. Hence, A_{hex} and A_{oa} were found to be $4.33 \cdot 10^{-20}$ J and $7.74 \cdot 10^{-19}$ J, respectively. Here dispersion forces are assumed to dominate the attraction, and thus the organic tail of oleic acid is assumed to be the dominating part giving rise to attraction, with a negligible polar head. The effective Hamaker constant of the solvent is found by taking the weighed volume average of the product αT in the equation above.

In terms of the Hamaker constant of magnetite, the literature seems to report ambiguous values. However, the effective Hamaker constant of magnetite in hexane seems to be close to $2.2 \cdot 10^{-20}$ J [22, 44]. Hence, Equation 2.25 for the effective Hamaker constant of magnetite in hexane

$$A_{212} = (\sqrt{A_{11}} - \sqrt{A_{22}})^2,$$

was used together with the values for the Hamaker constant of hexane and magnetite in hexane to obtain the value for only magnetite, a calculation which yielded a value of $12.6 \cdot 10^{-20}$ J.

A.3 Steric repulsion

The chain length L of oleic acid was measured using the molecular editor software Avogadro [47]. Using the energy Auto Optimization Tool, the energy minima of the molecule was found and L measured as the head-to-tail distance to be 2.08 nm.

The average volume fraction of oleic acid ϕ_{av} was calculated according to

$$\phi_{\text{av}} = N_{\text{surfactant}} \frac{V_{\text{surfactant}}}{V_{\text{shell}}},$$

where $N_{\text{surfactant}}$ is the number of ligands adsorbed onto a single nanocube, $V_{\text{surfactant}}$ is the volume of a single surfactant molecule and V_{shell} is the volume of the shell surrounding the surfactants situated on the nanocubes. The number of surfactant molecules is calculated according to $N_{\text{surfactant}} = A_{\text{core}}/A_{\text{surfactant}}$, where the surface area of the cube $A_{\text{core}} = 6a^2$ (not to be confused with the Hamaker constant A) was found to be 864 nm^2 and the average surface area per oleic acid molecule was reported in the literature to be 0.28 nm^2 [48, p.2.68], yielding the number of surfactants per nanocube to be 3085. The volume of the shell surrounding the surfactants, given by $V_{\text{shell}} = (a + L)^3 - a^3$, was calculated to be 1063.3 nm^2. $V_{\text{surfactant}}$ is calculated according to $V_{\text{surfactant}} = M_{\text{surfactant}}/\rho_{\text{surfactant}}$ in which $M_{\text{surfactant}}$ equal to $4.690 \cdot 10^{-25}$ kg (calculated by counting atomic mass units) is the mass of one single surfactant molecule, and $\rho_{\text{surfactant}}$ is the density of oleic acid, reported to be 895 kg/m^3 at 298 K [49]. This yields a $V_{\text{surfactant}}$ equal to 0.5240 nm^3. Now, as $N_{\text{surfactant}}$, $V_{\text{surfactant}}$ and V_{shell} are all known, ϕ_{av} is estimated to be 1.52, that is, a volume fraction larger than unity. It is an indication that the surfactant chains are closer packed on the nanocube than in the liquid state, and since a volume fraction can not be larger than unity, ϕ_{av} is set to 1.

The volume of the solvent molecules, $V_{\text{s,hex}}$ and $V_{\text{s,oa}}$, is calculated from the molecular weight and the densities of the respective solvent molecules. $V_{\text{s,oa}}$ which is basically the same as $V_{\text{surfactant}}$, was found above to be $5.240 \cdot 10^{-28}$ m^3. Hexane can be calculated the same way, by using the molecular weight found to be $1.330 \cdot 10^{-25}$ kg, and the density reported to be 659 kg/m^3 at 298 K [42], yielding a $V_{\text{s,hex}}$ equal to $2.018 \cdot 10^{-28}$ m^3.

The Flory parmeter is calculated according to Equation 2.28

$$\chi = \frac{V_{\text{s}}}{k_B T}(\delta_{\text{solvent}} - \delta_{\text{surfactant}})^2 + \beta,$$

with the Hildebrand solubility parameters δ_{hex} for hexane and δ_{oa} for oleic acid equal to $1.49 \cdot 10^4$ $\text{Pa}^{\frac{1}{2}}$ and $1.56 \cdot 10^4$ $\text{Pa}^{\frac{1}{2}}$ [50], respectively. In hexane, using $V_{\text{s,hex}}$, the Flory parameter is calculated to be 0.366. In oleic acid, however, the solvent and surfactant has the same Hildebrand parameter resulting in a reduction of the Flory parameter to β, or 0.34.

The number of surfactants per unit area nanocube surface was calculated through the relation $\nu = 1/A_{\text{surfactant}}$, with $A_{\text{surfactant}}$ given above as 0.28 nm^2. Converting $A_{\text{surfactant}}$ to m^2 yields a ν equal to $3.57 \cdot 10^{18}$ m^{-2}.

A.4 Magnetism

The intrinsic magnetic moment, m_s, of the nanocubes was calculated from the product of the nanocube saturation magnetization M_s and volume V. M_s was reported to be $4.80 \cdot 10^5$ A/m for bulk magnetite in Section 2.6, and V calculated to be $1.73 \cdot 10^{-24}$ m^3. M_s was multiplied by a correction factor of 0.9 to account for a disordered surface layer. As stated in Section 2.2.3, the thickness of the disordered surface layer is typically ~ 1 nm, thus for a cube of size 12 nm the percentage volume of disordered material is close to 80 %. However, there would not be an instant transition from an ordered to disordered lattice and this outer part of the cube would still contribute to the total magnetic moment. Moreover, as can be seen from the TEM image of a nanocube in Figure 2.12b in Section 2.6, the surface can be rather rough. Thus, a saturation magnetization correction factor of 0.9 is assumed. The product of the corrected saturation magnetization and nanocube volume yielded an intrinsic magnetic moment equal to $7.47 \cdot 10^{-19}$ Am^2.

As stated and justified in Section 2.6, the sixth order term K_{A2} in Equation 2.17 for describing magnetocrystalline anisotropy is neglected. Thus, only the quartic term K_{A1} is used and renamed K_A.

REFERENCES

[1] J. Stöhr and H. C. Siegmann. *Magnetism; From Fundamentals to Nanoscale Dynamics*. Springer-Verlag Berlin Heidelberg, 2006.

[2] S. Blundell. *Magnetism in Condensed matter*. Oxford University Press Inc., 2001.

[3] F. Bloch. "Zur Theorie des Ferromagnetismus". In: *Zeitschrift für Physik* 61.3-4 (1930), pp. 206–219. ISSN: 0044-3328. DOI: 10.1007/BF01339661. URL: 10.1007/BF01339661.

[4] S. O. Demokritov and A. N. Slavin, eds. *Magnonics; From Fundamentals to Applications*. Springer-Verlag Berlin Heidelberg, 2013.

[5] C. Kittel. *Introduction to Solid State Physics*. Eight. John Wiley & Sons, Inc, 2005.

[6] C. Kittel. "On the Theory of Ferromagnetic Resonance Absorption". In: *Phys. Rev.* 73 (2 1948), pp. 155–161. DOI: 10.1103/PhysRev.73.155.

[7] J. H. E. Griffiths. "Anomalous High-frequency Resistance of Ferromagnetic Metals". In: *Nature* 158 (1946), pp. 670–671. DOI: 10.1038/158670a0.

[8] B. Lenk et al. "The building blocks of magnonics". In: *Physics Reports* 507.4–5 (2011), pp. 107 –136. ISSN: 0370-1573. DOI: 10.1016/j.physrep.2011.06.003.

[9] A. Dong et al. "Binary nanocrystal superlattice membranes self-assembled at the liquid–air interface". In: *Nature* 466 (2010), 474–477. DOI: 10.1038/nature09188.

[10] G. Singh et al. "Self-assembly of magnetite nanocubes into helical superstructures". In: *Science* 345.620 (2014), pp. 1149–1153. DOI: 10.1126/science.1254132.

[11] K. J. Bishop et al. "Nanoscale forces and their uses in self-assembly". In: *small* 5 (2009), 1600–1630. DOI: 10.1002/smll.200900358.

[12] D. D. Stancil and A. Prabhakar. *Spin waves; Theory and Applications*. Springer Science+Business Media, LLC, 2009.

[13] http://www2.physics.colostate.edu/groups/PattonGroup/systems/epr_desc.html. Electron paramagnetic resonance. Retrieved: May 16. 2015.

[14] J. Jiang and R. T. Weber. *ELEXSYS E 500 User's Manual: Basic Operations*. http://www.sb.fsu.edu/~fajer/Fajerlab/LinkedDocuments/E500%20Basic.pdf. EPR Division, Bruker BioSpin Corporation. Billerica, MA USA, 2001.

[15] http://en.wikipedia.org/wiki/Electron_paramagnetic_resonance. Electron paramagnetic resonance. Retrieved: May 16. 2015.

[16] V. V. Kruglyak, S. O. Demokritov, and D. Grundler. "Magnonics". In: *Journal of Physics D: Applied Physics* 43.26 (2010), p. 264001. URL: http://stacks.iop.org/0022-3727/43/i=26/a=264001.

[17] M. Kostylev et al. "Partial frequency band gap in one-dimensional magnonic crystals". In: *Applied Physics Letters* 92.13, 132504 (2008). DOI: 10.1063/1.2904697.

[18] G. Gubbiotti et al. "Collective spin modes in monodimensional magnonic crystals consisting of dipolarly coupled nanowires". In: *Applied Physics Letters* 90.9, 092503 (2007). DOI: 10.1063/1.2709909.

[19] M. P. Kostylev, A. A. Stashkevich, and N. A. Sergeeva. "Collective magnetostatic modes on a one-dimensional array of ferromagnetic stripes". In: *Phys. Rev. B* 69 (6 2004), p. 064408. DOI: 10.1103/PhysRevB.69.064408.

[20] J. O.Vasseur et al. "Magnon band structure of periodic composites". In: *Phys. Rev. B* 54 (2 1996), pp. 1043–1049. DOI: 10.1103/PhysRevB.54.1043.

[21] D. Levy, R. Giustetto, and A. Hoser. "Structure of magnetite (Fe_3O_4) above the Curie temperature: a cation ordering study". In: *Phys Chem Minerals* 39 (2011), 169–176. DOI: 10.1007/s00269-011-0472-x.

[22] G. Singh et al. "Supplementary Materials for Self-assembly of magnetite nanocubes into helical superstructures". In: *Science* 345.620 (2014), pp. 1149–1153. DOI: 10.1126/science.1254132.

[23] B. P. Weiss et al. "Ferromagnetic resonance and low-temperature magnetic tests for biogenic magnetite". In: *Earth and Planetary Science Letters* 224.1–2 (2004), pp. 73 –89. ISSN: 0012-821X. DOI: 10.1016/j.epsl.2004.04.024.

[24] Ö. Özden. "Coercive force of single crystals of magnetite at low temperatures". In: *Geophysical Journal International* 141.2 (2000), pp. 351–356. DOI: 10.1046/j.1365-246x.2000.00081.x.

[25] D. J. Craik, ed. *Magnetic Oxides*. John Wiley & Sons, Ltd, 1975.

[26] T. K. McNab, R. A. Fox, and A. J. F. Boyle. "Some Magnetic Properties of Magnetite (Fe3O4) Microcrystals". In: *Journal of Applied Physics* 39.12 (1968), pp. 5703–5711. DOI: 10.1063/1.1656035.

[27] G. M. Whitesides and B. Grzybowski. "Self-Assembly at All Scales". In: *Science* 295.5564 (2002), pp. 2418–2421. DOI: 10.1126/science.1070821.

[28] G. M. Whitesides and M. Boncheva. "Beyond molecules: Self-assembly of mesoscopic and macroscopic components". In: *PNAS* 99.8 (2002), 4769–4774. DOI: 10.1073/pnas.082065899.

[29] P. C. Nelson. *Biological Physics: Energy, Information, Life*. Updated First. W. H. Freeman and Company, 2008.

[30] F. Fujara et al. “Translational and rotational diffusion in supercooled orthoterphenyl close to the glass transition”. In: *Zeitschrift für Physik B Condensed Matter* 88.2 (1992), pp. 195–204. DOI: 10.1007/BF01323572.

[31] P. C. Heimenz and R. Rajagopalanl. *Principles of Colloid and Surface Chemistry*. Third. Taylor & Francis Group, LLC, 1997.

[32] M. D. Croucher. “A simple expression for the Hamaker constant of liquid-like materials”. In: *Colloid and Polymer Science* 259.4 (1981), pp. 462–466. DOI: 10.1007/BF01524883.

[33] N. Goubet et al. “Which Forces Control Supracrystal Nucleation in Organic Media?” In: *Advanced Functional Materials* 21.14 (2011), pp. 2693–2704. DOI: 10.1002/adfm.201100382.

[34] C. M. Hansen. *Hansen Solubility Parameters: A User’s Handook*. First. Taylor & Francis Group, LLC, 2007.

[35] http://www.qsimaging.com/ccd_noise_interpret_ffts.html. Interpret Fourier Transforms (FFT). Retrieved: June 15. 2015.

[36] E. Kreyszig. *Advanced Engineering Mathematics*. Ninth. John Wiley & Sons Inc., 2006.

[37] http://ntnu.norfab.no/WebForms/Equipment/EquipmentView.aspx?toolId=11. S(T)EM (1512). Retrieved: May 18. 2015.

[38] J. M. Hammersley and D. C. Handscomb. *Monte Carlo Methods*. First. Methuen & Co Ltd., 1964.

[39] D. Frenkel and Berend Smit. *Understanding Monte Carlo Simulation: From Algorithm to Application*. First. Academic Press, 2002.

[40] http://www.mathworks.com/products/matlab/?refresh=true. MathWorks. Retrieved: May 24. 2015.

[41] K. A. Dill and S. Bromberg. *Molecular Driving Forces: Statistical Thermodynamics in Biology, Chemistry, Physics and Nanoscience*. Second. Taylor & Francis Group, LLC, 2011.

[42] http://www.sigmaaldrich.com/chemistry/solvents/hexane-center.html. Hexane. Sigma-Aldrich. Retrieved: May 21. 2015.

[43] http://www.sjlipids.com/c181.htm. Oleic acid. S & J Lipids. Retrieved: May 22. 2015.

[44] B. Faure, G. Salazar-Alvarez, and L. Bergström. “Hamaker Constants of Iron Oxide Nanoparticles”. In: *Langmuir* 27.14 (2011), pp. 8659–8664. DOI: 10.1021/la201387d.

[45] Z. I. Zaripov et al. “Thermal Properties of n-Hexane at Temperatures of 298.15–363.5 K and Pressures of 0.098–147 MPa”. In: *Theoretical Foundations of Chemical Engineering* 36.4 (2002), pp. 400–405. ISSN: 0040-5795. DOI: 10.1023/A:1019864119650.

[46] http://www.google.com/patents/EP1114425A4?cl=en. High oleic acid oil compositions and electrical devices containing the same . Retrieved: May 20. 2015.

[47] http://avogadro.cc/wiki/Main_Page. Avogadro . Retrieved: May 21. 2015.

[48] J. Lyklema. *Fundamentals of Interface and Colloid Science: Particulate Colloids, Volum IV*. First. Elsevier Ltd., 2005.

[49] http://pubchem.ncbi.nlm.nih.gov/compound/oleic_acid. Oleic acid. PubChem. Retrieved: May 21. 2015.

[50] http://cool.conservation-us.org/coolaic/sg/bpg/annual/v03/bp03-04.html. Solubility Parameters: Theory and Application. Sigma-Aldrich. Retrieved: May 21. 2015.

[51] R. F. Butler. "Theoretical Single-Domain Grain Size Range in Magnetite and Titanomagnetite". In: *Journal of Geophysical Research* 80.29 (1975), pp. 4049 –4058. DOI: 10.1029/JB080i029p04049.

[52] J. Orloff, L. W. Swanson, and M. Utlaut. "Fundamental limits to imaging resolution for focused ion beams". In: *Journal of Vacuum Science & Technology B* 14.6 (1996), pp. 3759–3763. DOI: 10.1116/1.588663.

[53] V. R. Manfrinato et al. "Resolution Limits of Electron-Beam Lithography toward the Atomic Scale". In: *Nano Letters* 13.4 (2013), pp. 1555–1558. DOI: 10.1021/nl304715p.

[54] J. S. Liu, F. Liang, and W. H. Wong. "The Multiple-Try Method and Local Optimization in Metropolis Sampling". In: *Journal of the American Statistical Association* 95.449 (2000), pp. 121–134. DOI: 10.1080/01621459.2000.10473908.

[55] I. Neudecker et al. "Comparison of frequency, field, and time domain ferromagnetic resonance methods". In: *Journal of Magnetism and Magnetic Materials* 307.1 (2006), pp. 148 –156. ISSN: 0304-8853. DOI: 10.1016/j.jmmm.2006.03.060.

[56] K. Enpuku et al. "Detection of Magnetic Nanoparticles with Superconducting Quantum Interference Device (SQUID) Magnetometer and Application to Immunoassays". In: *Japanese Journal of Applied Physics* 38.10A (1999), p. L1102. DOI: 10.1143/JJAP.38.L1102.

[57] U. Hartmann. "Magnetic Force Microscopy". In: *Annual Review of Materials Science* 29.1 (1999), pp. 53–87. DOI: 10.1146/annurev.matsci.29.1.53.

[58] Y. Takagi and K. Kurihara. "Application of a microscope to Brillouin scattering spectroscopy". In: *Review of Scientific Instruments* 63.12 (1992), pp. 5552–5555. DOI: 10.1063/1.1143380.

[59] Michael Quirk and Julian Serda, eds. *Semiconductor Manufacturing Technology*. Prentice Hall, Inc, 2001.

[60] J. B. Hubbard and J. F. Douglas. “Hydrodynamic friction of arbitrarily shaped Brownian particles”. In: *Physical Review E* 47.5 (1993), pp. 2983–2986. URL: http://www.stevens-tech.edu/zeno/journals/pR2983_1.pdf.